Integrated Stability and Tracking Control System for Autonomous Vehicle-Trailer Systems

by

Mehdi Abroshan

A thesis
presented to the University of Waterloo
in fulfillment of the
thesis requirement for the degree of
Doctor of Philosophy
in
Mechanical and Mechatronics Engineering

Waterloo, Ontario, Canada, 2021

Examining Committee Membership

The following served on the Examining Committee for this thesis. The decision of the Examining Committee is by majority vote.

External Examiner:	Yang Shi Professor, Mechanical Engineering University of Victoria
Supervisor(s):	Amir Khajepour Professor, Mechanical and Mechatronics Engineering
Internal Member:	Dongpu Cao Associate Professor, Mechanical and Mechatronics Engineering
Internal Member:	Ehsan Hashemi Adjunct Assistant Professor, Mechanical and Mechatronics Engineering
Internal-External Member:	Glenn Heppler Professor, Systems Design Engineering

Author's Declaration

I hereby declare that I am the sole author of this thesis. This is a true copy of the thesis, including any required final revisions, as accepted by my examiners.

I understand that my thesis may be made electronically available to the public.

Abstract

The addition of a trailer to a vehicle significantly changes the dynamics of a single-vehicle and generates new instability modes including jackknifing and snaking. Understanding of the dynamics of these modes leads to the development of more effective control strategies for improved stability and handling. In addition, vehicle-trailer systems suffer from the off-tracking problem meaning that the path of the trailer rear end differs from that of the vehicle front end. Off-tracking makes these vehicles less maneuverable and increases swept path of the vehicle, especially in urban areas and tight spaces.

Vehicle active safety systems have been extensively developed over the past decades to improve vehicle handling and assist the driver to keep the vehicle under control in unfavorable driving situations. Such active safety systems, however, are not well developed for vehicle-trailer systems specialty to control the above-mentioned instability modes. In addition to the above active safety systems, off-tracking of vehicle-trailers is another aspect that is essential in path planning and path tracking of autonomous vehicle-trailers.

In this thesis, first, phase portraits are used to study the non-linear dynamics of the system through state trajectories and equilibrium point locations of a vehicle-trailer system, with respect to the inputs and also the loading conditions of the trailer. By the study of the phase portraits, the foundation of the vehicle-trailer yaw instability is recognized and a two-dimensional stable region as the stability envelope is defined. This stability envelope is utilized to prevent unnecessary control interventions while the vehicle is operating in the safe stability region whereas the controller is allowed to effectively interfere when the vehicle crosses the stability envelope.

To handle multiple control actions in the vehicle and trailer units, a control structure with two hierarchical layers is proposed. In the upper layer, a model predictive controller is formulated as a quadratic optimization problem with a virtual control action for each degree of freedom of the vehicle dynamic model. In this formulation, the developed stability envelope is constructed as state constraints along with control action constraints. In the lower layer, a control allocation approach optimally transforms the virtual control actions provided by the upper layer into steering and/or braking commands for each wheel. In this approach, actuator failure in addition to actuator and tire capacity constraints is taken into account in real-time.

A hybrid A*-based motion planning is developed to generate a trajectory while considering the trailer effect in terms of stability in high speed and off-tracking in high curvature paths. The proposed motion planning utilizes a hybrid A* algorithm combined with potential fields to find a feasible and collision-free trajectory for the vehicle-trailer system.

To assess the performance of the proposed control structure in instability prevention both in snaking and jackknifing, different simulations are conducted using different control actions. Additionally, the fault tolerance and robustness of the proposed controller are investigated. To validate the real-time performance of the proposed control strategy, experimental tests are performed on a vehicle-trailer system with differential braking capability. The results show that the proposed control strategy is able to effectively prevent both instability modes as well as unnecessary engagement of the control action to reduce control intervention. The performance of the developed motion planning module is also evaluated for normal driving, obstacle avoidance, off-tracking compensation, and crash mitigation using high-fidility Carsim model. It is observed that proposed motion planning is able to effectively satisfy all the expected requirements.

Acknowledgements

Although I am the only one whose name is on the cover of this thesis, many people helped me to accomplish this research, and here is the only place I can express my feelings and sincere gratitude to them. First and foremost, I am extremely grateful to my supervisors, Prof. Amir Khajepour, for his invaluable advice, continuous support and encouragement, and patience throughout my PhD study. Besides my supervisor, I would like to thank Dr. Ehsan Hashemi for his knowledge and guidance in all the steps of this research.

This journey would not be going smoothly without my friends. My sincere and heartfelt gratitude goes to Dr. Avesta Goodarzi, who provided me with the guidance and support I need to start my PhD program and also Dr. Amir Soltani, who kindly and generously helped me to settle down in Canada in 2017. I cannot thank enough Dr. Alireza Pazooki and Dr. Laaleh Durali for their genuine friendship and all the fun we have had over the last four years. In addition, I would like to thank my friends and colleagues, Saed Farajnejad, Gary Zhang, Chen Tang, Reza Hajiloo, Amin Habibnejad, Halit Zengin and all others for their support and assistance.

The experiments could not have been possible without the MSV lab technicians, Jeff Graansma, Aaron Sherratt, Jeremy Reddekopp, and Adrian Neill.

Most importantly, I would like to express my heartfelt gratitude to my wonderful and loving family members for their unending support throughout my life and this endeavor.

Dedication

To my sister Roya for being endless source of love, inspiration, and support.

Table of Contents

List of Figures xi

List of Tables xv

1 Introduction 1

1.1 Motivation . . . 1

1.2 Objectives . . . 3

1.3 Outline . . . 4

2 Literature Review and Background 6

2.1 Vehicle-Trailer Stability Analysis . . . 6

2.2 Active Safety Systems . . . 9

2.3 Motion Planning . . . 10

2.4 Envelope Control . . . 15

2.5 Control Allocation . . . 18

2.6 Summary . . . 20

3 Stability Envelope Development for Vehicle-Trailer Systems 22

3.1 Tire Model . . . 22

3.2 Non-Linear Vehicle-Trailer System Model . . . 25

3.2.1 Affine Bicycle Model . . . 27

3.3 Stability Analysis . . . 29
3.3.1 A Trailer as a Pendulum . . . 32
3.3.2 Phase Plane Analysis of Vehicle-Trailer System . . . 34
3.4 Summary . . . 45

4 Development of a Reconfigurable Vehicle-Trailer Control System 48
4.1 Upper Layer, Model Predictive Control . . . 48
4.1.1 Desired Response . . . 51
4.1.2 Constraints . . . 51
4.1.3 Performance Index . . . 53
4.2 Lower Layer, Optimized Distribution . . . 55
4.3 Simulation and Experimental Results . . . 58
4.3.1 Simulation Results . . . 59
4.3.2 Experimental Results . . . 74
4.4 Summary . . . 79

5 Hybrid A*-Based Motion Planning for Vehicle-Trailer Systems 81
5.1 Trajectory Tracking Affine Bicycle Model . . . 82
5.2 Autonomous Vehicle Architecture . . . 84
5.3 Hybrid A* Algorithm . . . 86
5.3.1 Fundamentals . . . 86
5.3.2 Hybrid A* search: . . . 88
5.4 Potential Field . . . 89
5.4.1 Non-Crossable Obstacle . . . 89
5.4.2 Road Curb . . . 92
5.5 The Proposed Motion Planning . . . 93
5.6 Simulation Results . . . 101
5.6.1 Merging, a normal driving scenario . . . 102

5.6.2 Sharp turn, off-tracking problem . . . 105
5.6.3 Lane change, a pop-up obstacle . . . 105
5.6.4 Crash mitigation, obstacle prioritization . . . 108
5.7 Summary . . . 116

6 Conclusions and Future Work **117**
6.1 Conclusions . . . 117
6.2 Future Work . . . 119

References **121**

APPENDICES **136**

A Appendix A **137**
A.1 Affine Bicycle Model . . . 137
A.2 Performance Index . . . 138
A.3 Trajectory Tracking Affine Bicycle Model . . . 139

List of Figures

2.1 General structure for autonomous vehicles 11
2.2 The effect of heuristic technique in search improvement 14
2.3 Phase portraits of an under-steer single-vehicle 16
2.4 Phase portraits of an over-steer single-vehicle 17

3.1 Combined tire force limits 23
3.2 Tire models 24
3.3 Free body diagram of a planar bicycle model for stability analysis of a vehicle-trailer vehicle 25
3.4 Linearizing tire model around lateral slip angle operating point 28
3.5 Different instability modes, (a) saddle-node bifurcation (b) continuous divergence (c) Hopf bifurcation (d) oscillatory motion 30
3.6 Trailer pendulum model. 33
3.7 Phase portraits for unloaded trailer, $\delta = 0$ deg 36
3.8 Phase portraits for unloaded trailer, $\delta = 7$ deg 37
3.9 Phase portraits for unloaded trailer, $\delta = 9$ deg 37
3.10 Phase portraits when vehicle-trailer is vulnerable to jackknifing, $\delta = 5$ deg 38
3.11 Phase portraits when vehicle-trailer is vulnerable to jackknifing, $\delta = 7$ deg 39
3.12 Phase portraits when vehicle-trailer is vulnerable to snaking, $\delta = 5$ deg . . 39
3.13 Phase portraits when vehicle-trailer is vulnerable to snaking, $\delta = 7$ deg . . 40
3.14 Phase portraits when vehicle-trailer is vulnerable to snaking, $\delta = 7$ deg-magnified 40

3.15 Phase portraits when vehicle-trailer is vulnerable to snaking, $\delta = 7.5$ deg . 41
3.16 Trajectory comparison. 41
3.17 2D stability envelope. 45
3.18 Equilibrium point at the stability margin 46

4.1 The structure of the proposed controller 49
4.2 Illustration of model predictive control (MPC) concept 50
4.3 Approximated friction circle limit by an octagon 57
4.4 Performance of the controller with the steering-based control actions in the double lane change maneuver 62
4.5 Performance of the controller with the steering-based control actions in the double lane change maneuver 63
4.6 Performance of the controller with the braking-based control actions in the double lane change maneuver 64
4.7 Performance of the controller with the braking-based control actions in the double lane change maneuver 65
4.8 Performance of the controller with the steering-based control actions in the cornering maneuver 66
4.9 Performance of the controller with the steering-based control actions in the cornering maneuver 67
4.10 Performance of the controller with the braking-based control actions in the cornering maneuver 68
4.11 Performance of the controller with the braking-based control actions in the cornering maneuver 69
4.12 Performance of the controller with integrated VDB and ARS control actions in the double lane change maneuver 70
4.13 Performance of the controller with integrated VDB and TDB control actions in the double lane change maneuver 71
4.14 Performance of the controller with VDB control action in the double lane change maneuver when actuator failure occurs 72
4.15 Performance of the controller with VDB control action in the double lane change maneuver where the estimated properties of the trailer are not accurate 73

4.16 The electric all-wheel-drive Chevrolet Equinox vehicle and the trailer attached 74
4.17 Experimental setup network 75
4.18 Experimental test results of the vehicle without controller in the accelerating slalom maneuver 77
4.19 Experimental test results of the vehicle with controller in the accelerating slalom maneuver. 78
4.20 Experimental test results of the vehicle with controller in the double lane change maneuver 80

5.1 Schematic of the trajectory tracking model and the lateral and heading errors 83
5.2 Autonomous vehicle architecture 85
5.3 State space subdivision 87
5.4 Graph representation 87
5.5 Defined areas around non-crossable obstacle 91
5.6 Ego vehicle with trailer 91
5.7 Potential field of a non-crossable obstacle 93
5.8 Potential field of road curbs 94
5.9 Obstacles in (s,y) coordinates 95
5.10 Expansion and pruning 97
5.11 Stability and comfortable envelopes 98
5.12 Possible goal/target locations and local terminals 100
5.13 Goal and local terminal in normal driving scenario 102
5.14 Path of the ego vehicle in the normal driving scenario 103
5.15 Simulation results in the normal driving scenario 104
5.16 Path of ego vehicle in sharp turn with and without considering trailer effect 106
5.17 Simulation results in the normal driving scenario 106
5.18 Path of ego vehicle in lane change scenario 107
5.19 Simulation results in the lane change scenario 109
5.20 Path of ego vehicle in first crash mitigation scenario 110

5.21 Simulation results in the obstacle prioritization scenario-passing 111
5.22 Hybrid A* algorithm search process at first time step in first crash mitigation scenario 112
5.23 Path of ego vehicle in second crash mitigation scenario 113
5.24 Simulation results in the obstacle prioritization scenario-lane change 114
5.25 Hybrid A* algorithm search process at first time step second crash mitigation scenario 115
5.26 Path of ego vehicle in third crash mitigation scenario 115
5.27 Simulation results in the obstacle prioritization scenario-Straight 116

List of Tables

3.1 Parameter description for the vehicle-trailer bicycle model. 27
3.2 Characterization of the instability modes 32
3.3 Corresponding values for nonlinear-vehicle parameters. 34
3.4 Maximum absolute values and grid sizes of initial condition vector component. 35

4.1 Corresponding values for the vehicle parameters used in simulations 59
4.2 Hyper-parameters of the MPC controller for stability control-Simulation . . 60
4.3 Corresponding values for baseline-vehicle parameters. 75
4.4 Hyper-parameters of the MPC controller for stability control-Experimental 76

5.1 Priority of the Obstacles and the corresponding cost 108

Chapter 1

Introduction

For providing more freight capacity and reducing fuel consumption, people have been encouraged to use a second unit attached to the main vehicle especially in North America [1]. Generally, this system, known as a tractor-trailer, consists of a towing unit and a towed unit which are connected by an articulation joint. A vehicle-trailer as a specific form of tractor-trailer systems is the main focus of this thesis. In this case, the towing unit can be a passenger car or a pickup truck and the towed unit can be a boat, caravan, or any type of trailer.

1.1 Motivation

Every year, thousands of people are killed and injured in vehicle collisions throughout the world. Based on Transport Canada's National Collision Database (NCDB), 1858 motor vehicle fatalities were reported in 2015 [2]. These accidents have different causes such as road conditions, high speeds, human distractions, etc.

To reduce the risk of loss of control and improve safety and handling, conventional road vehicles are equipped with active control systems to assist the driver. These systems interfere with the vehicle inputs until the undesired vehicle dynamic behavior is corrected. These active safety features include ABS (Anti-lock Braking System), TCS (Traction Control System), ESC (Electronic stability control) and ASC (Active Steering Control), etc. Many studies have shown that these active systems significantly improve the vehicle dynamics, especially at high lateral accelerations [3].

Yet, most of these active safety systems have been developed for single-unit vehicles and do not consider the effects of any attached unit such as a trailer. In comparison with a single-unit vehicle, the dynamic behavior of a vehicle-trailer system is more complex. More precisely, the stability of these type of vehicles is strongly affected by the dynamics of the attached trailer which consequently adds additional instability modes to the combined dynamic system. Therefore a unified control strategy is required to employ the available active systems to fulfill vehicle-trailer stability requirements which are essential for instability prevention of these type of vehicles.

Despite the importance of the number and type of actuators, using each active safety system without considering the effect of other actuation systems can have a detrimental effect on the total controlling performance. These systems may fight each other in emergency situations causing the vehicle controller not to perform effectively. This can also be more dangerous in vehicle-trailer systems because the combined vehicle may experience contradicting control actions at each unit.

Despite the challenges that multiple control actions might cause, the over-actuated systems provide an opportunity to improve the vehicle control system in all driving conditions as each actuation system is usually more effective in certain road and driving conditions. This can be done by integrating all active safety systems and forming a reconfigurable control structure. The main challenge of the integration is to first recognize and identify the foundation of the instabilities in vehicle-trailer systems. A genuine understanding significantly boosts the likelihood of designing an appropriate algorithm for efficiently exploiting control systems in a cooperative way with minimum control intervention that guarantees the comfort of the passengers.

It is proven that the aforementioned active safety systems can significantly improve the stability of conventional vehicles. Nonetheless, with the advent of new technologies, autonomous driving has been proposed as a safer way of driving in the future that can exploit these safety systems more efficiently [4, 5]. Some of these new technologies are the Global Positioning System (GPS), by-wire technologies, and other technologies providing environmental information.

In autonomous vehicles, motion planning is one of the modules that is strongly connected to the control module that affects vehicle stability. This module is utilized to generate a safe, comfortable, and feasible trajectory considering road regulations, obstacles, and stability limits for the motion of the vehicle. This generated trajectory is ultimately fed to the control module for tracking. In this regard, a motion planning module is obliged to consider the limitations of vehicle-trailer systems to provide the aforementioned requirements of a suitable trajectory. In addition to different dynamic behavior and instability modes,

due to the longer length of vehicle-trailer systems, these vehicles are less maneuverable in tight spaces. Off-tracking is the main source of this lack of maneuverability and means that the rear end of the trailer is not following the path of the vehicle unit. Therefore, ignoring trailer off-tracking can result in traffic problems and collisions. In conclusion, an autonomous vehicle-trailer requires a motion planning module that not only takes the stability limits of the vehicle into account during the planning process but also systematically considers the off-tracking problem.

1.2 Objectives

For an efficient control strategy with the least control interference, the lateral dynamic behavior of vehicle-trailer systems needs to be investigated and the essence of the instability modes is required to be identified. Therefore, the first objective of this thesis is to analyze the non-linear behavior of vehicle-trailer systems to recognize the main sources of the yaw instabilities and find a region in which the vehicle remains stable without any control intervention. Hereof, an appropriate control strategy can be developed that only enables the active safety systems when the vehicle is about to leave the stable region. To do so, the phase plane analysis is conducted to understand the non-linear behavior of a vehicle-trailer system by plotting its phase portraits in a three-dimensional space for different steering angles and loading conditions. These phase portraits are studied to discover the behavior of the equilibrium point and its moving direction to find the margin of instability and the stable region.

The second objective is to develop a reconfigurable controller for a vehicle-trailer system that is equipped with different control actions on both vehicle and trailer units. This reconfigurable controller is expected to ensure the stability of the vehicle-trailer systems in a wide range of longitudinal velocities and loading conditions. Additionally, the controller needs to have the minimum intervention while the vehicle is inside a safe and stable region. This control structure needs to handle different steering and/or braking-based control actions in a systematic manner without any considerable modifications. As a solution, a two-layer control structure is presented that can fulfill the above-mentioned requirements. In the upper layer, a model predictive controller is developed that has the capability to prevent excessive control actions when the vehicle is inside the stable region. In the lower layer, the control allocation technique is utilized to optimally employ the available actuators. This scheme is able to flexibly exploit the actuators and handle actuator failures.

The third objective is to formulate a motion planning module that can consider vehicle-trailer limitations. The proposed motion planning needs to ensure that the autonomous

vehicle-trailer does not violate stability limits while it is tracking the provided trajectories. In addition, it needs to have a structured approach for considering the trailer effect in sharp maneuvers, when the off-tracking problem might cause a collision. To address these requirements, in the proposed motion planning approach, the hybrid A* algorithm is combined with the potential field approach to provide a safe and feasible trajectory. This approach can not only consider all the vehicle-trailer requirements but also has the capability to prioritize the obstacles for crash mitigation.

Moreover, the proposed controller strategy and the developed motion planning approach should be computationally efficient for real-time implementation.

1.3 Outline

In the second chapter of this thesis, first, the background of the vehicle-trailer stability analysis is studied based on different techniques while key considerations are discussed. Secondly, different active safety systems are reviewed with emphasis on those which have been used for articulated vehicles. Then, the literature on motion planning and control as essential parts of autonomous vehicles are reviewed. Afterward, the envelope control concept and its background on vehicle control are explored. Lastly, the control allocation technique and its capabilities are discussed. In the third chapter, a non-linear vehicle-trailer lateral dynamic model is derived, and based on that an affine bicycle model with the state-space representation is generated. The lateral stability of vehicle-trailer systems is analyzed and two different yaw instability modes are characterized. Finally, the phase plane method is exploited to identify the non-linear behavior of a vehicle-trailer system. Using different three-dimensional phase portraits, state trajectories are visualized and different instability modes of vehicle-trailers are analyzed. By drawing a conclusion from the presented phase portraits, a two-dimensional stability envelope is developed which theoretically guarantees the vehicle-trailer's yaw stability regardless of its loading condition.

In the fourth chapter, a reconfigurable control structure is developed with two layers that generates the optimized control actions and optimally distributes among available actuators. In the upper layer, a model predictive controller is developed that constraints the yaw rate and the sideslip angle based on the developed stability envelope and provides three virtual control actions for each degree of freedom. In the lower layer, the control allocation technique is formulated to map the virtual control actions of the upper layer into actuator actions considering actuator/tire constraints and also the friction circle in cases that both steering and braking are applied to the tire. The performance of the proposed control structure is assessed in both yaw instability modes, snaking and jackknifing using

different steering and braking-based control actions and their combinations. Furthermore, the fault tolerance and the robustness of the controller are investigated. In addition to the simulations, the proposed stability envelope and the MPC controller are experimentally examined in different maneuvers and the results are presented.

In the fifth chapter, first, an MPC trajectory tracking model is derived by augmenting the previously developed affine model with the new state variables required for this task. The hybrid A* algorithm is combined with the potential field approach to formulate the motion planner. In the proposed approach local terminals are defined to prevent infeasibility and provide an opportunity for prioritizing the obstacles in order to find the path with the lowest crash cost. The performance of the motion planning module is examined through simulations in several scenarios.

Chapter six presents the conclusions of the work and provides suggestions for the continuation of this project.

Chapter 2

Literature Review and Background

This chapter mainly presents a review of the literature on tractor-trailer stability analysis, active safety systems of tractor-trailer systems, and motion planning for autonomous vehicles. As mentioned, a vehicle-trailer that is a specific form of tractor-trailer vehicles is the main focus of this thesis. In these type of vehicles, the towing unit can be a passenger car or a pickup truck and the towed unit can be a boat, caravan or any type of trailer. Although a commercial tractor-trailer vehicle can be represented by a similar mathematical model, there are mainly two differences between a commercial tractor-trailer and a vehicle-trailer combination. Firstly, the mass ratio of the trailer to the towing vehicle that is normally below one for a vehicle-trailer combination and bigger than 10 for a large commercial vehicle. Secondly, they have a different coupling at the hitch point. Nonetheless, those studies on commercial vehicles whose control strategies can be used in vehicle-trailer systems are also reviewed in this chapter.

2.1 Vehicle-Trailer Stability Analysis

In comparison with a single-unit vehicle, the dynamic behavior of a vehicle-trailer system is more complex. This complexity comes from two main reasons. First, due to the fact that the stability of this type of vehicle is strongly affected by the dynamics of the attached trailer, other instability modes are consequently added to the combined dynamic system. Secondly, the motion of trailers is not predicted by a driver because of the articulation joint. Hence, the driver's input is mostly based on the vehicle's response rather than the trailer. These two basic reasons have made vehicle-trailer combinations more prone to loss of control and cause of road accidents.

Before addressing the problem of stability control, it is beneficial to study the stability of a vehicle-trailer system. The purpose of stability analysis is to find dynamic conditions or regions of a vehicle-trailer system in which stability is inherently guaranteed. Basically, three main motion modes can be identified for a vehicle-trailer system. These modes are rollover, trailer swing known as snaking, and jackknife. The last two motion modes can be generally categorized as the yaw instability which is the main focus of this thesis. The yaw instability has been widely studied in the literature which most predominant ones are provided in the following paragraphs.

For road vehicles, yaw stability is basically attributed to the cornering force in the lateral direction produced by tire/road friction at the footprint of a tire known as contact patch [6, 7]. Generally, the cornering force is affected by various factors including normal load, tire lateral slip angle, the friction coefficient between tire and road, etc. Assuming that other factors are fixed under a given maneuver, the cornering force is only a function of the tire lateral slip angle. In low lateral acceleration maneuvers, the cornering force of tires is proportional to its lateral slip angle. However, as the lateral acceleration increases, tires show a nonlinear behavior. Once the tire lateral slip angle reaches a threshold, the cornering force approaches its maximum possible value and beyond that, the tire saturates. This saturation may cause the vehicle to lose its yaw or roll stability [8].

Based on the saturated axle, two distinct instability modes are defined including snaking and jackknife instabilities. If the tires of a trailer saturate, snaking oscillation occurs causing the trailer to move side to side divergently [6]. The origin of this saturation can be towing speed, uneven road condition, a gust of wind, inappropriate hitch adjustment, etc. [1]. On the other hand, if the rear tires of a vehicle saturate, a jackknifing occurs which means the hitch angle increases divergently without oscillation such that after a critical limit, drivers may not be able to stabilize the vehicle by steering or braking [6, 9].

From the control point of view, a vehicle-trailer is a system of fourth-order which has two types of instability including saddle-node bifurcation known as static and Hopf bifurcation known as dynamic [9, 10, 11]. In the static form of instability, the state variables increase divergently without oscillation while in the dynamic form, a vehicle experiences divergent oscillations. Making a connection between the control and the vehicle dynamics point of view, static and dynamic instabilities cause jack-knife and snaking oscillation respectively.

In this regard, Hac et al. [9] and N Zhang [12] investigated the yaw plane stability considering the static stability through analysis, simulation, and vehicle testing in different loading conditions and longitudinal velocities. Based on these studies, the parameters of the vehicle and the normal load on the hitch point are the only parameters that affect the static stability. Regardless of the fact that passenger cars are normally designed with a

positive under-steer gradient, for a vehicle-trailer system, the under-steer coefficient might even become negative at particular operating points [13]. The authors believe that the under-steer coefficient may change due to the CG location of a trailer. More precisely, with the assumption that the cornering stiffness of tires is constant, the under-steer tendency decreases when the CG location of a trailer is ahead of the trailer axle and increases when the CG location is behind the trailer axle in comparison with a single-unit vehicle.

The dynamic stability analysis was discussed in [1, 9, 12, 14]. In these studies, plotting the pole location of lateral dynamic models and the damping coefficient of the vehicle were used as a function of longitudinal velocity. The results show that for a single-unit vehicle if the vehicle is under-steer and linear, theoretically, the vehicle remains stable over the entire range of speed but for a vehicle-trailer system as the speed increases, one of two damping ratios reduces, and after a specific velocity becomes negative and leads to the instability of the vehicle-trailer system. In the dynamic stability, the mass of a trailer alone does not change the stability significantly in comparison with the yaw inertia e.g. the load distribution [15]. Moving CG location toward the end of a trailer makes the vehicle less stable due to the damping reduction which contradicts the static stability improvement [9]. This means the CG location needs to be compromised to cover both the static and dynamic stability requirements.

As discussed, the yaw instability mostly happens when the tires go beyond their linear regions and are saturated. Therefore, [16, 17, 18, 19, 20, 21, 22] have conducted different studies on the nonlinear analysis of single-unit vehicle dynamics. For articulated vehicles, tire saturation causes large articulation and lateral slip angles which are the main reasons for the yaw instability and fatal accidents. As a result, the nonlinear analysis of a vehicle-trailer system can provide a better understanding of its dynamic behavior, especially at the stability margins.

T. Sun et al. [23] provided a non-linear bifurcation stability analysis of articulated vehicles based on phase-plane behavior theorem and Lyapunov stability analysis theory. Also, they designed an active trailer differential braking controller to prevent unstable motions including yaw and roll instabilities using the fuzzy logic technique. In this research, the longitudinal velocity, steering angle, and trailer payload are considered varying parameters and a 6DOF nonlinear yaw-roll model is used for the analysis. Simulation results have confirmed the outcomes that have been widely reported in the literature through linear stability analysis such as the critical speed concept and the rearward amplification [1, 10, 12, 24].

2.2 Active Safety Systems

To stabilize tractor/vehicle-trailer systems different actuators have been used in the literature including differential braking on vehicle/trailer, and active trailer steering. Simulation and experimental results show that all of these active safety systems can be effective in stabilizing tractor/vehicle-trailers. The most prominent studies are reviewed in the following paragraphs.

Differential braking, as a form of direct yaw control (DYC), is extremely popular in vehicles owing to a large corrective yaw moment achieved by this system especially in high lateral accelerations [25, 26]. This corrective yaw moment allows the vehicle of a vehicle-trailer system to prevent the snaking instability effectively [9, 27]. But, differential braking intervention can make the driver uncomfortable. In order to minimize the activation of braking and increase the safety margin, Y. Zhao et al [28] conducted a study to integrate active front steering and differential braking due to a smooth intervention of AFS in low lateral accelerations (the linear region of a tire) and better performance of differential braking in critical situations (the nonlinear region of a tire) [29]. The proposed slide mode controller applies a compensated yaw moment to push the vehicle to follow the desired yaw rate. This controller has two loops. In the inner loop, the steering angle is used to compensate yaw rate and when the yaw error exceeds a predefined threshold, in the outer loop, differential braking is engaged. Based on the simulation results, the designed integrated controller is able to improve the stability of the vehicle-trailer system without an insignificant drop in the longitudinal velocity. It should be noted that the uniform braking of the vehicle unit can also be used as an actuator for stability control. But, it not only requires a large speed reduction to bring the vehicle into the stable region but also creates a destabilizing moment acting on the trailer which increases the hitch angle [9].

Trailer differential braking is another actuator used to stabilize a vehicle-trailer system. The main concept of a trailer differential braking controller is to generate a corrective yaw moment on the trailer unit to align it with the vehicle unit e.g. reducing articulation angle [6, 30, 31]. T. Sun et al. designed a trailer differential braking controller using fuzzy logic [23]. The results showed that differential braking on the trailer unit is able to prevent yaw and roll instabilities effectively. They also proposed that a threshold can be identified for the actuator activation using the nonlinear stability analysis. M. Fernández et al. and R. Shamim et al. used different controllers including an error-based controller and a linear quadratic regulator. They also confirmed that trailer differential braking is helpful in stabilizing a vehicle-trailer system.

In conventional tractor-trailer vehicles with non-steering trailers, large tire lateral slip angles produce large lateral forces which can make the path of the trailer rear end deviate

from that of the tractor front end. This deviation is frequently defined as off-tracking and is an important measure for the maneuverability of articulated vehicles. By steering the trailer axle wheels, it is possible to decrease the off-tracking thereby improving the maneuverability, especially at low speed [24]. Active trailer steering (ATS) is also able to improve the stability of a tractor-trailer vehicle in high speed through the lateral acceleration reduction in the trailer [32].

In contrary to non-commercial vehicles, active trailer steering was well developed in commercial vehicles [32, 33, 34, 35]. A. Odhams et al. [24] established two different strategies for low and high speed. In low speed, a kinematic model is used to reduce off-tracking. However, in high speed, a dynamic pendulum model as a linear model of a trailer was derived for a PID controller design. The results showed that active trailer steering along with an appropriate controller is able to reduce the off-tracking as well as stability improvement. They also developed another controller strategy based on optimal preview control to obtain the aforementioned requirements with a better performance [36]. To achieve one controller which improves both low-speed maneuverability and high-speed stability for tractor-trailer vehicles, K. Kural et al. proposed a new control strategy [37]. This controller uses a gain scheduling method to provide optimal performance in the desired range of speed. The results demonstrate both off-tracking and rearward amplification reduction as the indicators of low and high-speed performances respectively. In non-commercial tractor-trailer vehicles, there are also some limited studies that used different controller strategies to stabilize a vehicle-trailer system using active trailer steering. They concluded that this actuation system can also be effective in vehicle-trailer stabilization [6, 30].

2.3 Motion Planning

Over the last few decades, autonomous driving has attracted a lot of attention due to the advent of new technologies such as advanced driving assistance system (ADAS), which provide promising steps toward fully autonomous driving, and increasing demand for a practical solution to minimize the number of road accidents and fatalities accordingly.

There are different control architecture for autonomous vehicle [38, 39, 40], however, Figure 2.1 is the general structure that was implemented on automated vehicles [41]. In this structure, first, the vehicle that is equipped with different sensors including LIDARs, cameras, and radars obtains knowledge about its surroundings. In the perception layer, the received data is used to detect and classify obstacles, identify the appropriate lane, and localize the ego vehicle [42, 43, 44, 45, 46, 47]. The classified information along with possible additional data from communication with infrastructure or other vehicles is fed to

the decision layer. This layer might consist of three different planning modules including global planning, behavioral planning, and local planning. The global planning module finds an optimal route from the current point to the destination considering the traffic flow and road regulations [48, 49, 50]. The behavioral planning module, as the name suggests, specifies the proper driving behavior and set local goals, for example changing the lane or stop request [51, 52, 50]. Based on the information from global planning, behavioral planning, and perception layer, the local planning module, usually called motion planner, provides a local collision-free trajectory [53, 54, 55, 41]. The control layer tries to guide the vehicle along the supplied trajectory both laterally and longitudinally and have appropriate responses to unexpected scenarios such as emergency braking [50, 56]. Finally, the control layer sends the control commands to the low-level controller (Actuation layer) to be transformed into actuator commands. Needless to say that, sometimes, some of these modules and layers are combined and not clearly segregated.

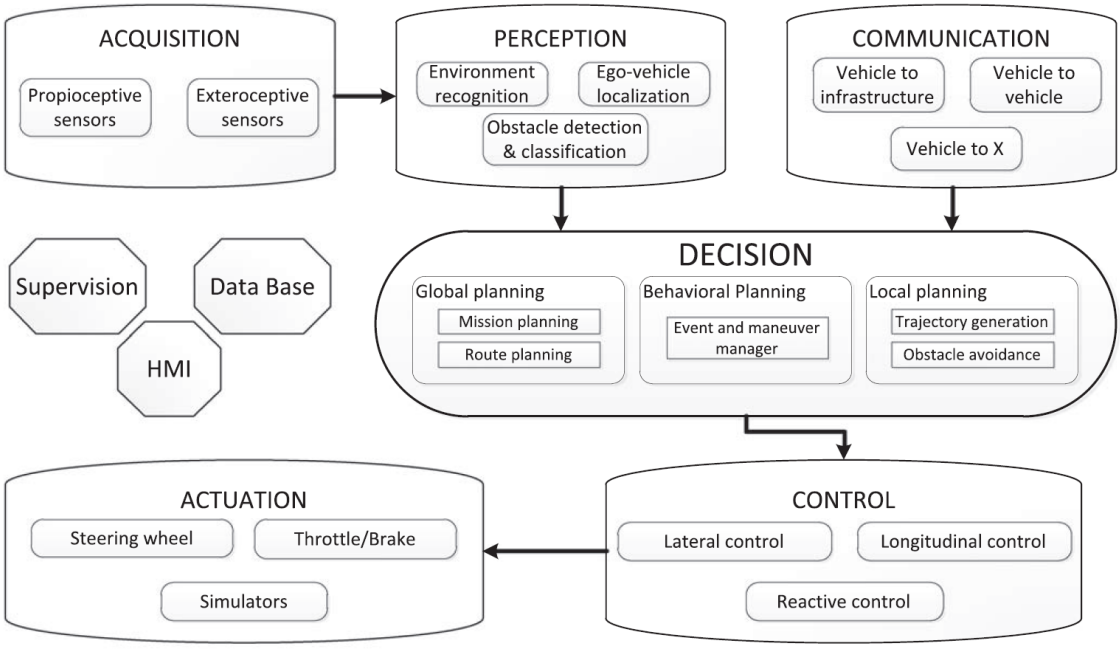

Figure 2.1: General structure for autonomous vehicles [41]

As mentioned, in autonomous vehicles, motion planning is a module that is utilized to generate a safe, comfortable, feasible trajectory from the current state of the vehicle to the goal state which is usually provided by a decision-making hierarchy. Also, the planned

trajectory needs to satisfy some given local, global, and vehicle dynamics constraints, avoid obstacles whether they are static or dynamic, and consider traffic regulations and road lanes. Over the last few decades, numerous studies have been done to address these challenges through proposing various approaches. Generally, the most common motion planning approaches used in autonomous driving can be divided into four major categories: interpolating curve planning approaches, sample-based approaches, optimization-based approaches, and graph search-based approaches.

In interpolating curve planning, in a specific range, a new set of data along with the reference path is defined which is obstacle free and smooth. There are different techniques for generating the trajectory and its smoothness including polynomial curves [57, 58, 52], spline curves [59, 60, 61], and lines and circles [62, 63].

Sample-based approaches randomly sample the environment space to construct a collision-free path, which is not optimal, from the current state of the vehicle that is described by its position and the heading to the destination [64, 39]. Rapidly exploring Random Tree (RRT) and its variants are widely used for path planning in this category [41]. This algorithm grows randomly in a bounded navigation area and among the generated trajectories the best solution is selected. This process is fast and can also consider non-holonomic constraints and collision avoidance as the automated driving requirements [10], however, its performance is not appropriate due to its jerky response [41]. To overcome the limitations of this approach, Lim et. al, integrated this method with an optimization approach. In the proposed planner, the sample-based approach provides the trajectory tracking by selecting the optimal one among all available collision-free candidates which are modeled by a quintic polynomial. Also, for the longitudinal movement, a linear MPC is utilized as an optimized solution [65].

Recently, optimization-based methods are widely used in automated driving path planning. The aim of these approaches is to minimize a mathematically formed cost function [66, 67, 68]. This cost function might be solved by linear or nonlinear programming depending on the complexity of the problem. The solution to this method, contrary to the previous one, is optimal and can be constrained with respect to environmental and vehicle constraints. Model Predictive Control (MPC) is widely used in the literature as an optimized motion planning method. The non-linear MPC has a high computation cost and it is hardly possible to be implemented in real-time [56]. Therefore, this cost function is simplified to a linear quadratic MPC problem considering a linear dynamic model along with linear constraints [69, 70]. Also, in [71], Yi et al., and in [72], Gutjahr et al., developed MPC-based trajectory planning with collision avoidance capabilities in critical driving maneuvers and computationally efficient for real-time applications.

Among optimization-based methods, although the potential field approach is not solely used as a path planner in automated driving, it is usually integrated with other methods such as MPC to provide an optimal path [53, 73, 74]. In the potential field, the repulsive forces and attractive forces are virtually considered on the obstacles and the goal position, respectively. In this method, the strength of the potential filed prioritized obstacle avoidance and the ultimate path is planned based on the overall potential filed and following the direction of the steepest gradient. In [54], a path is generated by the potential field method to avoid obstacles. Then, the planned path is used to formulate a multi-constraint MPC for providing stability of the vehicle. The same strategy is used by Huang et al. in [75, 55], however, they use a modified potential field called elaborated resistance for motion planning. In these papers, MPC has exploited as a path tracking controller due to its prediction nature and unique capabilities for handling constraints. It is clear that the motion planning of an autonomous vehicle is nonlinear and non-convex. However, solving this nonlinear problem is computationally expensive, therefore, Rasekhipour et al. in [53] proposed an optimal control method that its quadratic cost function includes both potential fields and an MPC with the vehicle and environmental constraints. In this method, both trajectory planning and tracking are combined in a unified manner. Although the research results show that potential field and MPC can be integrated as a motion planning module, the potential field method suffers from getting stuck in local minima and oscillatory motion planning when several obstacles exist [76].

In graph search-based approaches, the environment is mapped to a 2D grid (cell), and the search algorithm visits the different cells and provides the shortest path as a solution [76, 77]. The most well-known search-based algorithms are the Dijkstra algorithm [78], state lattice algorithm [3], [4], and A* algorithm. The Dijkstra algorithm is fundamentally a graph-search based algorithm that finds the shortest path between the current and the goal locations while visiting different cells [79]. the cost/weight of each cell is usually calculated based on the length or travel time. This algorithm has been implemented in real time tested on different autonomous vehicle platforms [80, 81]. This algorithm is not effective and fast as the size of the problem increases. In the state lattice algorithm, a search is conducted on a set of lattices which can guide from its current position toward the goal point, and a path with the lowest cost function is selected [82, 83]. Among these methods, A* and its variations are more popular than others as it enables a fast node search due to utilizing heuristic technique [84]. This technique prevents the search algorithm from visiting unpromising nodes/vertices of a graph and this way the calculation time reduces significantly [76]. Figure 2.2 compares the A* with Dijkstra algorithms and shows how the heuristic technique reduces search space significantly. In [85], Ziegler and et al. implemented the A* method to navigate a car-like robot considering its kinematic constraints

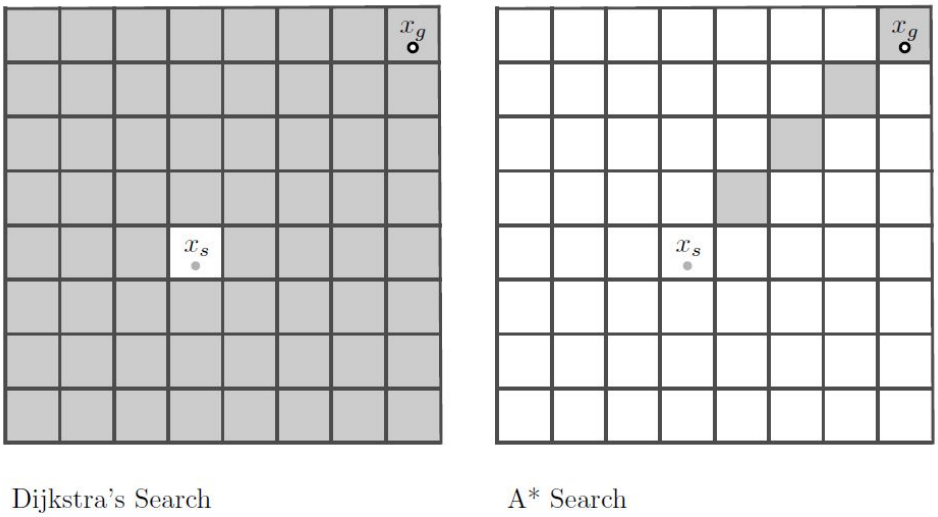

Figure 2.2: The effect of heuristic technique in search improvement [76]

in an unstructured environment for precise parking, narrow turns, and navigation in long distances. Also, a variation of this algorithm called hybrid A* was also served as a fast path planner in autonomous vehicles [64, 76]. This variation although follow the same search algorithm among nodes, a continuous space is searched rather than discrete cells [86, 85]. In all of these studies, only the kinematic models are used and dynamic limitations of the vehicle are neglected.

As mentioned, One of the most important features of an appropriate motion planner is feasibility. In other words, the vehicle needs to able to follow the trajectory generated by the motion planner. In this regard, having an accurate model that is able to predict the behavior of the vehicle during the planning procedure is crucial. Generally, the vehicle models used in motion planning can be categorized into three main streams: point mass, kinematic, and dynamics models [56]. In point-mass models, the tire model is not considered and the vehicle is only considered a particle that can move laterally and longitudinally. The lateral and longitudinal accelerations of the vehicle can be limited by their corresponding accelerations [55, 87]. Although these bounds might be rather beneficial, they are not obviously sufficient to predict the complex behavior of a vehicle. Kinematic models are also used in motion planning [88, 89, 85]. As these models do not consider tie models, they do not enable an accurate prediction especially at higher speeds or lateral accelerations as well [90].

The vehicle dynamics are highly non-linear mostly due to the non-linearity of the tires.

The linear bicycle model, as the most common dynamic model, exploits a linear tire model and therefore can be easily utilized in control formulations. Although it is a linear model, it is accurate enough to be used as a prediction model in high-speed driving scenarios [73, 91, 54]. However, this accuracy degrades as the vehicle enters the non-linear region of the tries. Therefore, in many studies, the bicycle model is developed using a non-linear tire model such as brush tire model [69] or Pacejka tire model [92] to establish a more precise model even in an operating region close to saturation.

In emergency driving scenarios, regardless of the performance level of the autonomous vehicle, there are some situations in which accident is inevitable as the vehicle operates in a mixed human-driven traffics. In these cases, the motion planner is expected to respond properly and find a solution with the lowest crash severity. To this aim, the obstacles need to be prioritized by an algorithm in which the cost of each trajectory, as a solution of motion planning, is evaluated [93] and the one with minimum cost is chosen. To address this problem, Rasekhipour et al. [53] and Wang et al. [73], proposed an optimal motion planning approach based on the potential field method that is capable of prioritization of the obstacles using different potential fields considering their importance. In [94], Rasekhipour et al. proposed another strategy for considering obstacle priority order by utilizing lexicographic optimization which regulates the objective functions in a multi-objective optimization problem based on their priorities. In this approach, the prioritization is performed by changing the weights of each constraint in an MPC formulation.

2.4 Envelope Control

Minimizing control intervention has always been one of the challenges for designing controllers due to the fact that excessive control interference might be annoying for the driver. For example, Smakman in [95], proposed using a reference region rather than a reference value for yaw rate tracking to minimize the controller's engagement In this regard, developing a controller that provides a systematic approach to minimize the control interference is a promising practice, especially where the control action might be annoying for the passengers like differential braking. In this situation, the controller is expected to affect the drive's command when the vehicle is going to leave the stability region. Thus, both the passenger's convenience and the vehicle stability are considered in the control strategy.

The idea of envelope control is originated from the aviation industry by which the pilot is allowed to control the aircraft without controller intervention but prevented to go beyond the stable region of the aircraft [97]. If the aircraft is about to leave the stable region the controller is engaged to prevent it or bring it back to the stable one in case of entering the

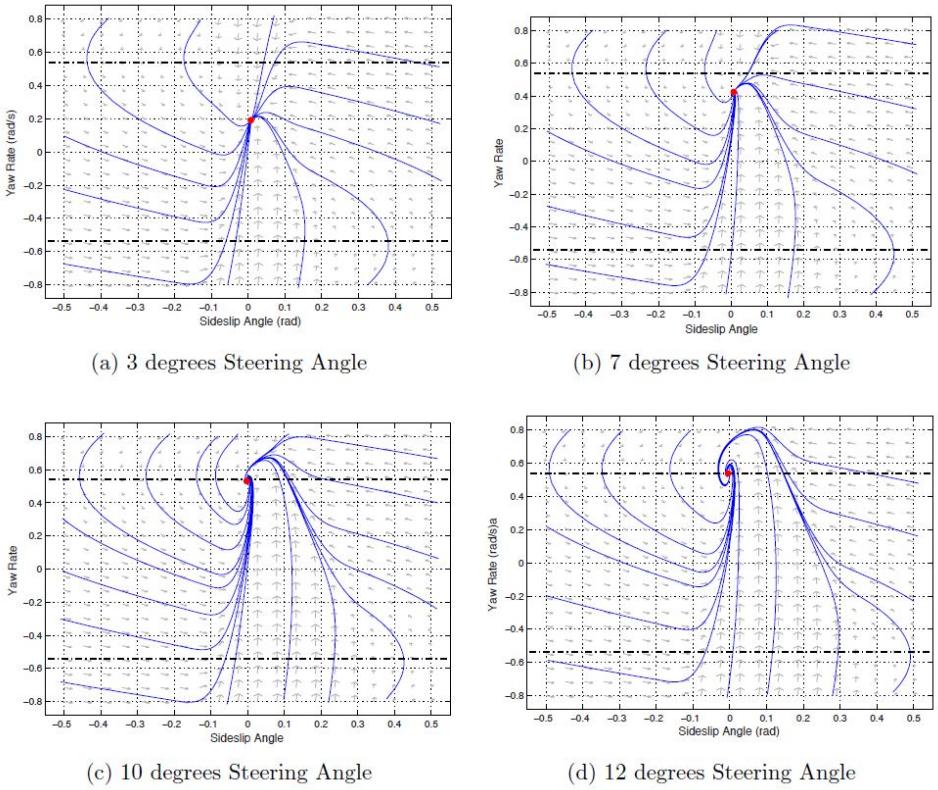

(a) 3 degrees Steering Angle

(b) 7 degrees Steering Angle

(c) 10 degrees Steering Angle

(d) 12 degrees Steering Angle

Figure 2.3: Phase portraits of an under-steer single-vehicle [96]

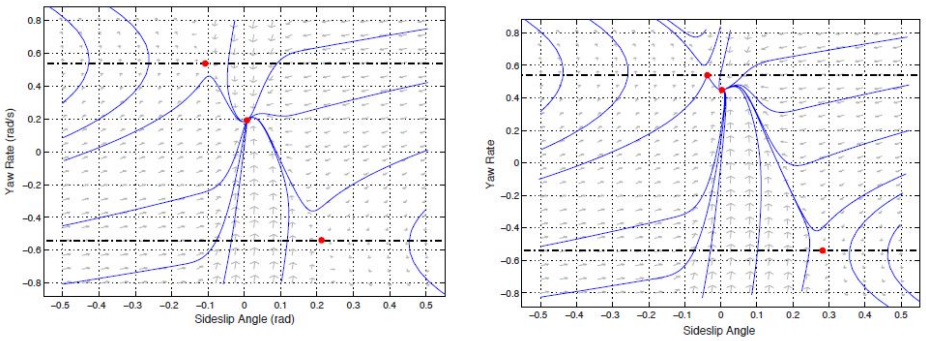

(a) 3 degrees Steering Angle

(b) 7 degrees Steering Angle

(c) 10 degrees Steering Angle

(d) 12 degrees Steering Angle

Figure 2.4: Phase portraits of an over-steer single-vehicle [96]

unstable region. This is mainly performed by imposing constraints on state variables of the aircraft such as speed and rotation angles. Recently, this strategy has been extended to a single-vehicle yaw stability control by Beal et al. [3]. To find this envelope accurately, the non-linear behavior of the tires should be considered the main source of the non-linear behavior of vehicles. In this regard, the authors exploited 2D phase portraits of the vehicle which are able to show the nonlinear behavior of the vehicle, its equilibrium points, and the stable region known as the region of attraction. In this study, it was observed that when a single-vehicle is under-steer, there is always a stable equilibrium point that the stable trajectories converge to, Figure 2.3 and when the vehicle is over-steer the stable equilibrium point disappears when the steering exceeds a certain value and the vehicle becomes unstable, Figure 2.4. Based on these observations, they defined bounds on state variables, sideslip angle and yaw rate, and developed an MPC controller to correct the driver's input and keep the vehicle inside the safe envelope. The experimentally validated results showed that the MPC-based envelope controller was able to keep the vehicle stable in real-time and was also robust in the presence of disturbances. Envelope control was also used by Ni et al. [98] on an autonomous vehicle to follow the target path using control action integration. Similar to the idea presented by Beal, C. Bobier et al. in [99, 100, 101] suggested a different envelope according to yaw acceleration nullclines and the maximum steering angle in order to obtain higher possible yaw rates and ensure that the designed controller does not interfere with vehicle natural stable transient. Later, in [102], Beal et al. extended 2D phase portraits to 3D ones to reflect the coupled lateral and longitudinal dynamics by considering longitudinal speed as a new variable. In this study, they introduced a stable curve called stem that appeared in 3D phase portraits. In [103], C. Tang and A. Khajepour proposed a stability control strategy for narrow tilting vehicles using envelope approach. In this strategy, an MPC controller is designed to constraint the roll angle inside a roll envelope rather than tracking zero to not only keep the vehicle stable but also provide comfort and prevent excessive control effort.

2.5 Control Allocation

To enhance safety, fault tolerance, actuator sharing, and maneuverability, vehicles might have redundant actuators or sensors. In addition, in vehicle-trailer systems, since the vehicle unit might tow different trailers equipped with different safety systems, a controller that can handle different actuator configurations is a necessity. Although this redundancy increases controller performance and provides a multi-objective control scheme, it leads to complex control strategies. Also, considering all possible control actions in a unified struc-

ture drastically increases computation time, especially in MPC. Therefore, a proper control action coordination technique that is able to address all the aforementioned concerns has attracted considerable attention.

To practically solve the control action distribution in over-actuated systems, Control Allocation (CA) has been frequently proposed in the literature in different fields of study [104, 105, 106]. Mainly, CA is an intermediate level between high-level and low-level controllers that optimally defines the share of each actuator based on their capacity (bounds), health, and control objective preference [106, 105]. In this structure, to reduce the size of the problem and accordingly the computation time, usually a virtual control action is devoted to each degree of freedom that is intended to be controlled [107]. The high-level controller considers these virtual control actions as the plant control actions and provides the value for each virtual control action by solving the objective function. Then, CA maps these virtual control actions to an actuator command vector based on the allocated weights and actuator bounds [106].

In [108], Wang et al. proposed a new strategy for dynamics control of an over-actuated vehicle called Coordinated Reconfigurable Vehicle Dynamics Control (CRVDC) to constraint combined tire slip angle which is inherently non-linear and also reduces the computational burden of the optimization solving process. In this strategy, a high-level controller provides the generalized forces and moments at CG as the virtual control actions, and then, in the low-level, the lateral and longitudinal forces of the tires are manipulated through braking/traction/steering forces to track the desired lateral and longitudinal slips. Kasinathan et al. [26], used a control structure called Holistic Cornering Control (HCC) originally introduced in [109] that ensures the vehicle stability while following the target path. Similar to [108], first, the required CG forces and moments are calculated and then the HCC module optimally distributes those at each corner of the vehicle on each wheel in the form of lateral and longitudinal forces. Since HCC is fundamentally formulated as a constrained optimization problem, the minimum and maximum allowable forces for each tire are also considered. Nahidi et al. [107], followed the same approach to develop a modular integrated controller for an electric vehicle. In this study, a low-level distributor similar to the HCC module is exploited to map the CG-based forces and moments supplied by the high-level controller to a set of commands for the actuators which are electric motors for each wheel. A similar CA approach in [110] is extended to an autonomous vehicle equipped with four independent electric motors for each wheel. In this research, an adaptive sliding mode controller acts as the high-level which provides the steering angle and additional yaw moment for adjusting yaw moment. The adjusting yaw moment is obtained through manipulating the longitudinal force of each tire regulated by the CA approach. Tang et al. proposed an optimal CA for narrow tilting vehicles to supply actuator selection flexibility

rather than modifying the controller structure entirely [111]. In this control structure, the high-level controller, which handles rollover stability and control effort, provides the necessary forces for keeping the vehicle inside the roll envelope, and then, the distributor optimally transforms them to actuator commands.

2.6 Summary

In this chapter, first, the literature on vehicle-trailer stability analysis was reviewed. It was discussed that two main yaw instability modes are characterized for vehicle-trailer systems, snaking and jackknifing. A vehicle-trailer system has a tendency to jackknifing where the CG of the trailer is close to the hitch point and the normal load on the hitch point is the only parameter that affects it. On the other hand, moving the CG location toward the end of the trailer reduces the damping coefficient of the combined vehicle and might make it negative for speeds above a certain value which causes snaking instability. The reviewed studies were mostly based on linear analysis, however, the non-linear analysis of these types of vehicles can provide promising control strategies which is the aim of this research.

In addition, the active safety systems used in tractor/vehicle-trailer stabilization along with control approaches were explored. Differential braking on the vehicle unit was the most common method to stabilize the combined vehicle. This control action was also integrated with AFS to prevent its annoying interventions in low lateral accelerations. Trailer differential braking has also been utilized as an active safety system and it was shown that this control action is able to make the vehicle stable. Additionally, the application of active trailer steering on tractor-trailer stabilization was discussed. This control action, however, is more common on commercial tractor-trailer vehicles to reduce rearward amplification and off-tracking.

The literature on motion planning was reviewed in four major categories, interpolating curve planning, sample-based, optimization-based, and graph search-based. In interpolating curve planning approaches, a set of new paths along with the target path is generated and one of them is selected. In sample-based approaches, some random paths are generated and the best solution is chosen. However, its performance is not appropriate due to its jerky response. Optimization-based techniques have been recently developed to provide an optimal solution for motion planning problems. These methods are mostly non-linear and computationally expensive. In this regard, some new techniques have been proposed to linearize the corresponding cost function to reduce the computation time for real-time implementations. In graph search-based approaches, the environment is discretized and

a search algorithm finds the shortest path from the vehicle location to the goal point. Among these proposed methods, the hybrid A* algorithm has been more popular for autonomous vehicles as it can consider non-holonomic constraints and it is fast enough to be implemented in real-time. In the reviewed literature on motion planning, the effect of a trailer and the requirements of a vehicle-trailer system were not considered. In this thesis, a motion planning module is developed to take the stability and off-tracking concerns of vehicle-trailer systems into consideration.

In this chapter, envelope control and control allocation were discussed as well. The idea of the envelope control is that the control action is engaged when the vehicle is about to leave the stable region to prevent any unnecessary control intervention. This control methodology has been investigated for single-vehicles and it has been shown that it is able to effectively prevent instability. To define the stable region, however, the non-linear behavior of the vehicle needs to be studied. The control allocation technique has been widely used for systems that are equipped with multiple control actions. This technique is able to optimally map the required control actions to the available actuators with respect to given actuator constraints or capabilities.

Chapter 3

Stability Envelope Development for Vehicle-Trailer Systems

In this chapter, the stability of a vehicle-trailer system is comprehensively examined using the linear and phase plane methods which ultimately leads to developing a stability envelope for vehicle-trailer systems. To this aim, a non-linear planar bicycle model of a vehicle-trailer system is developed with 3DOF to capture the non-linear lateral dynamic behavior of the vehicle mainly coming from the tires and large hitch angles. To reduce the complexity of the equations of motion, the trailer has only one axle. However, if a trailer has more than one axle, it can be modeled as an equivalent one axle trailer as explained in [21]. Also, an affine bicycle model is derived based on this non-linear model. The affine model is utilized for controller design in the next chapter and linear stability analysis later in this chapter.

3.1 Tire Model

Tires provide the main lateral and longitudinal forces needed for a vehicle to do stable accelerating, braking, and turning maneuvers. In this regard, the properties of a tire significantly affect the handling of a vehicle. Providing different safety and handling features due to different driving requirements have made a tire a very complicated product. Therefore, developing a model from this complex product with all the details is not computationally efficient and consequently cannot be used in real-time applications. As a result, tire models used in controller designs usually capture only the most important character-

istics of a tire to prevent computational problems and be accurate enough at the same time.

The tire model used in this thesis is a brush model, originally presented by Fiala and modified by Pacejka. This model has been frequently used for model-based controller designs [112, 99, 113]. The brush model utilizes the concepts of force demand and availability to determine the total available force over the footprint area called the contact patch. The total available force in the contact patch is limited by the normal load and road friction. In addition, this model has a special mechanism which is explained later to consider the effects of lateral-longitudinal force coupling known as combined slip. In general, the total force on a tire is a vector sum of the lateral and longitudinal force components and must be less than the total available force as demonstrated in Figure 3.1. This concept is called friction circle and is defined as

$$F^t = \sqrt{(F^x)^2 + (F^y)^2} \leq \mu F^z \tag{3.1}$$

where F^t is the total available force, F^x is the longitudinal force, F^y is the lateral force, F^z is the normal load, and μ is the road friction.

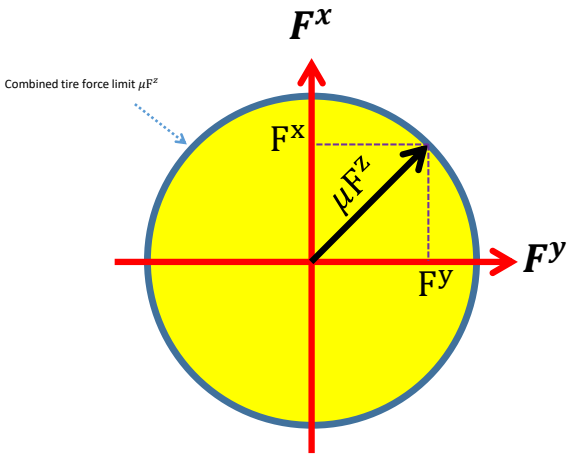

Figure 3.1: Combined tire force limits

The lateral tire force using the brush model is parametrized by the linear cornering stiffness C_α, the normal load F_z, the road friction coefficient μ, and a derating factor η that is added to reduce the lateral force capability of the tire due to the presence of

longitudinal force. The mathematical expression of the brush model is as follows

$$F^y = \begin{cases} C_\alpha t - \frac{C_\alpha^2}{3\eta\mu F^z}|t|t + \frac{C_\alpha^3}{27\eta^2\mu^2 F^{z2}}t^3, & |\alpha| < \alpha^{sat} \\ \eta\mu F^z \text{sign}(\alpha), & \text{otherwise} \end{cases} \tag{3.2}$$
$$t = \tan(\alpha)$$

where α^{sat} is the saturation lateral slip angle of the tire at which the maximum lateral tire force is achieved and defined as

$$\alpha^{sat} = tan^{-1}\left(\frac{3\mu\eta F^z}{C_\alpha}\right) \tag{3.3}$$

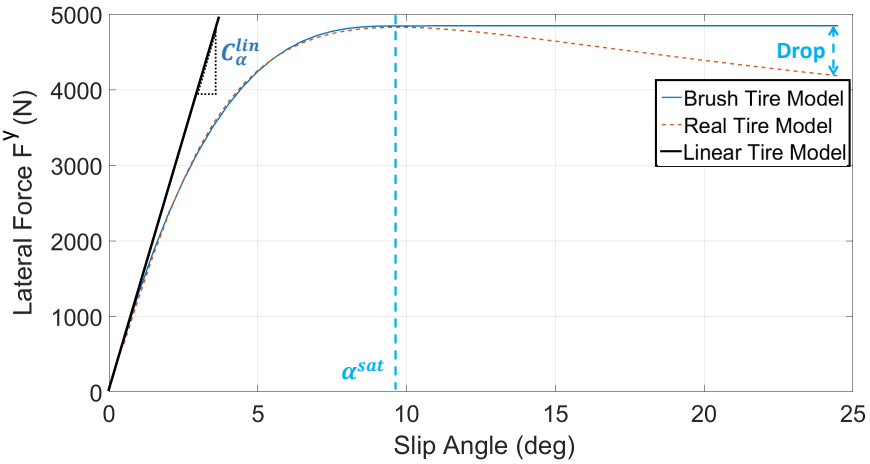

Figure 3.2: Tire models

In this tire model, as presented in Equation (3.2), when the lateral slip angle exceeds the saturation angle, the lateral force remains unchanged and does not drop like a real tire (Figure 3.1). This is a reasonable assumption because the controller should prevent the vehicle from entering the saturation region and the operating point of all axles is forced to stay in the non-sliding regions. As mentioned, the effect of the combined slip in lateral force is modeled using a derating factor [70] that is expressed as

$$\eta = \frac{\sqrt{(\mu F^z)^2 - (F^x)^2}}{\mu F^z} \tag{3.4}$$

This technique has a good performance when the total available force is significantly larger than the longitudinal force. In other words, μF^z should be bounded away from zero which is valid in this thesis.

3.2 Non-Linear Vehicle-Trailer System Model

A vehicle-trailer system consists of a towing unit and a towed unit which are connected at an articulation joint called hitch point. Figure 3.3 illustrates the free body diagram of a planar bicycle model of a vehicle-trailer system with 3DOF when the longitudinal velocity of the vehicle is u_v^x. For this model the considered degrees of freedom include 1) the lateral motion of the vehicle 2) the yaw motion of the vehicle and 3) the hitch angle. Also, it is assumed that the longitudinal velocity is positive, and, the pitch and the body-roll of the vehicle and the trailer have been neglected. Studies show that these assumptions are valid for yaw stability analysis and are in good agreement with other models with more degrees of freedom [14].

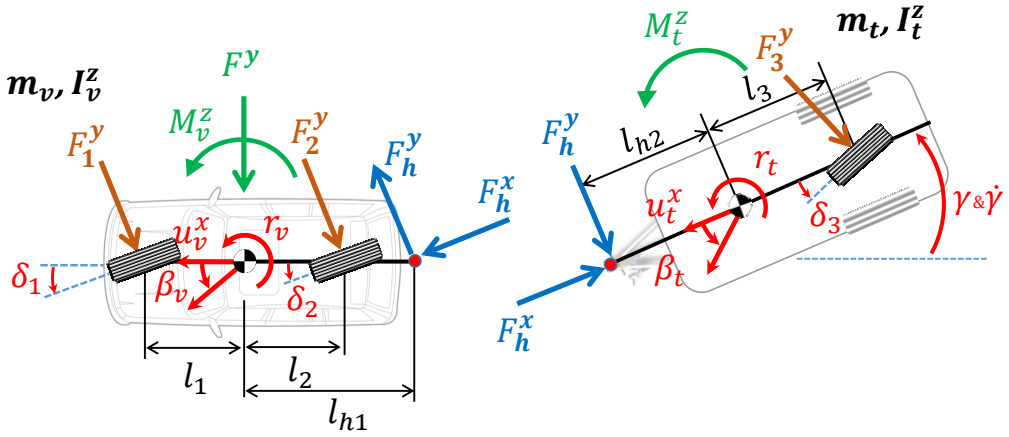

Figure 3.3: Free body diagram of a planar bicycle model for stability analysis of a vehicle-trailer vehicle

From Newton's law of dynamics, the non-linear equations of motion for the vehicle-trailer system are expressed as follows

$$m_v u_v^x(\dot{\beta}_v + r_v) = F_1^y cos(\delta_1) + F_2^y - F_h^y \cos(\gamma) + F_h^x \sin(\gamma) + F^y \tag{3.5}$$

$$I_v^z \dot{r}_v = l_1 F_1^y cos(\delta_1) - l_2 F_2^y + l_{h1} \left(F_h^y \cos(\gamma) - F_h^x \sin(\gamma)\right) + M_v^z \tag{3.6}$$

$$m_t u_t^x(\dot{\beta}_t + r_t) = F_3^y + F_h^y \tag{3.7}$$

$$I_t^z \dot{r}_t = -l_3 F_3^y + l_{h2} F_h^y + M_t^z \tag{3.8}$$

The hitch coupling equations are

$$u_t^x = u_v^x \cos(\gamma) + (u_v^x \beta_v - l_{h1} r_v) \sin(\gamma) \tag{3.9}$$

$$r_t = \dot{\gamma} + r_v \tag{3.10}$$

$$\beta_t = -\frac{l_{h2} r_t + u_v^x \sin(\gamma) + (u_v^x \beta_v - l_{h1} r_v) \cos(\gamma)}{u_t^x} \tag{3.11}$$

All parameters mentioned in the above equations are described in Table 3.1. Respectively, F_h^x and F_h^y are the longitudinal and lateral internal forces of the vehicle and the trailer in the trailer coordinate. F_i^y is the lateral force at the i^{th} axle and the index $i = 1, 2, 3$ indicates the axle number. These lateral forces generated by tires at axles are highly non-linear in nature, especially at high lateral accelerations. Hence, a non-linear brush model is used to capture this effect for providing sufficient accuracy. Moreover, for each degree of freedom one virtual control action is assigned to provide a general control structure, as discussed in Chapter 4, F^y, M_v^z, M_t^z for the lateral motion of the vehicle, the yaw motion of the vehicle, and the hitch angle, respectively.

The non-linear equations of motion can be written in state space form by eliminating the internal forces, F_h^x and F_h^y. This non-linear model is stated by the following equation

$$\dot{x} = f(x, F, V) \tag{3.12}$$

where x is the state vector with four variables, $x = [\beta_v \quad r_v \quad \dot{\gamma} \quad \gamma]^T$, F is the vector of lateral tire forces, $F = [F_1^y \quad F_2^y \quad F_3^y]^T$, and V is the vector of virtual control actions, $V = [F^y \quad M_v^z \quad M_t^z]^T$.

Table 3.1: Parameter description for the vehicle-trailer bicycle model.

Parameter	Description
m_v & m_t	Mass of vehicle & trailer
I_v^z & I_t^z	Yaw inertia of vehicle & trailer
l_1	Distance from axle 1 to the CG of vehicle
l_2	Distance from axle 2 to the CG of vehicle
l_{h1}	Distance from hitch point to the CG of vehicle
l_3	Distance from trailer axle to the CG of trailer
l_{h2}	Distance from hitch point to the CG of trailer
u_v^x & u_t^x	Longitudinal velocity in vehicle & trailer coordinates
u_v^y & u_t^y	Lateral velocity in vehicle & trailer coordinates
r_v & r_t	Yaw rate of vehicle & trailer
β_v & β_t	Sideslip angle of vehicle & trailer
γ & $\dot{\gamma}$	Hitch angle& its rate
δ_1 & δ_2 & δ_3	Steering angle of first & second & third axle
T_v & T_t	Track width of vehicle & trailer

3.2.1 Affine Bicycle Model

It is known that at higher lateral accelerations the linear tire model does not provide enough accuracy to predict the lateral behavior of the vehicle. Thus, to preserve both the non-linearity of the tires (direct consideration of the tire saturation) and to prevent the model complexity, the tire model is linearized at each time step about the operating lateral slip angle. This process is demonstrated in Figure 3.4 and expressed as

$$F^y = \bar{C_\alpha}(\alpha - \bar{\alpha}) + f^y(\bar{\alpha}) \tag{3.13}$$

The equations of motion of the affine bicycle model are developed using the non-linear model with small angle assumption (small γ and δ). In addition, the lateral force F_i^y is expressed by the linearized tire model. To obtain the lateral force of each axle, the lateral slip angles are needed which are expressed as

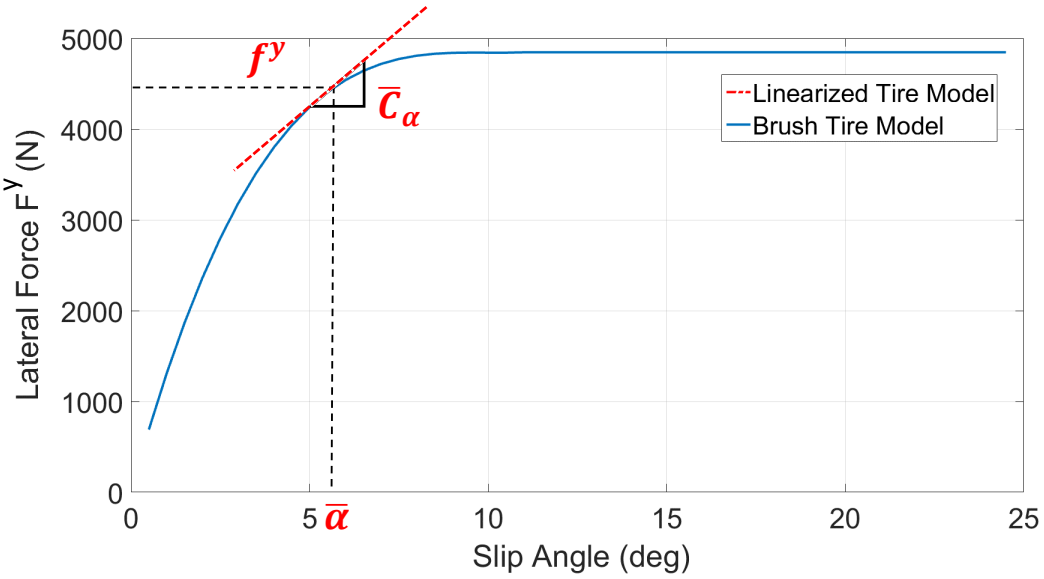

Figure 3.4: Linearizing tire model around lateral slip angle operating point

$$\alpha_1 = \delta_1 - \left(\beta_v + \frac{l_1 r_v}{u_v^x}\right) \tag{3.14}$$

$$\alpha_2 = \delta_2 - \beta_v + \frac{l_2 r_v}{u_v^x} \tag{3.15}$$

$$\alpha_3 = \delta_3 - \beta_t + \frac{l_3 r_t}{u_t^x} \tag{3.16}$$

where α_1, α_2, α_3 represent the lateral slip angle of axles 1, 2, and 3, respectively. As a result

$$F_1^y = \bar{C}_{\alpha 1}(\alpha_1 - \bar{\alpha}_1) + f^y(\bar{\alpha}_1) = \bar{C}_{\alpha 1}\delta_1 + \bar{C}_{\alpha 1}\left(-\beta_v + \frac{l_1 r_v}{u_v^x}\right) + \bar{C}_{\alpha 1}\bar{\alpha}_1 + f^y(\bar{\alpha}_1) \tag{3.17}$$

$$F_2^y = \bar{C}_{\alpha 2}(\alpha_2 - \bar{\alpha}_2) + f^y(\bar{\alpha}_2) = \bar{C}_{\alpha 2}\delta_2 + \bar{C}_{\alpha 2}\left(-\beta_v - \frac{l_2 r_v}{u_v^x}\right) + \bar{C}_{\alpha 2}\bar{\alpha}_2 + f^y(\bar{\alpha}_2) \tag{3.18}$$

$$F_3^y = \bar{C}_{\alpha 3}(\alpha_3 - \bar{\alpha}_3) + f^y(\bar{\alpha}_3) = \bar{C}_{\alpha 3}\delta_3 + \bar{C}_{\alpha 3}\left(-\beta_t - \frac{l_3 r_t}{u_t^x}\right) + \bar{C}_{\alpha 3}\bar{\alpha}_3 + f^y(\bar{\alpha}_3) \tag{3.19}$$

Eliminating F_h^y from Equations (3.5), (3.6), and (3.8), using Equation (3.7), and then substitution of Equations (3.10) and (3.11), and the above lateral forces into these equations, yields a set of differential equations that can be written in a state-space form as

$$\dot{x} = \mathbf{M}^{-1}(\mathbf{A}x + \mathbf{B}_1 V + w), \quad y = \mathbf{C}x \tag{3.20}$$

where

$$\begin{aligned} w =& \mathbf{F}f^y + \mathbf{L}\bar{\alpha} + \mathbf{B}_2\Delta \\ f^y = \begin{bmatrix} f_1^y & f_2^y & f_3^y \end{bmatrix}^T, \quad \bar{\alpha} = \begin{bmatrix} \bar{\alpha}_1 & \bar{\alpha}_2 & \bar{\alpha}_3 \end{bmatrix}^T, \quad \Delta = \begin{bmatrix} \delta_1 & \delta_2 & \delta_3 \end{bmatrix}^T \end{aligned} \tag{3.21}$$

Matrices $\mathbf{M}$, $\mathbf{A}$, $\mathbf{B_1}$, $\mathbf{B_2}$, $\mathbf{C}, \mathbf{F}$, and $\mathbf{L}$ are defined in Appendix A.1.

3.3 Stability Analysis

In this section, the lateral stability of the vehicle-trailer system is evaluated using the characteristic equation. For a vehicle-trailer system, two bifurcations can be distinguished including saddle-node bifurcation and Hopf bifurcation. In the saddle-node bifurcation, known as static instability mode, one real eigenvalue goes to the right-hand side of the s-plane (see Figure 3.5-(a)). In this condition, the state variables of the system, like yaw rate, increases divergently without oscillation from its original equilibrium position shown in Figure 3.5-(b). From the vehicle dynamics point of view, this type of instability is called jackknife and happens when the rear tires of the vehicle saturate and are not able to provide enough lateral force. This saturation may happen due to high normal loads or applying torque for accelerating or braking while cornering. However, in the Hopf bifurcation which is also called dynamic instability mode, a complex conjugate pair of eigenvalues passes the imaginary axis of the s-plane (see Figure 3.5-(c)). As a result, the damping ratio of the dynamic system becomes negative and this system starts to oscillate divergently [12], [23], similar to the snaking mode, as Figure 3.5-(d) shows. In a vehicle-trailer system, when the rear tires of the trailer saturate it starts to oscillate, and if the vehicle unit resonates this oscillation the snaking instability occurs.

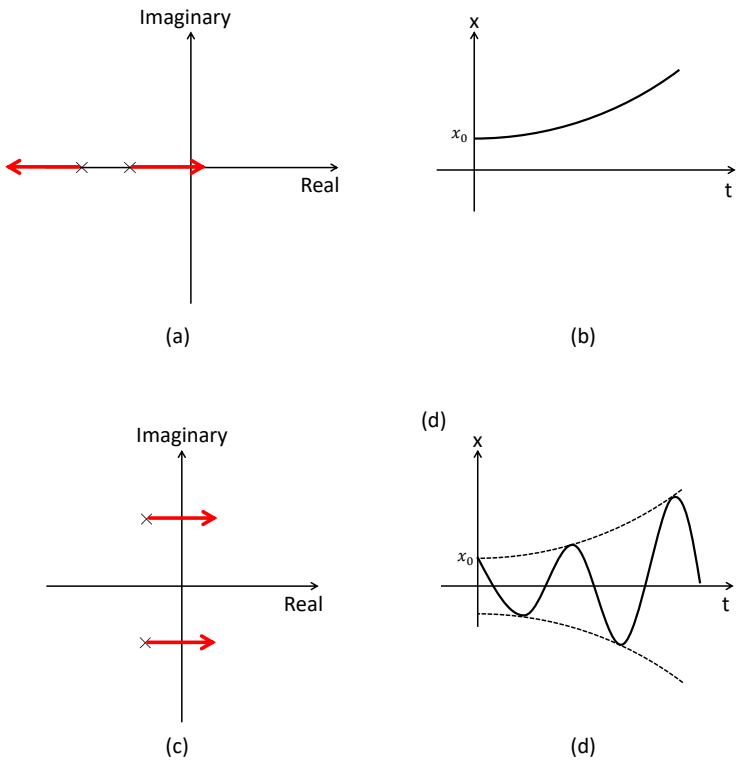

Figure 3.5: Different instability modes, (a) saddle-node bifurcation (b) continuous divergence (c) Hopf bifurcation (d) oscillatory motion

As there are two different instability modes for this kind of vehicle, we need an indicator to categorize these modes. Therefore, two common methods including the characteristic equation and the damping ratio of the system are used to identify them. Regarding the characteristic equation, a system is stable when all roots of the characteristic polynomial have negative real parts. For the vehicle-trailer model presented in the previous section (assuming linear tire, $\bar{C}_{\bar{\alpha}=0} = C_\alpha$, $f^y(\bar{\alpha})$=0), the characteristic equation is given by

$$c_0\lambda^4 + c_1\lambda^3 + c_2\lambda^2 + c_3\lambda + c_4 = 0 \tag{3.22}$$

The c_i is the coefficient of the characteristic equation which has been introduced in [10]. Based on the results of a study conducted by M. Luijten [114], the vehicle-trailer system becomes unstable in jackknife mode when the biggest coefficient c_4 is negative and the longitudinal velocity exceeds the critical value. Also, snaking instability mode happens when c_4 is positive and the highest Hurwitz determinant passes the imaginary axis. c_4 is defined as

$$c_4 = \frac{{C^t}_\alpha C_{\alpha 3}(l_3 + l_{h2})}{u_v^x}\left(-u_v^2\left(\frac{m_t l_3\,(s_1 + l_{h1})}{l_3 + l_{h2}} + m_v s_1\right) + {C^t}_\alpha\left(q_1^2 - s_1^2\right)\right) \tag{3.23}$$

where

$${C^t}_\alpha = C_{\alpha 1} + C_{\alpha 2}, \quad s_1 = \frac{C_{\alpha 1} l_1 - C_{\alpha 2} l_2}{{C^t}_\alpha}, \quad q_1^2 = \frac{C_{\alpha 1} l_1^2 + C_{\alpha 2} l_2^2}{{C^t}_\alpha} \tag{3.24}$$

The under-steer coefficient is defined as a function of the cornering stiffness of tires and the normal load of axles. Based on this concept, if the coefficient is negative and the speed exceeds the critical value, a single-unit vehicle becomes unstable. Adding a trailer significantly modifies the under-steer coefficient of the vehicle unit due to normal load changes [9]. The modified (combined) under-steer coefficient of the vehicle ${k^c}_{us}$ and the critical speed u_v^c (defined in [9]) are expressed as

$${k^c}_{us} = \frac{\frac{W_1}{C_{\alpha 1}} - \frac{W_2}{C_{\alpha 2}}}{g} \tag{3.25}$$

where

$$W_1 = \frac{m_v l_2 - \frac{m_t l_3 (l_{h1} - l_2)}{l_3 + l_{h2}}}{l_1 + l_2}, \quad W_2 = \frac{m_v l_2 + \frac{m_t l_3 (l_{h1} - l_2)}{l_3 + l_{h2}}}{l_1 + l_2} \tag{3.26}$$

$$u_v^c = \sqrt{\frac{-(l_1 + l_2)}{{k^c}_{us}}} \tag{3.27}$$

Using k^c_{us}, c_4 can be rewritten as

$$c_4 = \frac{{C^t_\alpha}^2 C_{\alpha 3}(l_3 + l_{h2})\,(q_1^2 - s_1^2)}{u_v}\left(u_v^2 {k^c}_{us} + l\right) \tag{3.28}$$

Form Equation (3.28), it can be concluded that if ${k^c}_{us}$ becomes negative and speed exceeds the critical value, the mode of instability is jackknife. For snaking mode investigation, the Hurwitz determinants cannot be evaluated conveniently due to the multiplication of the coefficients. Therefore, an alternative numerical solution is proposed according to the damping ratio of the system ζ [9, 30]. In this method, a negative damping ratio shows that the system is unstable in snaking mode and a complex conjugate pair of eigenvalues is on the positive side of the real axis. The damping ratio is expressed as

$$\zeta = \frac{-\sigma}{\sqrt{\sigma^2 + \omega^2}} \tag{3.29}$$

where $s_{1,2} = \sigma \pm j\omega$ is a complex conjugate pair of eigenvalues. Table 3.2 summarizes how the instability modes are characterized. It is concluded that when the under-steer coefficient of the vehicle unit is negative (positive) the vehicle-trailer system is more prone to jackknife (snaking).

Table 3.2: Characterization of the instability modes

Jackknife instability	**Snaking instability**
${k^c}_{us} < 0$	${k^c}_{us} > 0$
$u_v > u^c_v$	$\zeta < 0$

3.3.1 A Trailer as a Pendulum

As pointed out, the linear stability analysis of a vehicle-trailer system shows that two different yaw instability modes can be characterized, jackknifing also known as saddle-node bifurcation, and snaking also called Hopf bifurcation. Most studies mainly considered a vehicle-trailer system as a single-dynamic system. However, knowing how a trailer is affected by a vehicle unit is more useful in understanding the proposed controller design strategy than considering the vehicle as a whole dynamic system. Assuming a trailer as a planar rigid body pinned to a point that moves forward with a constant longitudinal speed

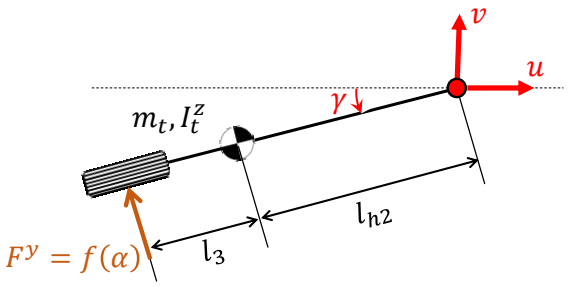

Figure 3.6: Trailer pendulum model.

u, it can be simply modeled as a pendulum (Fig. 3.6) [24], which is excited by a vehicle unit with an equivalent lateral velocity, v, at the hitch point.

With small hitch angle and linear tire model ($F^y = C_\alpha \alpha$) assumptions, the equation of motion for this model is as follows

$$\begin{aligned} I_t^z \ddot{\gamma} &= -C_\alpha \alpha (l_3 + l_{h2}) + l_{h2} m_t \dot{v} \\ I^z &= I_t^z + m_t l_{h2}^2 \end{aligned} \tag{3.30}$$

The lateral slip angle of the trailer axle is expressed as

$$\alpha = \gamma + \frac{(l_3 + l_{h2})\dot{\gamma} - v}{u} \tag{3.31}$$

Substituting Equation (3.31) into Equation (3.30) and then taking Laplace transform of the resulting, the transfer function of this system is described by Equation (3.32).

$$\frac{\Gamma(s)}{V(s)} = \frac{\frac{m_t l_{h2}}{I^z} s + \frac{C_\alpha (l_3 + l_{h2})}{u I^z}}{s^2 + \frac{C_\alpha (l_3 + l_{h2})^2}{u I^z} s + \frac{C_\alpha (l_3 + l_{h2})}{I^z}} \tag{3.32}$$

where C_α, $\Gamma(s)$, and $V(s)$ are the cornering stiffness of the tire, Laplace transform of γ and v, respectively.

Based on the Routh–Hurwitz stability criterion, this transfer function is BIBO stable, which means as long as the equivalent lateral velocity from the vehicle is bounded, the hitch angle remains bounded. It can be concluded that if the vehicle is kept in the stable region, the vehicle-trailer system will be stable. This conclusion is used for deciphering the phase portraits of the vehicle-trailer system in the following section, and chiefly for the controller design.

3.3.2 Phase Plane Analysis of Vehicle-Trailer System

As mentioned, for single-vehicles, a two-dimensional stable region can be found using phase plane analysis of a vehicle lateral dynamic model that considers the non-linear behavior of tires. To do so, phase portraits of the lateral dynamic for different fixed input values, which are usually steering angles and longitudinal velocity, are plotted, and the type and the movement of the equilibrium point are examined, assuming all other model parameters, like road friction, are constant. These portraits graphically depict state trajectories that give an insight into how to utilize active control systems to manipulate vehicle dynamic responses and to prevent instability.

The same procedure can also be conducted for vehicle-trailer systems; however, there are two main challenges. First, the lateral dynamics of this type of vehicle has four state variables, $x = [\beta_v \quad r_v \quad \dot{\gamma} \quad \gamma]^T$, which cannot be plotted in a three-dimensional phase portrait. To solve this, in the this thesis, the phase portraits are plotted for three degrees of freedom (i.e., β_v, r_v, and γ), while $\dot{\gamma}$ is set to zero for the initial conditions; afterward, the effect of $\dot{\gamma}$ is generally investigated for a better perception of the dynamic behavior of the vehicle-trailer system. Secondly, unlike in a single-vehicle, which mostly has a constant mass and yaw inertia, a specific vehicle unit may tow different trailers with different loading conditions. This can make a vehicle-trailer system vulnerable to both aforementioned yaw instability modes (snaking and jackknifing). Hence, after analyzing the trailer without a payload, it is studied under two different loading conditions that are expected to excite jackknifing and snaking modes. For the phase plane analysis, the non-linear model derived in Section 3.2 is used, however, the control actions are neglected ($V = 0_{3\times1}$) and the steering angle of the front axle is the only input of the model. Table 3.3 lists the parameters of the non-linear vehicle-trailer model derived in Section 3.2.

Table 3.3: Corresponding values for nonlinear-vehicle parameters.

Parameter	**Value**	**Parameter**	**Value**
m_v $[kg]$	2270	m_t $[kg]$	601
I_v^z $[kg.m^2]$	4605	I_t^z $[kg.m^2]$	1894
l_1 $[m]$	1.42	l_3 $[m]$	0.77
l_2 $[m]$	1.44	l_{h2} $[m]$	2.23
l_{h1} $[m]$	2.58		

Unloaded trailer and the steering effect: Steering angle is the main contributing factor in shaping the phase portraits rather than road friction and longitudinal velocity [99].

Table 3.4: Maximum absolute values and grid sizes of initial condition vector component.

Component	**Max.Abs. Value**	**Grid Value**
$\beta\,[deg]$	30	30
$r\,[deg/s]$	40	20
$\gamma\,[deg]$	30	30

To this end, the first set of phase portraits is plotted based on the steering angle input δ, which takes constant values of 0, 7, and 9 deg. Also, the longitudinal velocity of the vehicle u_v^x and the road friction μ are set to 40 kph and 0.8, respectively. The maximum absolute value of each axis and its grid size are defined in a reasonable range for clarity by reducing the number of trajectories, as presented in Table 3.4. For further clarification, the initial condition of stable and unstable trajectories, and stable equilibrium points are plotted with blue circles, red circles, and a red filled diamond markers, respectively. In addition, since the direction of the trajectories might not be visually discernible in three-dimensional portraits, stable trajectories are shown by blue solid lines and when a trajectory exceeds the borders/limits defined in Table 3.4, the simulation is stopped and also the trajectories are colored and styled differently. In detail, if a trajectory goes beyond the sideslip angle, yaw rate, and hitch angle boundaries, it is shown by a red thick solid line, red dashed line, and red line with plus sign markers, respectively.

From Figure 3.7, and Figure 3.8, as with a single-vehicle [96] a favorable region called stable region (containing the blue trajectories) and an unfavorable region called unstable region (containing the red trajectories) can still be distinguished around the equilibrium point. In the stable region, the vehicle tires have enough lateral force to maintain the asymptotically stable equilibrium and the vehicle's behavior can be reasonably predicted by the driver. However, in the unstable region, the vehicle cannot be controlled due to tire saturation and shows large sideslip angles in which the vehicle skids sideways and/or large yaw rates in which the vehicle spins out. These figures also show the movement of the asymptotically stable equilibrium point and the trajectories for different steering angles. The stable equilibrium of the vehicle-trailer system moves toward larger positive yaw rates and negative hitch angles as the steering angle is increased (blue stars in Figure 3.9). At a 9 degree steering angle input (see Figure 3.9), when the vehicle enters the unstable region, all three state variables continually grow and most of them follow a tail-like stem. All three state trajectories then continually grow in a specific direction. Regardless of those trajectories that follow the stem, other trajectories (the trajectories starting from points A, B, C, and D) quickly grow in the hitch angle direction compared to the other directions.

These trajectories appear if the initial conditions include extremely large sideslip angles or yaw rates.

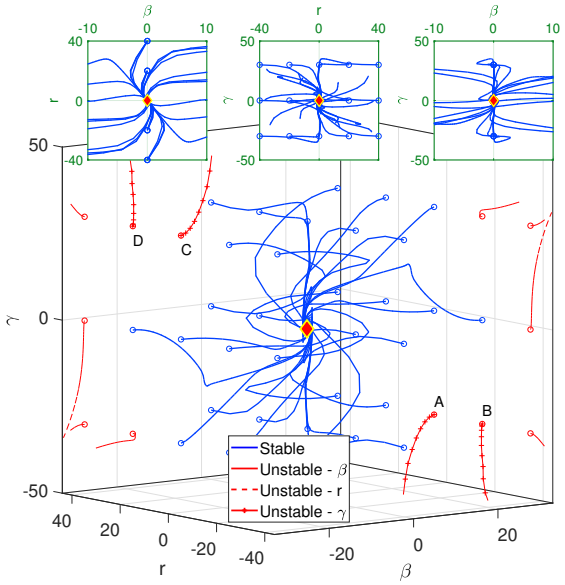

Figure 3.7: Phase portraits for unloaded trailer, $\delta = 0$ deg

Payload ***Steering effect for jackknifing and snaking:*** The loading condition of a trailer may significantly affect the dynamic behavior of its vehicle-trailer system. Thus, in this subsection, two different loading conditions are examined, one of which excites snaking and the other jackknifing. More specifically, a payload is located on the trailer with a distance of 1 and 3 meters from the hitch point, on the longitudinal axis, to initiate jackknifing and snaking, respectively. The mass of the payload and its yaw inertia are 500 kg and 500 $kg.m^2$, respectively.

Basically, putting a payload close to the hitch point enhances over-steer tendencies and makes a vehicle prone to jackknifing (saddle-node bifurcation) in which the hitch angle increases divergently without oscillation. While, in snaking instability (Hopf bifurcation), the hitch angle of a vehicle-trailer system shows oscillatory behavior.

Figure 3.10, and Figure 3.11 show the vehicle-trailer system when it is vulnerable to jackknifing for a 5 and 7 degree of steering angle input. The results demonstrate that adding the payload makes the vehicle less stable as it becomes unstable at a 7 degree of steering angle input, unlike with the unloaded trailer. From Fig. 3.10, it can also be seen

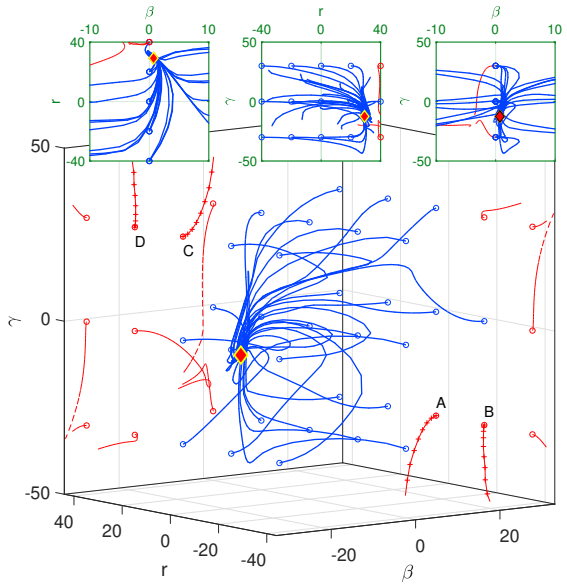

Figure 3.8: Phase portraits for unloaded trailer, $\delta = 7$ deg

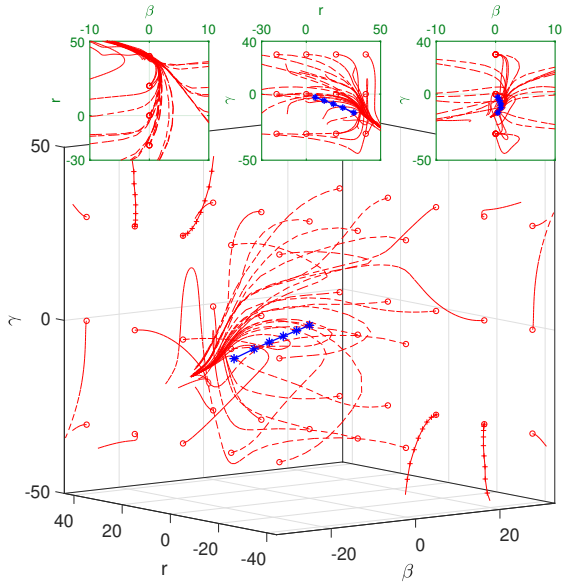

Figure 3.9: Phase portraits for unloaded trailer, $\delta = 9$ deg

that the trajectories do not show oscillatory behavior near the equilibrium point compared to the unloaded trailer, a finding compatible with jackknifing as described. Even though the overall instability form of the vehicle-trailer system is similar to that of the unloaded trailer, the former exhibits faster growth in its yaw rate due to higher over-steer tendencies, Fig. 3.11.

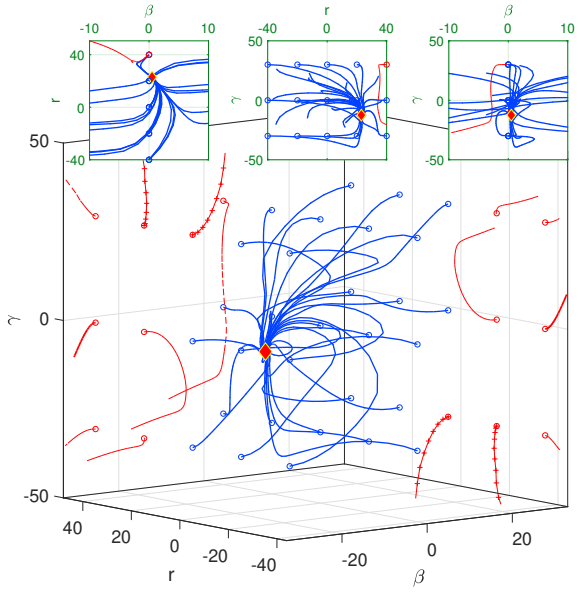

Figure 3.10: Phase portraits when vehicle-trailer is vulnerable to jackknifing, $\delta = 5$ deg

Figure 3.12 demonstrates the trajectories of the vehicle-trailer system when it is prone to snaking instability. Figure 3.14, a magnified form of Figure 3.13 in the $\beta - r$ plane, confirms a severe oscillatory behavior as a sign of snaking vulnerability and Hopf bifurcation. This behavior in a single-vehicle indicates under-steering and stability [96]. However, this is not valid for a vehicle-trailer system because this asymptotically stable equilibrium point may turn into an unstable one, if the steering angle exceeds a certain value and subsequently, the vehicle becomes unstable, as illustrated in this figure. When 7 deg of the steering angle input is applied, from Figures 3.13 and 3.14, it is noticeable that some trajectories that converge to the asymptotically stable equilibrium point at 5 deg of steering angle input (green trajectories) are unstable now. They move toward the stable equilibrium but enters the unstable region with a growing sideslip angle and yaw rate. It can be shown that this behavior fundamentally comes from the effect of $\dot{\gamma}$.

As an example, Figure 3.16 compares state variables of two different trajectories initi-

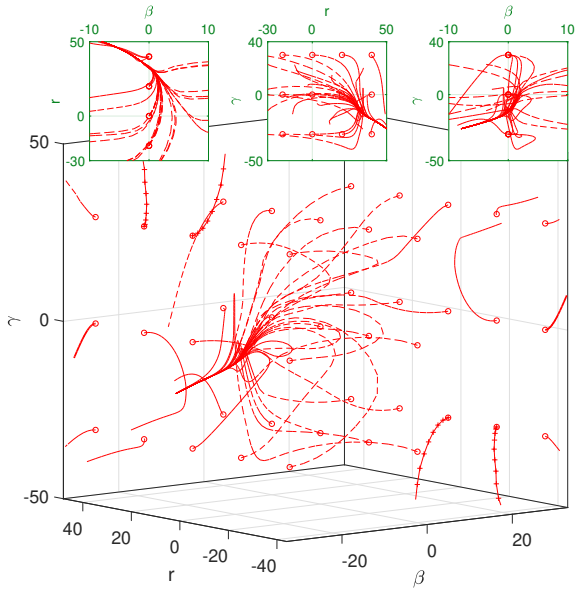

Figure 3.11: Phase portraits when vehicle-trailer is vulnerable to jackknifing, $\delta = 7$ deg

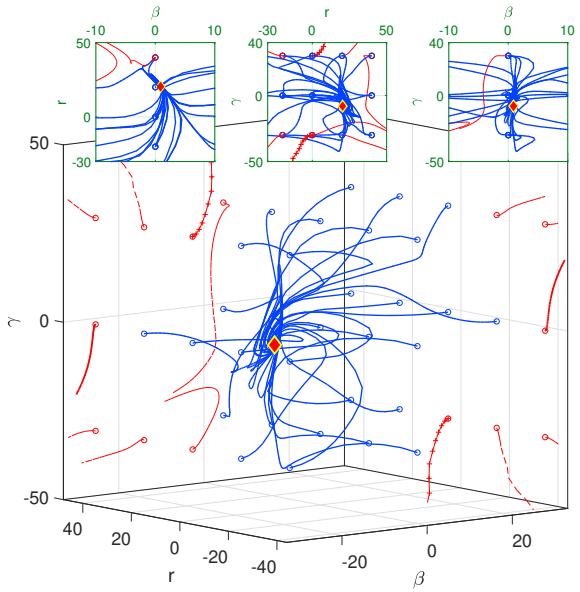

Figure 3.12: Phase portraits when vehicle-trailer is vulnerable to snaking, $\delta = 5$ deg

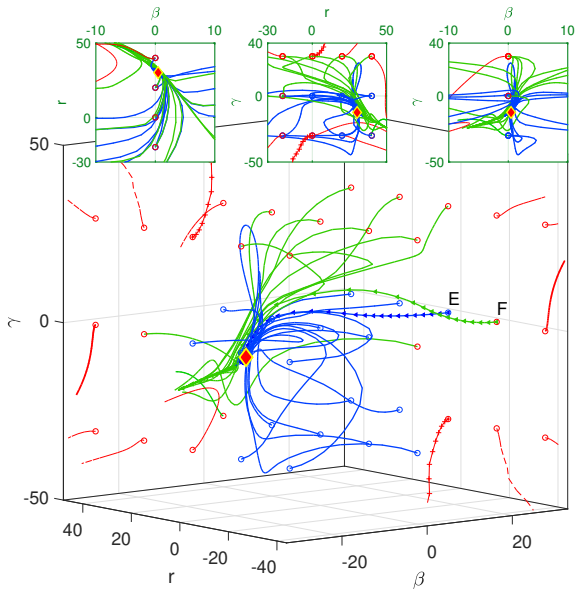

Figure 3.13: Phase portraits when vehicle-trailer is vulnerable to snaking, $\delta = 7$ deg

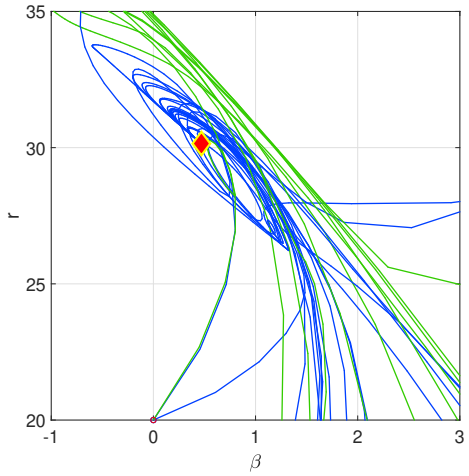

Figure 3.14: Phase portraits when vehicle-trailer is vulnerable to snaking, $\delta = 7$ deg-magnified

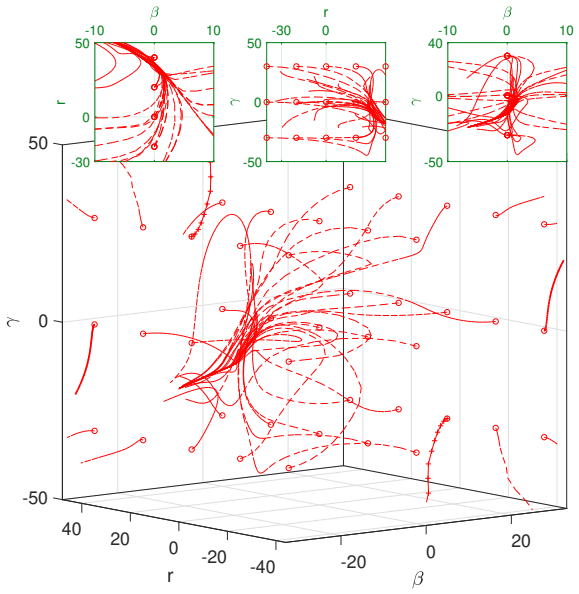

Figure 3.15: Phase portraits when vehicle-trailer is vulnerable to snaking, $\delta = 7.5$ deg

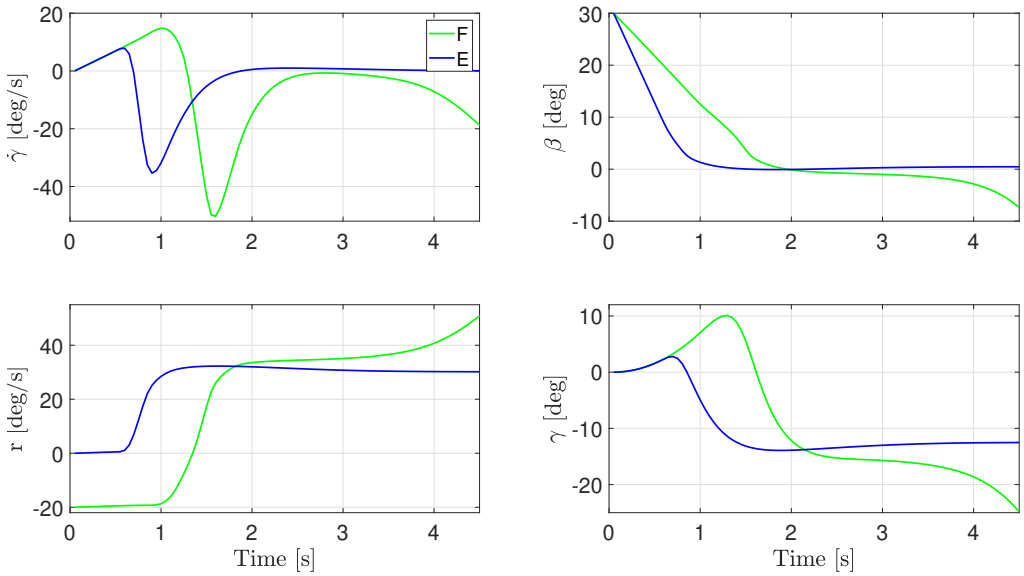

Figure 3.16: Trajectory comparison.

ated from two different initial conditions, introduced in Fig. 3.13 as point E (trajectory E) and F (trajectory F). These two points have the same hitch angle and sideslip angle; point F has a greater yaw rate than point E. This figure shows that the hitch angle rate of trajectory F goes up to an absolute value of 50 deg/s after 1.5 seconds when it is approaching the equilibrium point. Then, this extreme hitch angle rate is reduced significantly after about 0.5 second but since the yaw rate of the vehicle increases drastically up to 35 deg/s, the vehicle is not able to return toward the stable equilibrium point and finally becomes unstable. From this comparison, it is perceived that this extreme hitch angle rate is able to repel the trajectory from the stable equilibrium point and make the vehicle unstable when the vehicle is close to the stability margin. However, this only happens if the vehicle enters a region in which its yaw rate and sideslip angle continually grow (see lower left and upper right figures). Also, it should be noted that in the steady-state (e.g. $\dot{x} = 0$) hitch angle rate is zero which means if the vehicle remains stable hitch angle rate finally converges to zero.

Generally, the phase plane analysis provided in this section reveals that if the trajectories enter a certain area in the $\beta - r$ plane, they show persistent progress in yaw rate and sideslip angle and/or show quick growth in hitch angle for those started from large sideslip and yaw rates. This indicates that the stability boundary of a vehicle-trailer system essentially depends on the vehicle state variables. In other words, when the vehicle is kept in the stable region, a vehicle-trailer system remains stable as it was predicted by the linear analysis presented in Section 3.3.1.

Stability envelope for the vehicle-trailer system: The phase portraits presented in the previous section demonstrate that the state trajectories for different loading conditions enter the unstable region when the yaw rate and sideslip angle of the vehicle grow significantly when the steering angle exceeds a certain limit. Although it is observed that some trajectories quickly go up in the hitch angle direction, those are initialized from high sideslip angles and yaw rates. As a result, it is concluded that appropriately bounding the sideslip angle and yaw rate, without considering hitch angle and its rate, allows the active safety system to prevent the vehicle from entering the unstable region. Thus, the main objective of this section is to define an enclosed stable region called stability envelope by the state variables of the vehicle, the sideslip angle and yaw rate. Inside the defined envelope, there should exist an asymptotically stable equilibrium point to which the vehicle state trajectory converges. Stability control systems are expected to prevent the vehicle from leaving this stability envelope and also bring it back inside in case of any disturbance. Needless to say, a large hitch angle is not a stability concern and the hitch angle rate is implicitly controlled by keeping the vehicle inside the envelope because it finally converges to zero at the stable equilibrium point.

When the vehicle is stable, state trajectories converge to the asymptotically stable equilibrium point which is the steady-state of the vehicle response. Therefore, to define the stability envelope, first, the maximum steady-state yaw rate needs to be found. In this regard, the vehicle equations of motion at the steady-state, $\dot{\beta}_v = 0$, $\dot{r}_v = 0$, $\ddot{\gamma} = 0$, and $\dot{\gamma} = 0$, are obtained by eliminating the hitch point forces in (3.5) and (3.6) using (3.7) to (3.10). The final equations are expressed as

$$0 = l_{h1} m_t u_v^x \left(\frac{l_3 + l_{h2} sin^2 \gamma^{ss}}{l_3 + l_{h2}} \right) r_v^{ss} + l_1 F_1^y - l_2 F_2^y \tag{3.33}$$

$$\begin{aligned} 0 = &- \left(m_v + m_t \frac{l_3 + l_{h2} sin^2 \gamma^{ss}}{l_3 + l_{h2}} \right) u_v^x r_v^{ss} + F_1^y \\ &+ F_2^y \end{aligned} \tag{3.34}$$

where r_v^{ss} and γ^{ss} are the steady-state yaw rate and hitch angle, respectively. Using these two equations, the steady-state yaw rate can be define as a function of first and second axle lateral force as follows

$$r_v^{ss} = \left(\frac{l_1 + l_2}{u_v^x \left(l_2 m_v + m_t (l_2 - l_{h1}) Z \right)} \right) F_1^y \tag{3.35}$$

$$r_v^{ss} = \left(\frac{l_1 + l_2}{u_v^x \left(l_1 m_v + m_t (l_1 + l_{h1}) Z \right)} \right) F_2^y \tag{3.36}$$

$$Z = \left(\frac{l_3 + l_{h2} sin^2 (\gamma^{ss})}{l_3 + l_{h2}} \right)$$

As mentioned, based on the loading condition of the vehicle, one of the vehicle axles reaches its maximum capacity first. Besides, the maximum yaw rate of the vehicle is basically limited by the maximum available lateral force of the axles [3, 115]. Thus, two different maximum yaw rate can be obtained as expressed in (3.37) and (3.38).

$$r_v^{max1} = \left(\frac{l_1 + l_2}{u_v^x \left(l_2 m_v + m_t (l_2 - l_{h1}) Z \right)} \right) F_1^{y.max} \tag{3.37}$$

$$r_v^{max2} = \left(\frac{l_1 + l_2}{u_v^x \left(l_1 m_v + m_t (l_1 + l_{h1}) Z \right)} \right) F_2^{y.max} \tag{3.38}$$

$$Z = \left(\frac{l_3 + l_{h2} sin^2(\gamma^{ss.max})}{l_3 + l_{h2}} \right)$$

where $F_1^{y.max}$ and $F_2^{y.max}$ are the maximum lateral force of the first axle and the second axle, respectively, and $\gamma^{ss.max}$ is the maximum steady-state hitch angle while the vehicle remains stable. $\gamma^{ss.max}$ is approximately defined using Equation (3.31) by replacing the lateral velocity of the hitch point v with its maximum value while the vehicle remains stable v^{max}. $\gamma^{ss.max}$ and v^{max} are expressed as follows

$$v^{max} \approx \frac{l_{h1}}{l_2} u_v^x \alpha_2^{sat} \tag{3.39}$$

$$\gamma^{ss.max} \approx \frac{l_{h1}}{l_2} \alpha_2^{sat} + \alpha_3^{sat} \tag{3.40}$$

Based on different loading conditions of the trailer, each of these lateral forces may saturate first. In this regard, the yaw rate boundary of the stability envelope is defined as the minimum of these two yaw rates, as presented in Equation (3.41), to make sure that the tire saturation of the vehicle is prevented.

$$r_v^{max} = min\left(r_v^{max1}, r_v^{max2}\right) \tag{3.41}$$

As described, some initial conditions with high sideslip angles, no matter what the value of yaw rate is, cause unstable trajectories. Therefore, this state variable should also be restricted for keeping the vehicle stable. As Beal et al. described in [116] for a single-vehicle, the slip angle at the second axle as a linear combination of yaw rate and sideslip angle, expressed in Equation (3.15), can be bounded rather than the sideslip angle. The main reason is that at low speeds where the vehicle may reach large sideslip angles, without losing stability, the slip angle of the rear axle remains small. Here, the same approach is utilized for bounding the sideslip angle of the vehicle. Applying these bounds results in a stable region inside a parallelogram as illustrated in Fig. 3.17.

Two-dimensional phase portraits are once again plotted at the maximum allowable steering angle while the vehicle remains stable to make sure that the defined stability envelope satisfies all the discussed loading conditions.To maintain the vehicle stable, the controller needs to keep the vehicle inside the stable region or bring it back if it is outside. To prevent undamped or unstable behavior, there should be an asymptotically stable equilibrium point inside the boundary of the stability envelope (stable region) for all of

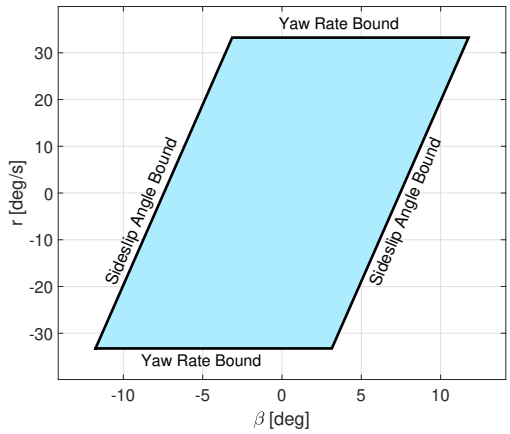

Figure 3.17: 2D stability envelope.

the mentioned situations. By this strategy, it is theoretically guaranteed that the vehicle state trajectory converges to that stable equilibrium point (i.e., the vehicle stays stable) if active control systems are able to prevent the vehicle from entering the unstable region. Figure 3.18 confirms that the defined stability envelope accurately encloses a region with a stable equilibrium point inside for all the loading conditions so that there is no stable equilibrium point beyond its boundaries when δ is slightly increased. It should be noted that the bounds change in each of these situations due to the different loading conditions as stated in Equations (3.37) and (3.38). In all of these figures, γ and $\dot{\gamma}$ are set equal to zero in all initial conditions.

3.4 Summary

In this chapter, first, a non-linear vehicle-trailer bicycle model was developed using a brush tire model to comprehensively examine their non-linear behavior. The brush tire model was linearized at each time step at its operating point to convert the non-linear vehicle model to an affine model. This model is utilized as the prediction model in the MPC controller developed in Chapter 4.

The stability of a vehicle-trailer system was analyzed using a linear model derived based on the affine model. This linear analysis characterized the instability modes of vehicle-trailer systems. To solely understand the dynamic behavior of a trailer excited by a vehicle unit, the trailer was also modeled as a pendulum. This study showed that a

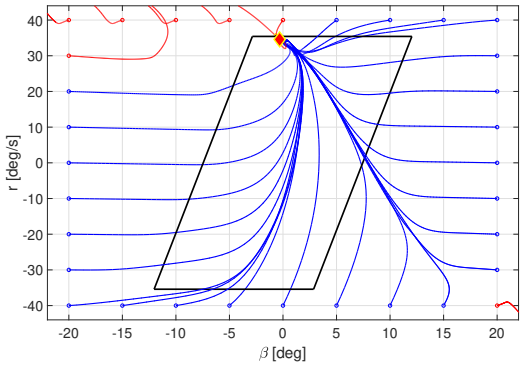

(a) Unloaded, $\delta = 7.7$ deg

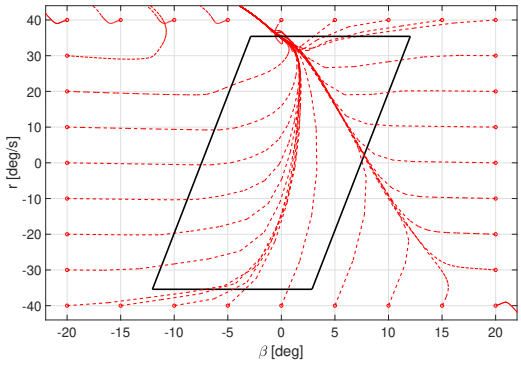

(b) Unloaded, $\delta = 7.8$

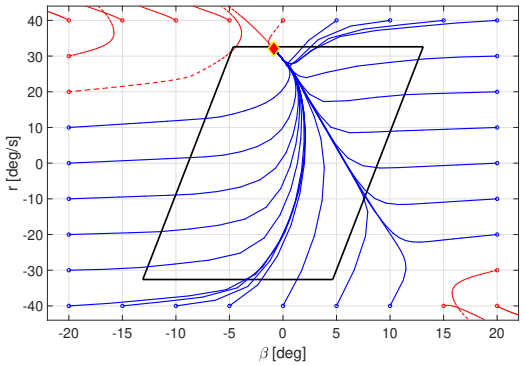

(c) Jackknifing, $\delta = 6.1$ deg

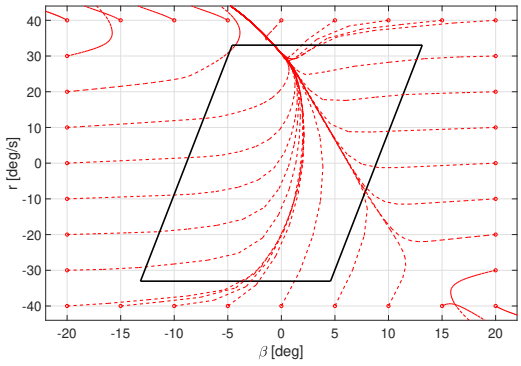

(d) Jackknifing, $\delta = 6.2$ deg

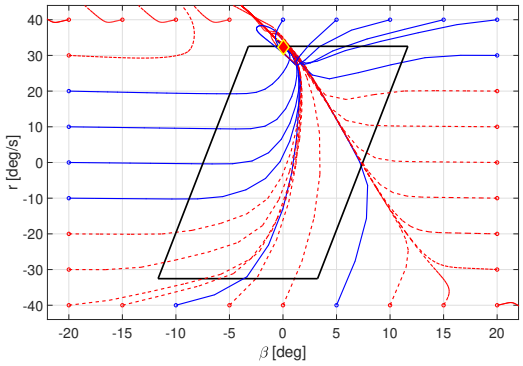

(e) Snaking, $\delta = 7.2$ deg

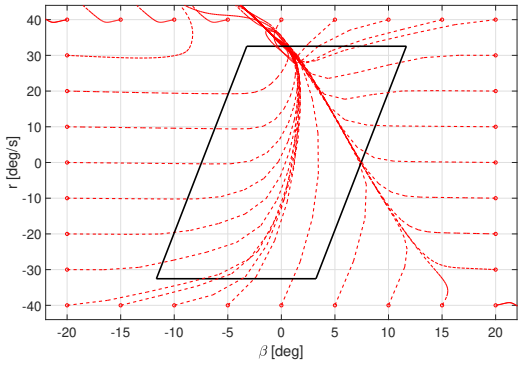

(f) Snaking, $\delta = 7.3$ deg

Figure 3.18: Equilibrium point at the stability margin

trailer remains stable if the equivalent lateral velocity at the hitch point generated by the vehicle is bounded. This is a conclusion that was leveraged to explain the phase portraits of the vehicle.

Using the derived non-linear vehicle-trailer system model, the phase portraits of the lateral dynamic for different steering inputs were depicted in a three-dimensional space using the sideslip angle and the yaw rate of the vehicle and hitch angle. This process was repeated for two different loading conditions by which the vehicle was made vulnerable to snaking and jackknifing. Those plots showed that two clearly-separated sub-spaces can be found in that 3D space, a stable region and an unstable one. It was also observed that as the steering angle increases, the asymptotically stable equilibrium point moves toward higher yaw rates, and at a specific steering angle that equilibrium point disappears and the trajectories grow continually, i.e., the vehicle becomes unstable. To find an enclosed area that always contains an asymptotically stable equilibrium point that the trajectories can converge to, the equations of motion at the equilibrium point were obtained which led to a parallelogram-shape stable area in the $\beta - r$ plane called stability envelope.

Chapter 4

Development of a Reconfigurable Vehicle-Trailer Control System

In this chapter, a reconfigurable control structure is developed that considers both vehicle and trailer dynamics. This controller is expected to keep the vehicle inside the stability envelope defined in Chapter 3, with minimum intervention, in wide loading and longitudinal velocity ranges. To make the controller applicable to any vehicle and trailer, it will be reconfigurable for any combination of actuation system in the vehicle and trailer. To this aim, a two-layer hierarchical control structure is developed. The upper layer is an MPC controller that utilizes the affine bicycle model developed in Chapter 3 to predict the future vehicle state variables. Having this prediction model and the reference values, a quadratic performance index is formed based on the weighted tracking error and three penalized virtual control actions that are devoted to the three degrees of freedom. Then, the optimal solution of this index is obtained according to the control action and state constraints. Finally, the optimized solution is distributed among the available actuators by the lower layer, which uses an optimization process called Control Allocation (CA) technique at each time step (see Figure 4.1). This low-level module, the major component in the proposed control structure, is able to constraint combined longitudinal and lateral forces so as not to exceed the friction circle limit, in addition to the actuators' capacity.

4.1 Upper Layer, Model Predictive Control

As explained, the designed controller is expected to avoid the undesirable dynamic behaviors of the vehicle-trailer system. In all cases, the vehicle needs to remain stable, especially

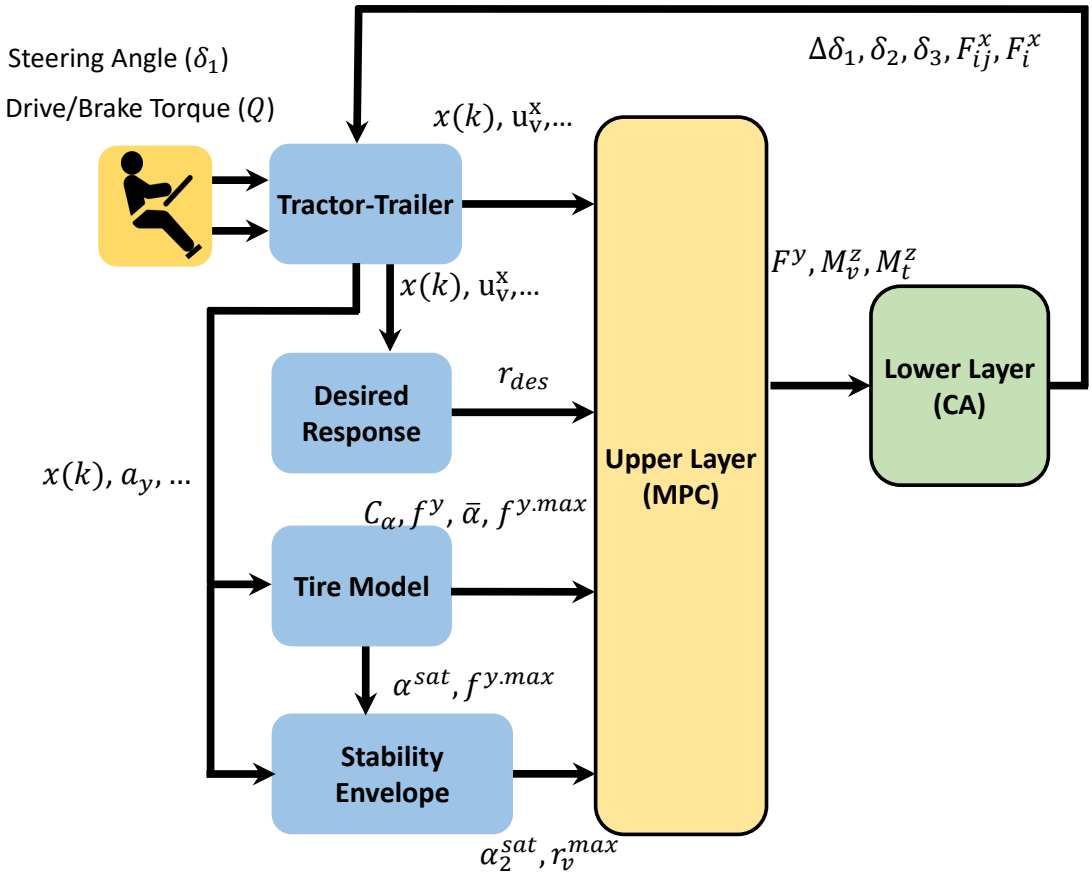

Figure 4.1: The structure of the proposed controller

in high lateral acceleration maneuvers in which the tires are in the non-linear region. Thus, the intended controller should be capable of covering the aforementioned non-linearity as well as bounding state variables. A model predictive controller provides some capabilities by which the requirements of interest are met [4, 69, 115, 117, 107]. First, an MPC is able to predict the dynamic behavior of the system and it can also be extended to affine models in which the non-linearity of tires can be considered. Furthermore, it has the capability of applying constraints to both inputs and outputs in addition to the quadratic performance index. These constraints are able to prevent the vehicle from losing controllability and stability due to tire saturation. According to the above-mentioned advantages, in this thesis, MPC will be used as the control method. The general control scheme of the MPC

is illustrated in Figure 4.2. In this technique, first, a discretized model is made from the continuous model to formulate a prediction model. Then, at each time step, the behavior of the system is predicted for a finite prediction time, known as the prediction horizon, using the current state of the system and the prediction model. With the knowledge of the desired future outputs, a certain number of control actions, known as the control horizon, for this finite horizon are obtained such that the objective performance index becomes minimized. Only the first control action (or the first set of control actions when there is more than one input) is applied and all other inputs are discarded. This concept, identified as a receding horizon, is a key feature of the MPC approach. Obtaining a new set of state variables at the next time step, the whole process is repeated, and a new control action is determined. The aforementioned procedure including the desired response, constraints, prediction model derivation, and the performance index definition, are described in the following sections.

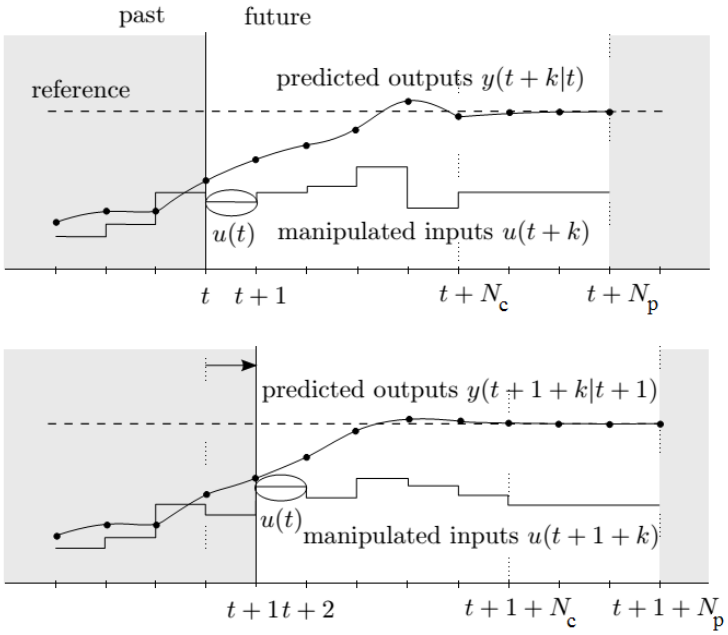

Figure 4.2: Illustration of model predictive control (MPC) concept [118]

4.1.1 Desired Response

For the stability control of the vehicle-trailer system, the desired yaw rate of the vehicle, r_{des}, is needed. The controller uses this desired value to correct the behavior of the vehicle. In this controller, the driver's intent is inferred by the final yaw rate of the developed affine model, r^*, without a trailer, with respect to the applied steering angle over the prediction horizon. It is assumed that the steering angle remains constant over the prediction horizon and the control action is zero. This response is exploited as the desired output rather than the steady-state value of a linear bicycle model. Hence, the controller does not force the vehicle to follow a linear dynamic response that does not match with the real dynamic behavior, especially at the handling limit.Thus there is less controller intervention, and the driver is provided with the same vehicle response that would occur if a trailer was not attached. To prevent instability, this desired yaw rate is limited by the yaw rate of the stability envelope as follows:

$$r_{des} = sign(r^*)min(|r^*|, |r_v^{max}|) \tag{4.1}$$

4.1.2 Constraints

As pointed out, constraints are one of the most important features of MPC controllers. These constraints are applied in the MPC controller in the form of upper and lower bounds. In fact, the maximum capacity of each control action provided by the controller is constrained as well as its rate based on the remaining capacity of tires and the capability of the actuator. These two sets of constraint are stated in Equations (4.2) and (4.3).

$$V^{min}(k) \leq V(k) \leq V^{max}(k) \tag{4.2}$$

$$|\Delta V(k)| \leq \Delta V^{max} \tag{4.3}$$

where k is the k^{th} prediction time, V^{min} and V^{max} are the minimum and the maximum compensatory control action, respectively. Also, ΔV^{max} is the maximum compensatory control action rate that can be defined based on the actuator capacity.

V^{min} and V^{max} are fundamentally limited based on the remaining capacity of the tires. For each tire, the available lateral force, $F^{y.max}$, and longitudinal force, $F^{x.max}$,can be defined using the friction circle as follows

$$F^{x.max} = \sqrt{(\mu F^z)^2 - (f^y(\bar{\alpha}))^2} \tag{4.4}$$

$$F^{y.max} = \sqrt{(\mu F^z)^2 - (F^{x.cur})^2} \tag{4.5}$$

In the above equations, the current lateral force $f^y(\bar{\alpha})$ is obtained using the Tire Model block shown in Figure 4.3 which exploits the brush tire model as explained. If the braking torque applied by the driver on each wheel, the longitudinal force applied by the controller, and the effective radius of the tire are denoted by q, $F^{x.c}$, and r_{eff}, respectively, the current longitudinal force $F^{x.cur}$ can be expressed as

$$F^{x.cur} = \frac{q}{r_{eff}} + F^{x.c} \tag{4.6}$$

Having $F^{y.max}$ and $F^{x.max}$ for each tire, the components of the upper bound vector $V^{max} = [F_v^{y.max} \quad M_v^{z.max} \quad M_t^{z.max}]^T$ and the components of the lower bound vector $V^{min} = [F_v^{y.min} \quad M_v^{z.min} \quad M_t^{z.min}]^T$ are obtained as

$$F_v^{y.max} = F_{fl}^{y.max} + F_{fr}^{y.max} + F_{rl}^{y.max} + F_{rr}^{y.max} \tag{4.7}$$

$$F_v^{y.min} = -F_v^{y.max} \tag{4.8}$$

$$M_v^{z.max} = \frac{\left(F_{fl}^{x.max} + F_{rl}^{x.max}\right) T_v}{2} \tag{4.9}$$

$$M_v^{z.min} = \frac{\left(F_{fr}^{x.max} + F_{rr}^{x.max}\right) T_v}{2} \tag{4.10}$$

$$M_t^{z.max} = \frac{F_l^{x.max} T_t}{2} \tag{4.11}$$

$$M_t^{z.min} = \frac{F_r^{x.max} T_t}{2} \tag{4.12}$$

where subscripts fl, fr, rl, rr, l, and r denote front left, front right, rear left, and rear right wheels of the vehicle and left and right wheels of the trailer, respectively.

In addition, the stability envelope is applied through the state constraints to prevent the vehicle from leaving the envelope due to disturbance or model uncertainties and expressed as follows

$$\begin{aligned} &\mathbf{C_{env}}\,|x(k)| \leq x_{env} + \xi \\ &\mathbf{C_{env}} = \begin{bmatrix} -1 & \frac{l_2}{u_v^x} & 0 & 0 \\ 0 & 1 & 0 & 0 \end{bmatrix}, x_{env} = \begin{bmatrix} \alpha_2^{sat} \\ r_v^{max} \end{bmatrix} \end{aligned} \tag{4.13}$$

In the above equation, ξ is a non-negative slack variable of the k^{th} prediction time which is used to make the stability envelope a soft constraint. In the optimization formulation, this variable is also considered in the performance index and minimized regarding the assigned weight. This technique allows the optimization problem to find a solution even if the constraints are violated and try to bring back the vehicle inside the envelope.

4.1.3 Performance Index

In this section, the performance index is derived to express the MPC controller as an optimization problem. To this aim, first, a discrete model is needed for the prediction model. The discretization method utilized in this thesis is Zero Order Hold (ZOH) which is commonly used in the literature. In this method, the assumption is that the input of the system remains constant over the time step which is valid as the time step is not large. Having the discrete model, if the optimization goal is to minimize the error between the predicted outputs $y(k)$ and the desired outputs $y_d(k)$, then a quadratic cost function J_{MPC} can be formulated over a finite number of horizon h_p and a finite number of control action and its increment CH as follows:

$$\begin{aligned} \Delta V_{opt} \;=\; & \text{argmin}(J_{MPC}) = \text{argmin}\Bigg(\sum_{k=0}^{h_p-1} ||y_d(k) - y(k)||^2_{\mathbf{Q}} \\ & + \sum_{k=0}^{h_c-1} ||V(k)||^2_{\mathbf{S}} + \sum_{k=0}^{h_c-1} ||\Delta V(k)||^2_{\mathbf{R}} \\ & + ||\xi||^1_{\mathbf{E}} \Bigg) \\ & s.t. \\ & Constraints\, \forall k = 1, ..., h_p \end{aligned}$$

where the matrices $\mathbf{Q} \geq 0$, $\mathbf{R} > 0$, $\mathbf{S} > 0$, and $\mathbf{E} > 0$ are weighting matrices that reflect the relative importance of the tracking errors, the control actions and their rates, and the slack variables correspondingly.

The predicted outputs can be expressed in terms of the current state of the system at time k and the future control actions. For the affine bicycle model used in the stability control, the predicted future output is expressed as

$$Y(k) = \mathbf{\Psi} x(k) + \mathbf{\Gamma} V(k-1) + \mathbf{\Phi} \Delta \mathbb{V}(k) + \mathbf{\Lambda} w_d \tag{4.14}$$

Initial condition matrix $\mathbf{\Psi} \in \mathbb{R}^{pi \times 4}$, current control action matrix $\mathbf{\Gamma} \in \mathbb{R}^{pi \times 3}$, control action increment matrix $\mathbf{\Phi} \in \mathbb{R}^{pi \times 3j}$, affine matrix $\mathbf{\Lambda} \in \mathbb{R}^{pi \times 4}$, and control actions increment vector $\Delta \mathbb{V}(k) \in \mathbb{R}^{3j \times 1}$ are defined in Appendix A.2. In the defined matrices, i, j, and p, are the number of prediction horizon, control horizon, and affine model output size, respectively. In this case, $Y(k)$ is a vector containing the predicted outputs over the prediction horizon, $x(k)$ is the current system state (measured and/or estimated), and $V(k-1)$ is the last applied set of control actions. Now, the cost function is rewritten as

$$J_{MPC} = ||Y_d(k) - Y(k)||^2_{\bar{\mathbf{Q}}} + ||\Delta \mathbb{V}(k)||^2_{\bar{\mathbf{R}}} + ||\mathbb{V}(k)||^2_{\bar{\mathbf{S}}} + ||\xi||^1_{\mathbf{E}} \tag{4.15}$$

where $Y_d(k)$ and $\mathbb{V}(k)$ are vectors containing all the desired outputs and control actions over the prediction horizon, respectively, and $\bar{\mathbf{Q}}$, $\bar{\mathbf{R}}$ and $\bar{\mathbf{S}}$ are defined as follows

$$\bar{\mathbf{Q}} = \text{diag}(\mathbf{Q}), \quad \bar{\mathbf{R}} = \text{diag}(\mathbf{R}), \quad \bar{\mathbf{S}} = \text{diag}(\mathbf{S}) \tag{4.16}$$

Now let

$$\mathbb{S} = Y_d(k) - \mathbf{\Psi} x(k) - \mathbf{\Gamma} V(k-1) - \mathbf{\Lambda} w_d \tag{4.17}$$

Substituting $Y(k)$, and $Y_d(k)$ into Equation (4.15) using Equations (4.14) and (4.17), augmenting $\Delta \mathbb{V}(k)$ with slack variables ξ by creating a new vector $\Delta \mathbb{V}^*(k) = [V^T \quad \xi^T]^T$, and then expanding and rearranging, the final expression of the cost function is rewritten as

$$J_{MPC}(k) = \Delta \mathbb{V}^{*T} \mathbf{H}^* \Delta \mathbb{V}^* + \Delta \mathbb{V}^{*T} \mathbf{F}^* + \text{Constant} \tag{4.18}$$

where

$$\mathbf{H}^* = \text{diag}(\mathbf{H}, 0_{p \times p}), \quad \mathbf{H} = \mathbf{\Phi}^T \bar{\mathbf{Q}} \mathbf{\Phi} + \bar{\mathbf{R}} + \bar{\mathbf{S}} \tag{4.19}$$

$$\mathbf{F}^* = [\mathbf{F}^T \quad \mathbf{E}^T]^T, \quad \mathbf{F} = 2\left(\mathbf{\Phi}^T \bar{\mathbf{Q}} \mathbb{S} + \bar{\mathbf{S}} \begin{bmatrix} \mathbf{1}_{h_p \times 1} \end{bmatrix} V(k-1)\right) \tag{4.20}$$

and the remaining constants are lumped into Constant.

Having $\mathbf{H}^*$ and $\mathbf{F}^*$, the quadratic cost function (Equation 4.18) can be solved for the optimal control action increments with respect to the defined bounds as follows

$$\begin{aligned} &\Delta \mathbb{V}^*_{opt} = \text{argmin } J_{MPC} \\ &s.t. \\ &\quad V^{min}(k) \leq V(k) \leq V^{max}(k) \quad \forall k \\ &\quad |\Delta V(k)| \leq \Delta V^{max} \quad \forall k \\ &\quad \mathbf{C_{env}}\, |x(k)| \leq x_{env} + \xi \quad \forall k \end{aligned} \tag{4.21}$$

In this thesis, in both MATLAB/Simulink simulations and real-time implementations, qpOASES solver [119] solves Equation 4.21. After solving the cost function for the optimal increment of the control actions, the first set of result $\Delta V^*_{opt}(k)$ is added to the applied control actions in the previous time step $V(k-1)$, see Equation (4.22). Then, the result is fed to the distribution module for the optimal distribution among available actuators.

$$V(k) = V(k-1) + \Delta V^*_{opt}(k) \tag{4.22}$$

4.2 Lower Layer, Optimized Distribution

As discussed, in the proposed control structure, the virtual control actions provided by the upper layer MPC need to be distributed optimally between available/preferred actuators. This technique that is called control allocation is usually employed to cope with over actuated systems for safety, reliability, or even comfort purposes. In this thesis, the active safety systems that are considered to be the actuators are Vehicle Differential Braking (VDB), Trailer Differential Braking (TDB), Active Front Steering (AFS), Active Rear Steering (ARS), and Active Trailer Steering (ATS).

In VDB and TDB, the corrective longitudinal force of the each tire is considered to be the actual control action, e.g. ΔF^x_{fl}, ΔF^x_{fr}, ΔF^x_{rl}, ΔF^x_{rr}, ΔF^x_{l}, and ΔF^x_{r}. These corrective longitudinal forces are transformed to braking torques using Equation (4.6) and then applied to each wheel. Each steering angle, however, is obtained from the summation of the current lateral force of each axle (F^y_i) and the lateral force correction, ΔF^y_i calculated by the low-level distribution module. Then, this force is transformed to its corresponding lateral slip angle as the desired angle using the tire model introduced in Section 3.1. By using the desired lateral slip angle, the required steering angle is obtained using Equations (3.14)-(3.14) depending on the axle number.

The relationship between the virtual control actions and aforementioned actuators with small angle assumption can be written as

$$F^y = \Delta F_1^y + \Delta F_2^y \tag{4.23}$$

$$M_v^z = \Delta F_1^y l_1 - \Delta F_2^y l_2 + 0.5\left(\Delta F_{fr}^x + \Delta F_{rr}^x - \Delta F_{fl}^x - \Delta F_{rl}^x\right) T_v \tag{4.24}$$

$$M_t^z = -\Delta F_3^y l_3 + 0.5\left(\Delta F_r^x - \Delta F_l^x\right) T_t \tag{4.25}$$

The virtual control actions can be mapped to the actuator commands using the above equations thorough a mapping matrix, $\mathbf{A}_{vu}$, called control effective matrix as follows

$$V = \begin{bmatrix} F^y \\ M_v^z \\ M_t^z \end{bmatrix} = \mathbf{A}_{vu} U \tag{4.26}$$

where U is the actuator command vector that contains all considered active safety systems. U and $\mathbf{A}_{vu}$ are defined as

$$U = \begin{bmatrix} \Delta F_1^y & \Delta F_2^y & \Delta F_3^y & \Delta F_{fl}^x & \Delta F_{fr}^x & \Delta F_{rl}^x & \Delta F_{rr}^x & \Delta F_l^x & \Delta F_r^x \end{bmatrix}^T \tag{4.27}$$

$$\mathbf{A}_{vu} = \begin{bmatrix} 1 & 1 & 0 & 0 & 0 & 0 & 0 & 0 & 0 \\ l_1 & -l_2 & 0 & -0.5T_v & 0.5T_v & -0.5T_v & 0.5T_v & 0 & 0 \\ 0 & 0 & -l_3 & 0 & 0 & 0 & 0 & -0.5T_t & 0.5T_t \end{bmatrix} \tag{4.28}$$

As Equations (4.23)-(4.25) present, the lateral and longitudinal corrective forces are applied on each tire, simultaneously. Therefore, the friction circle limit needs to be considered to prevent any possible tire saturation. CA is generally is an optimization problem and has a convex quadratic formulation with linear constraint capability. As a low-level distribution method, this single step optimization process offers not only imposing lower and upper bound for each real control action but also considering the friction circle limit for each tire. The constraints regarding the friction circle limit are nonlinear but convex. Therefore, it should be linearized to be used as linear constraints in the CA formulation. To do so, this circle is approximated by an octagon inscribed in it as Figure 4.3 shows.

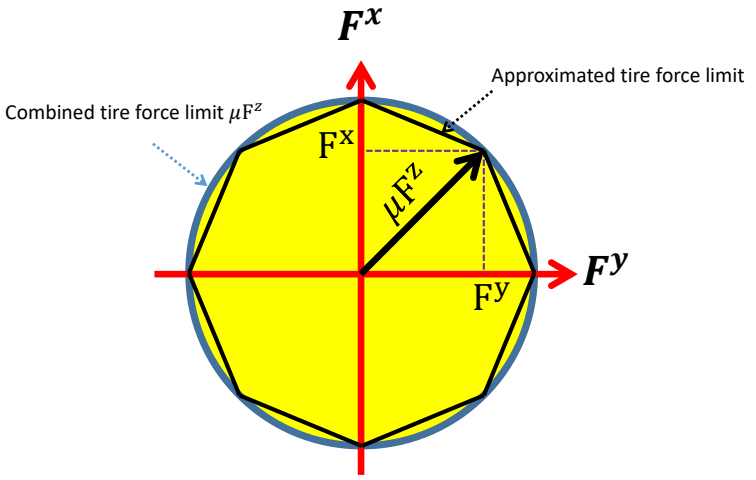

Figure 4.3: Approximated friction circle limit by an octagon

The actuators' limits with respect to their health and status can be considered by defining lower bound U^{min} and upper bound U^{max} on the actuator command vector. If these actuators are healthy, they are only bounded by the tire capacity using Equations (4.4) and (4.5), by which the available lateral and longitudinal forces at each time step is provided.

$$U^{max} = \begin{bmatrix} F_1^{y.max} & F_2^{y.max} & F_3^{y.max} & F_{fl}^{x.max} & F_{fr}^{x.max} & F_{rl}^{x.max} & F_{rr}^{x.max} & F_l^{x.max} & F_r^{x.max} \end{bmatrix}^T \tag{4.29}$$

where

$$\begin{aligned} F_1^{y.max} &= 2min(F_{fl}^{y.max}, F_{fr}^{y.max}) \\ F_2^{y.max} &= 2min(F_{rl}^{y.max}, F_{rr}^{y.max}) \\ F_3^{y.max} &= 2min(F_l^{y.max}, F_r^{y.max}) \end{aligned} \tag{4.30}$$

$$U^{min} = -U^{max} \tag{4.31}$$

Having the control effective matrix, the actuator capacity constraints, and the friction circle constraints, CA can be formulated. In the CA, the aim of the optimization is to map the virtual control actions to the actuator commands with respect to the defined weights and considering actuator and tire limitations as linear constraints as follows

$$\begin{aligned} U_{opt} \quad &= \quad \text{argmin}\Big(||V - \mathbf{A}_{vu}\mathbf{G}U||^2_{\mathbf{W}_{vu}} + ||U||^2_{\mathbf{W}_u}\Big) \\ &s.t. \\ & \qquad U^{min} \leq U \leq U^{max} \\ & \qquad linearized\sqrt{(F^x)^2 + (F^y)^2} \leq \mu F^z \end{aligned} \tag{4.32}$$

where the matrices $\mathbf{W}_{vu} > 0$ and $\mathbf{W}_u \geq 0$ are the weighting matrices that regulate the error between the virtual control actions and the actuator commands and penalize the effort of the actuator commands, respectively. $\mathbf{G} \geq 0$ is also a weighting matrix that can be utilized to define the relative importance of the actuators. This might also be useful for actuator prioritization in which the most effective actuator in a certain operating condition is mainly exploited.

4.3 Simulation and Experimental Results

In this section, to assess the performance of the proposed control structure and the effectiveness of the stability envelope developed in this chapter and Section 3.3, a comprehensive simulation/experiment-based study is conducted using different control actions and their integrations as follows

- Active front steering, AFS
- Active rear steering, ARS
- Active trailer steering, ATS
- Vehicle differential braking, VDB
- Trailer differential braking, TDB
- Integrated vehicle differential braking and active rear steering, VDB+ARS
- Integrated vehicle differential braking and trailer differential braking, VDB+TDB

Table 4.1: Corresponding values for the vehicle parameters used in simulations

Parameter	**Value**	**Parameter**	**Value**
m_v $[kg]$	2270	I_t^z $[kg.m^2]$	1080
I_v^z $[kg.m^2]$	4605	l_3 $[m]$	0.2
l_1 $[m]$	1.42	l_{h2} $[m]$	2.60
l_2 $[m]$	1.44	$C_{\alpha 1}$ $[N/rad]$	94748
l_{h1} $[m]$	2.58	$C_{\alpha 2}$ $[N/rad]$	103235
m_t $[kg]$	700	$C_{\alpha 3}$ $[N/rad]$	104160

4.3.1 Simulation Results

For the simulations, the controller is implemented in MATLAB and a high-fidelity and experimentally validated CarSim model [120] provided by General Motors car company is used to represent the vehicle dynamics. In this configuration, CarSim receives the steering angle δ_1^D and brake/drive torques T_b^D/T_v^D from driver and provides the feedback signals required for the controller module such as the vehicle longitudinal velocity u_v^x, sideslip angle β_v, longitudinal/lateral acceleration a_v^x/a_v^y, hitch angle γ and its rate $\dot{\gamma}$. The properties of the vehicle and the trailer used in simulations are presented in Table 4.1.

To excite the yaw instability modes, snaking and Jackknifing, two different maneuvers are chosen: double lane change and Sharp cornering, respectively. In both maneuvers, the initial speed of the vehicle and road friction are set equal to 50 kph and 0.9, correspondingly. The given trailer is inherently vulnerable to snaking as its CG is located near the axle of the trailer. However, as mentioned, the vehicle turns more into jackknifing instability as the trailer CG becomes closer to the hitch point. Thus, to excite this instability mode, a trailer payload is added near the hitch point.

Table 4.2 presents the hyper-parameters of the MPC controller and the control allocation. The time step, the number of prediction horizon, and the control horizon for the MPC controller are set equal to 10 ms, 15, and 154, respectively. The step time is the sampling time of the control unit hardware (dSpace Micro AutoBox II) which is used for the experimental validation and considered a common value that the control unit of newly manufactured vehicles utilizes. The number of prediction horizon and control horizon are chosen carefully to prevent excessive computational burden while the accuracy and the performance of the controller are not affected noticeably. It is notable that to disable an actuator in the control allocation module, its lower and upper bounds are both set equal

to zero.

Table 4.2: Hyper-parameters of the MPC controller for stability control-Simulation

Parameter	Description	Value
T	Time step	0.01
h_p	Number of prediction horizon	15
h_c	Number of control horizon	15
$\boldsymbol{Q}$	Reference tracking weight	100
$\boldsymbol{R}$	Control effort increment weight	$\text{diag}([1e^{-3}, 4e^{-4}, 1e^{-5}])$
$\boldsymbol{S}$	Control effort weight	$\text{diag}([1e^{-3}, 4e^{-7}, 1e^{-5}])$
$\boldsymbol{E}$	Envelope weight	$1e^{3}$
$\boldsymbol{W}_{vu}$	CA tracking weight	$\text{diag}([10, 100, 10])$
$\boldsymbol{W}_{u}$	CA control effort weight	$\text{diag}([10, 10, 1, 100 \times \mathbf{1}_{6\times1}])$
$\boldsymbol{G}$	CA actuator importance weight	$I_{9\times9}$
ΔV^{max}	Maximum control effort increment	–
ΔV^{min}	Minimum control effort increment	–

Snaking - steering-based control actions: As discussed, a double lane change maneuver is performed to excite snaking instability. The initial speed of the vehicle is 50 *kph* and the driver applies the steering angle shown in 4.5-c. Also, the throttle is set to keep the vehicle's speed constant before starting the maneuver. The vehicle response is compared when the controller is switched on and off in Figure 4.4 where the steering-based control actions including AFS, ARS, and ATS are individually leveraged. In this maneuver, when the controller is disabled, hitch angle drastically increases as Figure 4.5-b illustrates and the vehicle goes beyond the stability margin and becomes unstable, Figures 4.4-a and 4.4-b.

As Figure 4.4 demonstrates, it is realized that both AFS and ARS can not only effectively prevent the vehicle from leaving the yaw rate bound of the stability envelope but also provide an acceptable yaw rate tracking. As explained, the main objective of the controller is that to avoid control intervention when the vehicle is in the stable region which is clearly noticeable in the results. For example, in Figures 4.4-a and 4.4-c, the vehicle is going to leave the yaw rate bound at $t = 4.4s$, thus, the controller is engaged at $t = 4.3s$ to correct the yaw rate of the vehicle, see Figure 4.5-a. Then, when the vehicle goes back to

the envelope at about $t = 4.8s$, the controller quickly drops the controller action to zero. The side bounds of the stability envelope are expected to limit the lateral slip angle of the second axle. This figure confirms that the controller is able to keep this angle inside the stability envelope. Needless to say, ARS utilizes the steering angle of the second axle, i.e., its lateral force, to modify the vehicle's behavior. Therefore, the lateral slip angle of the second axle in ARS reaches its limit compared to AFS, Figure 4.4-b and 4.4-d. Figure 4.5-c shows that the vehicle speed drop is about 5 and 8 kph over this maneuver for AFS and ARS, respectively.

Contrary to AFS and ARS, ATS is able to keep neither yaw rate nor the slip angle inside the stability bounds. The main reason is that at the time when the snaking is triggered, the hitch angle significantly increases in a short period of time and subsequently, the trailer tires quickly saturate as Figures 4.5-a and 4.5-d show. Due to this saturation, ATS cannot correct the vehicle response and keep it stable. It is important to note that the maximum allowable steering angle of the trailer is defined to be 20 degrees.

Snaking - braking-based control actions: The effectiveness of the Vehicle and trailer differential braking control actions are compared in Figures 4.6 and 4.7. As Figure 4.6 indicates, both control actions are successfully engaged to stabilize the vehicle and keep it inside the stability envelope. Nevertheless, there is a substantial difference in the braking torques applied by VDB and TDB, Figure 4.7-a. As Figure 4.7-c illustrates, larger braking torques applied by VDB considerably drops the vehicle speed (up to 23 kph) compared to TDB. These control actions mainly intervene when the vehicle is about to overpass the stability bound, Figure 4.7-a. Although the braking torques in VDB drop significantly when the vehicle goes back to the stability envelope, similar to TDB, they gradually return to zero.

Jackknifing - steering-based control actions: To trigger jackknifing in which vehicle yaw rate and hitch angle increase divergently without oscillation, an 800 kg trailer payload with 800 $kg.m^2$ yaw inertia is located at a distance of 1.8 m from the hitch point. The candidate maneuver used to stimulate this instability mode is a cornering maneuver in which a steering angle of 11° is applied within 0.5 s, kept there for 2.5 s, and finally returns to zero in 0.5 s (Figure 4.9-c). This steering angle sharply moves the vehicle toward high lateral accelerations which makes the vehicle unstable. In this maneuver When the controller is switched off, the yaw rate and the lateral slip angle of the second axle rapidly exceed the stability limits as Figures 4.8-a and 4.8-b present and subsequently hitch angle grows persistently.

As shown in Figure 4.8, AFS and ARS are able to make the vehicle stable, unlike ATS. AFS keeps the lateral slip angle considerably below its stability bound and brings

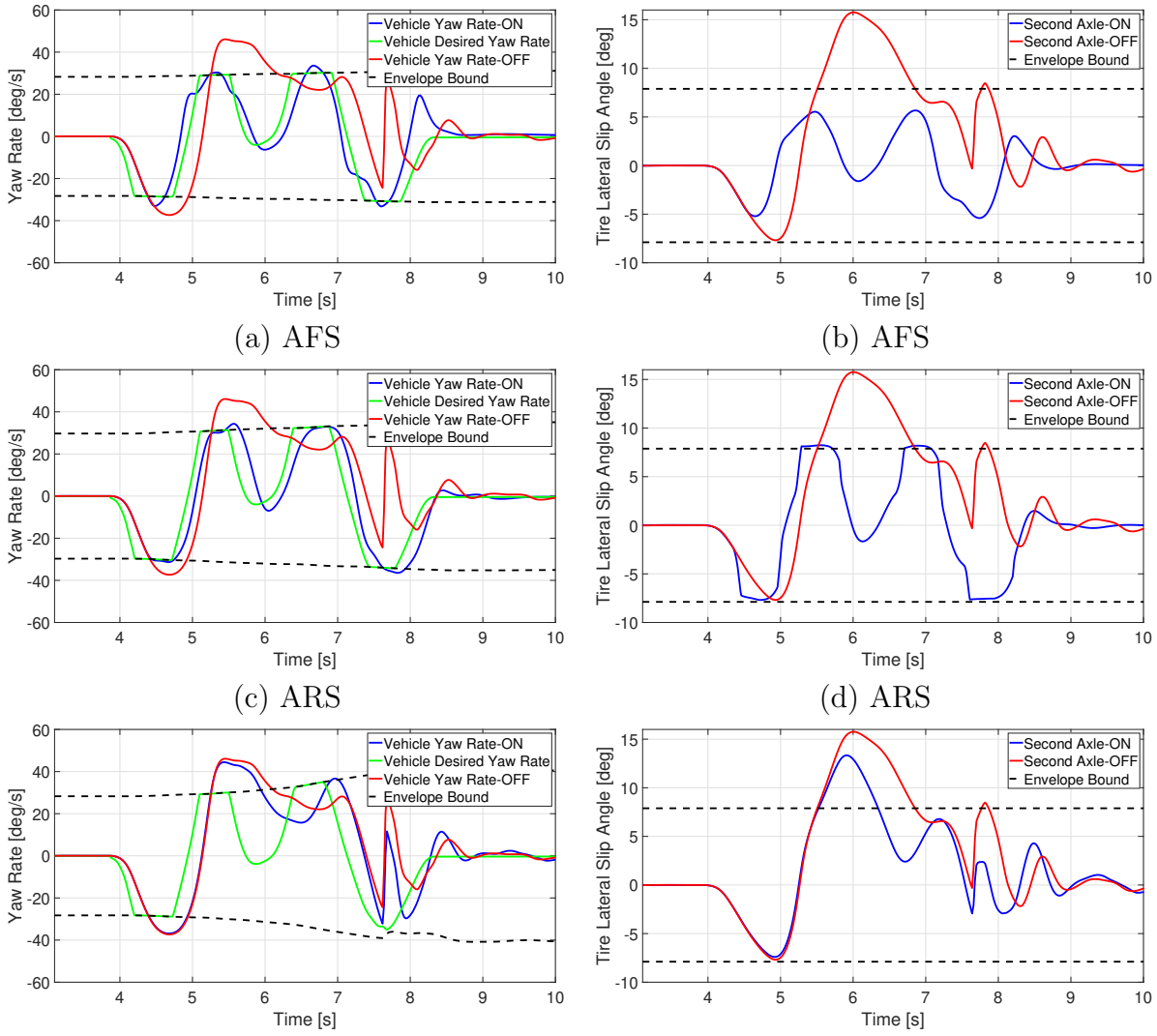

(a) AFS (b) AFS

(c) ARS (d) ARS

(e) ATS (f) ATS

Figure 4.4: Performance of the controller with the steering-based control actions in the double lane change maneuver

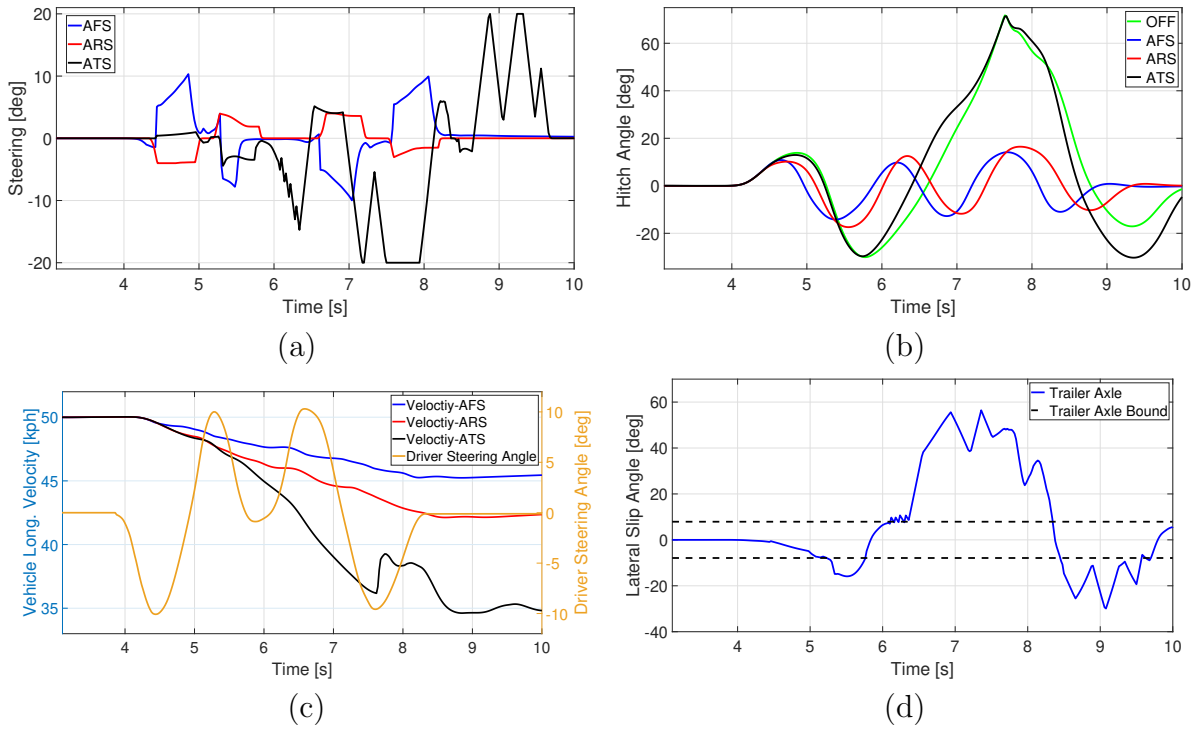

Figure 4.5: Performance of the controller with the steering-based control actions in the double lane change maneuver

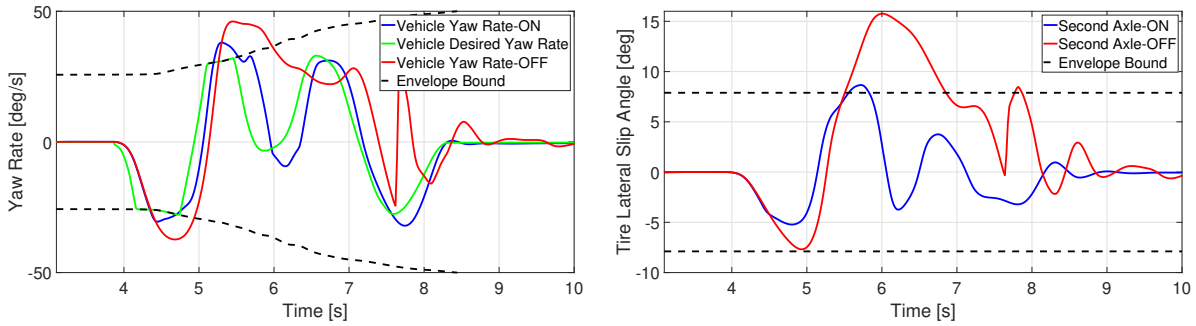

(a) VDB

(b) VDB

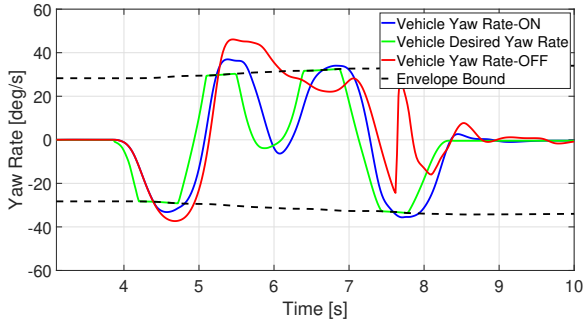

(c) TDB

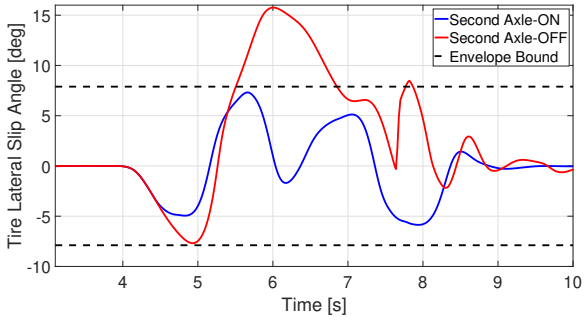

(d) TDB

Figure 4.6: Performance of the controller with the braking-based control actions in the double lane change maneuver

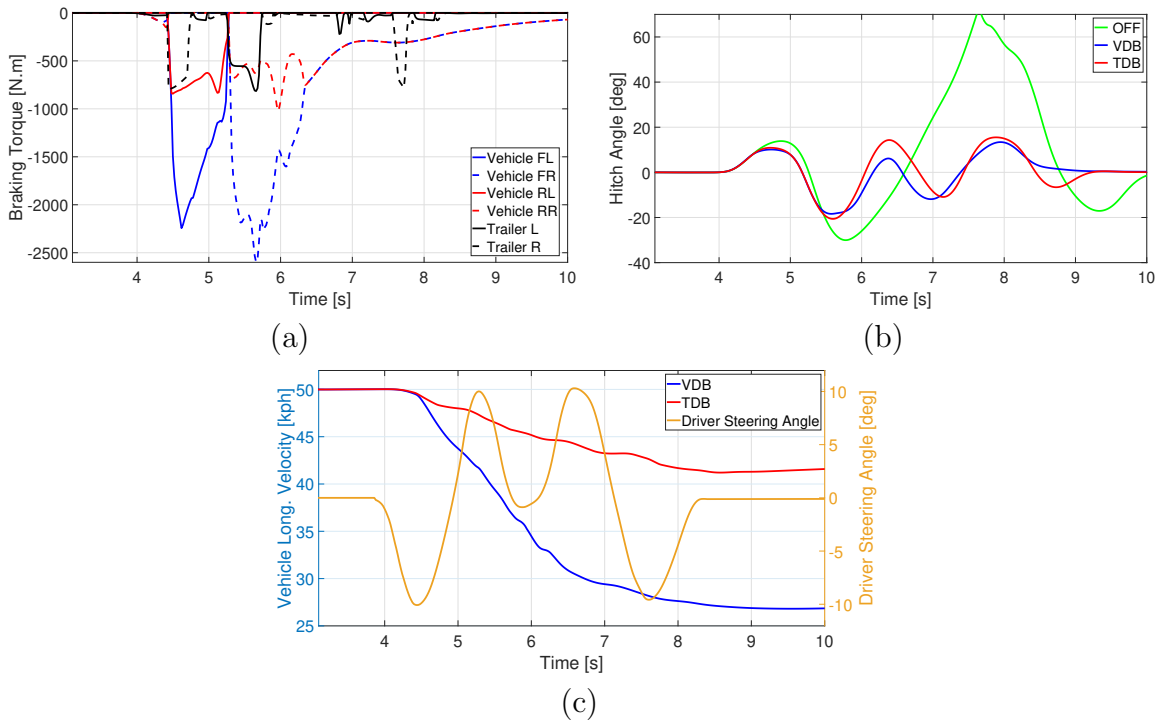

Figure 4.7: Performance of the controller with the braking-based control actions in the double lane change maneuver

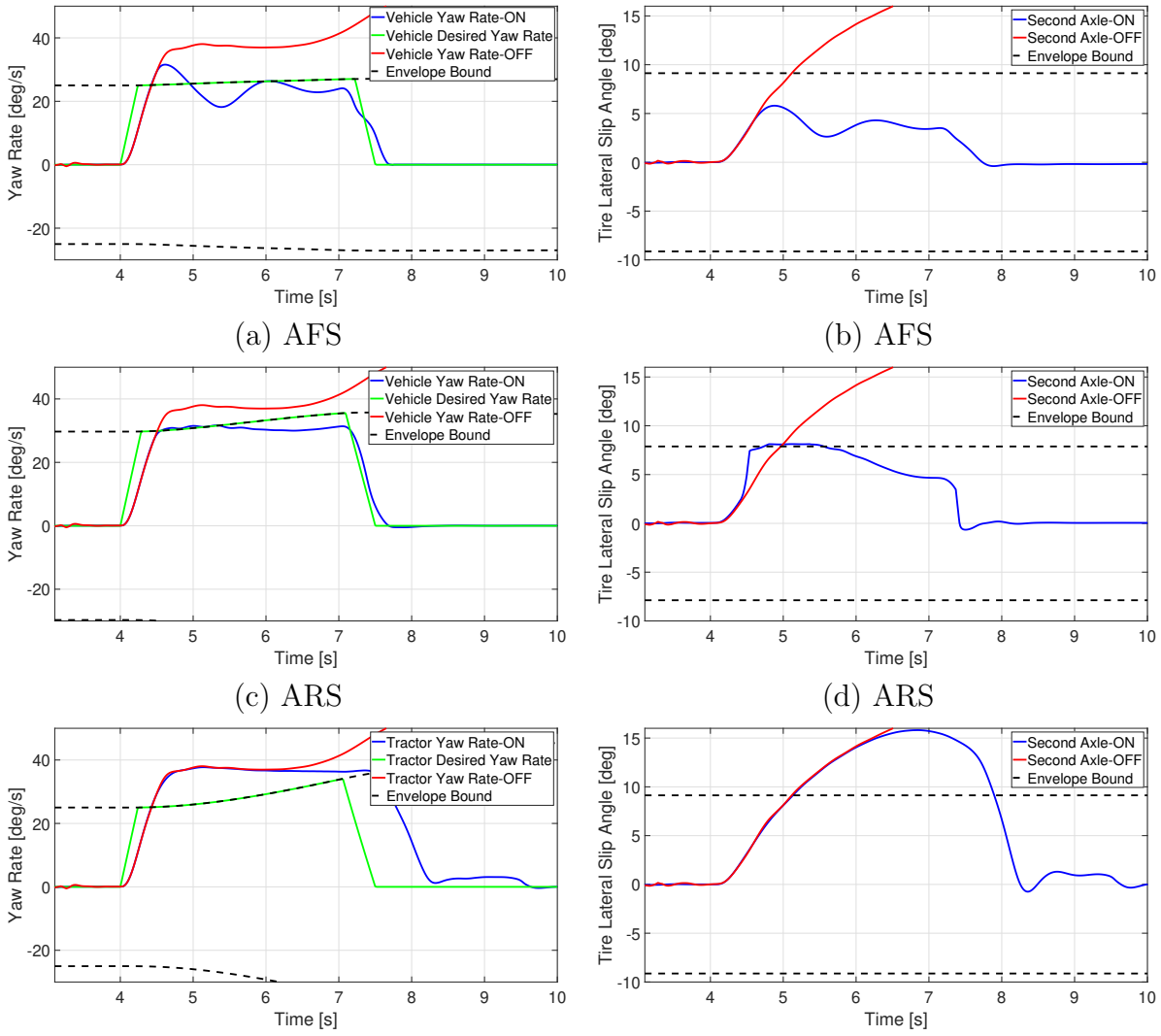

(a) AFS (b) AFS

(c) ARS (d) ARS

(e) ATS (f) ATS

Figure 4.8: Performance of the controller with the steering-based control actions in the cornering maneuver

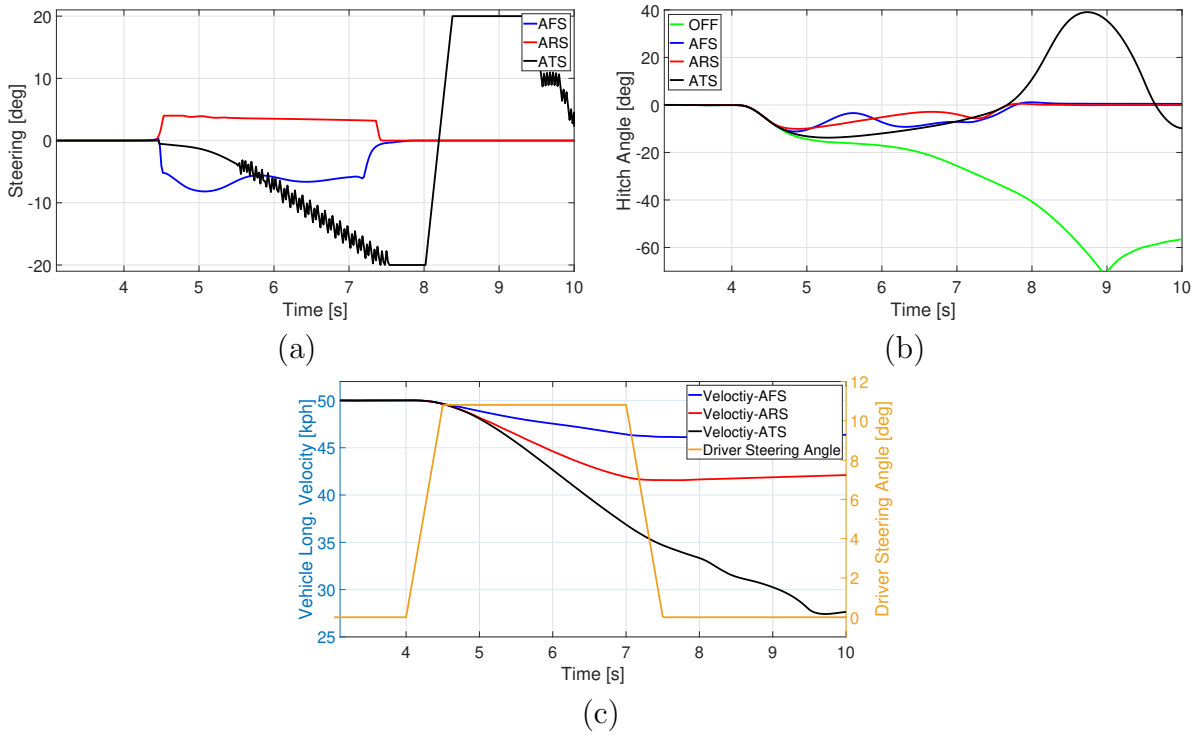

Figure 4.9: Performance of the controller with the steering-based control actions in the cornering maneuver

back the yaw rate inside the stable region, although, it shows oscillatory behavior at the beginning. Contrary to AFS, ARS effectively prevents the yaw rate from leaving the stability margin and provides better yaw rate tracking without oscillations. In addition, as discussed, the lateral slip angle in ARS reaches its limit to provide the required lateral force for stabilization, Figure 4.8-d. Figure 4.9-b shows that hitch angle is kept in a small range as the vehicle remains stable.

Similar to snaking instability, ATS fails to make the vehicle stable. Although it hampers the continuous yaw rate growth, Figure 4.8-e, it is not able to bring it back to the stable region. Moreover, the lateral slip angle keeps increasing which eventually makes the vehicle unstable, however, in this case, the vehicle remains stable since the steering is not applied for a long time.

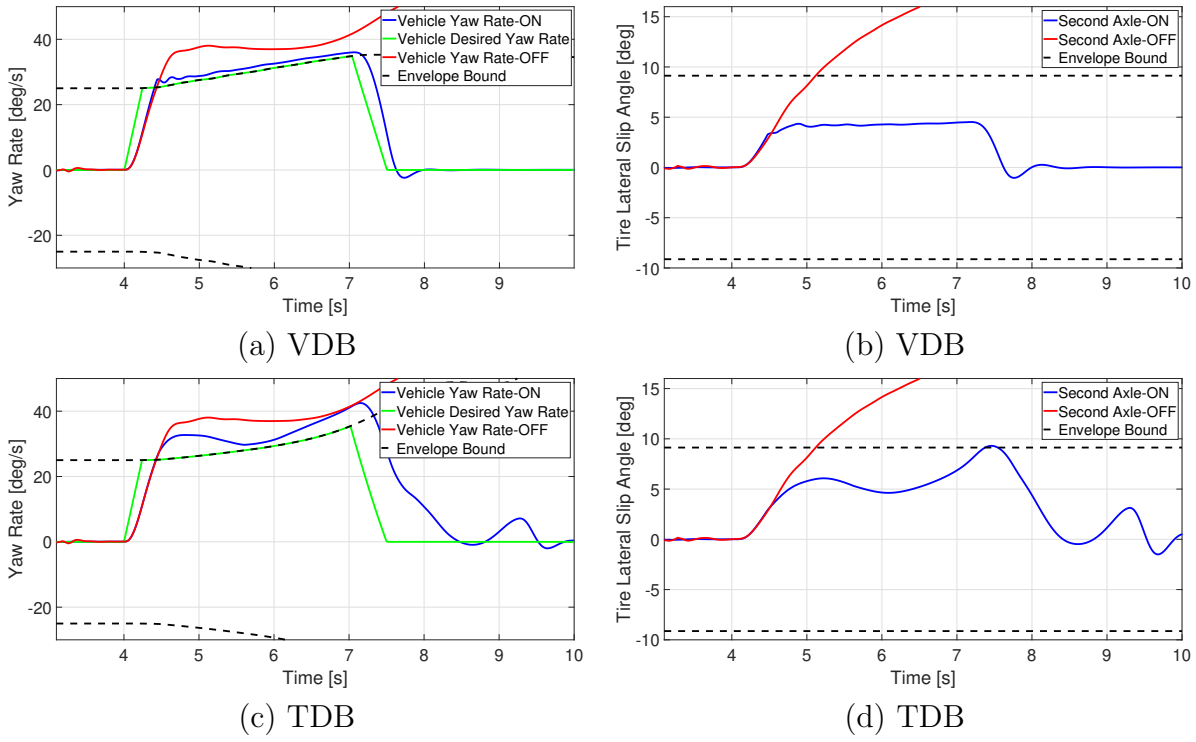

(a) VDB (b) VDB

(c) TDB (d) TDB

Figure 4.10: Performance of the controller with the braking-based control actions in the cornering maneuver

Jackknifing - braking-based control actions: Figures 4.10 and 4.11 show the simulation results of the cornering maneuver where the control actions are VDB and TDB. In this maneuver, VDB can stabilize the vehicle and prevents large yaw rates and lateral

slip angles illustrated in Figures 4.10-a and 4.10-b. However, unlike snaking mode, TDB is not able to retain stability for a long time. At the beginning of the maneuver, TDB is able to stop the growth of yaw rate and lateral slip angle but after about $t = 6s$ both yaw rate and the angle start to increase. As Figure 4.11-d indicates, the primary reason is that at the beginning, $t < 5s$, the trailer tires have enough capacity to provide the required corrective yaw moment, however, as trailer lateral acceleration goes up, this capacity reduces, the vehicle becomes unstable, and the hitch angle drastically increases, Figure 4.11-b.

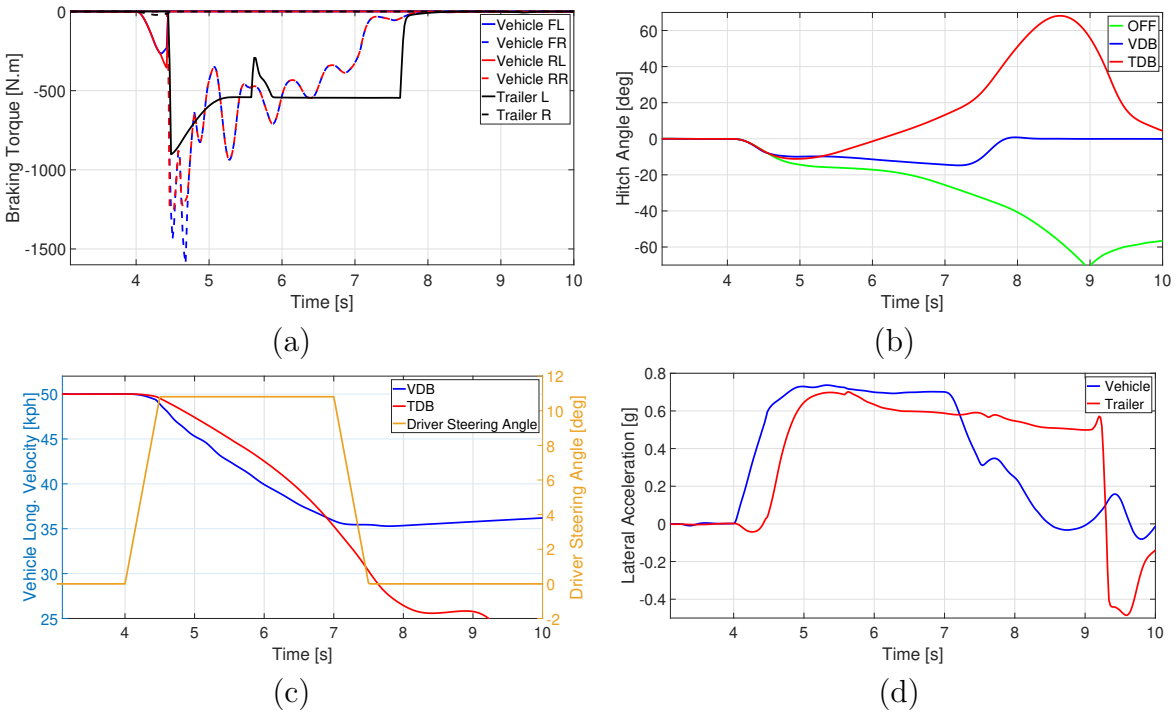

Figure 4.11: Performance of the controller with the braking-based control actions in the cornering maneuver

Control action integration: As explained, the proposed controller structure is expected to consider different control action configurations. In this regard, the controller performance is required to be investigated where different control actions are simultaneously operational. In this section, two different configurations are studied, first, a scenario in which the vehicle unit is equipped with one steering-based control action and one braking-based control action. In this situation, the tire capacity needs to be distributed among the actuators while preventing excessive demands. Second, each unit has a separate control action and they are combined to provide more effective/reliable stability control.

For the former case, the vehicle is equipped with VDB and ARS and the integration is evaluated in the snaking scenario discussed previously. The result of this simulation is presented in Figure 4.12 and compared with that of VDB. It can be seen that this integration has clearly improved the performance of VDB. Neither yaw rate nor lateral slip angle noticeably pass the stability bounds, Figures 4.12-a and 4.12-b, and also the speed drop in VDB which is about 23 *kph* is reduced to 10 *kph* in the integration case. For the

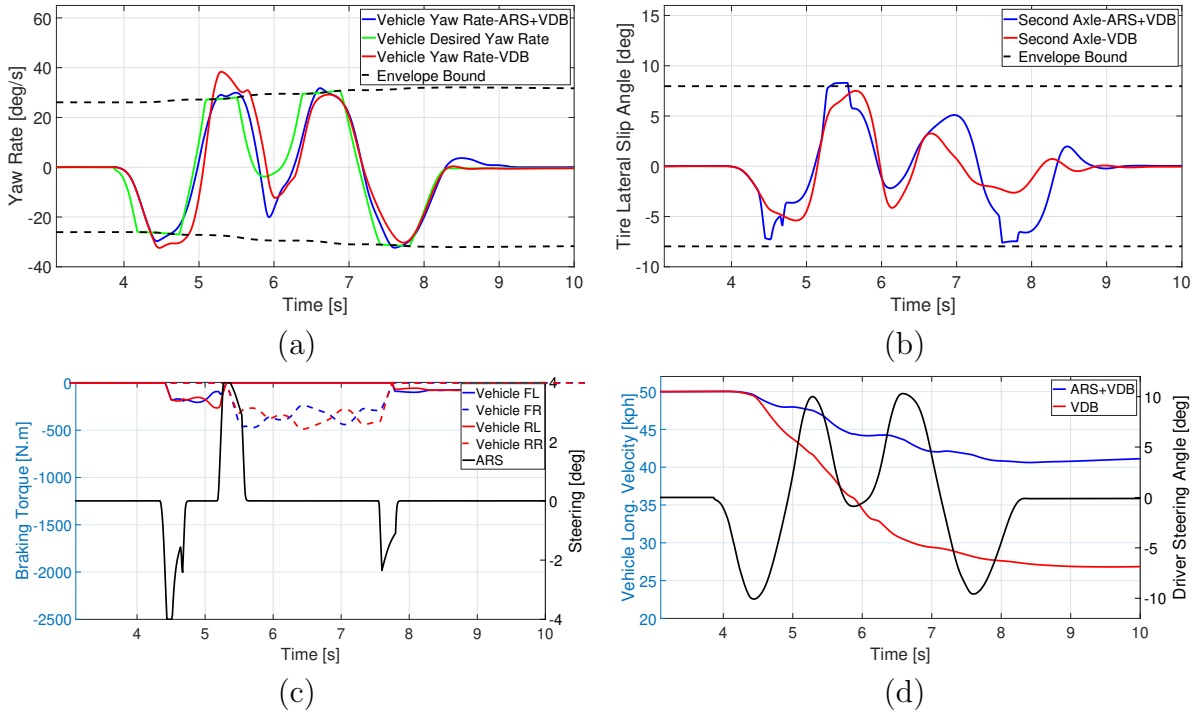

Figure 4.12: Performance of the controller with integrated VDB and ARS control actions in the double lane change maneuver

second scenario, the vehicle and the trailer units are equipped with differential braking, i.e., VDB and TDB, respectively. Figure 4.13 shows the result of the snaking maneuver that is chosen to assess the performance of the aforementioned integration. This integration does not show any tangible improvement compared to VDB only, however, the vehicle velocity drops less than VDB case, as Figure 4.13-d demonstrates, since the applied braking torques has been slightly decreased compared to VDB only, Figure 4.13-c.

Fault tolerance and robustness: One of the main advantages of the control allocation technique is that it can distribute the required forces and moments only among

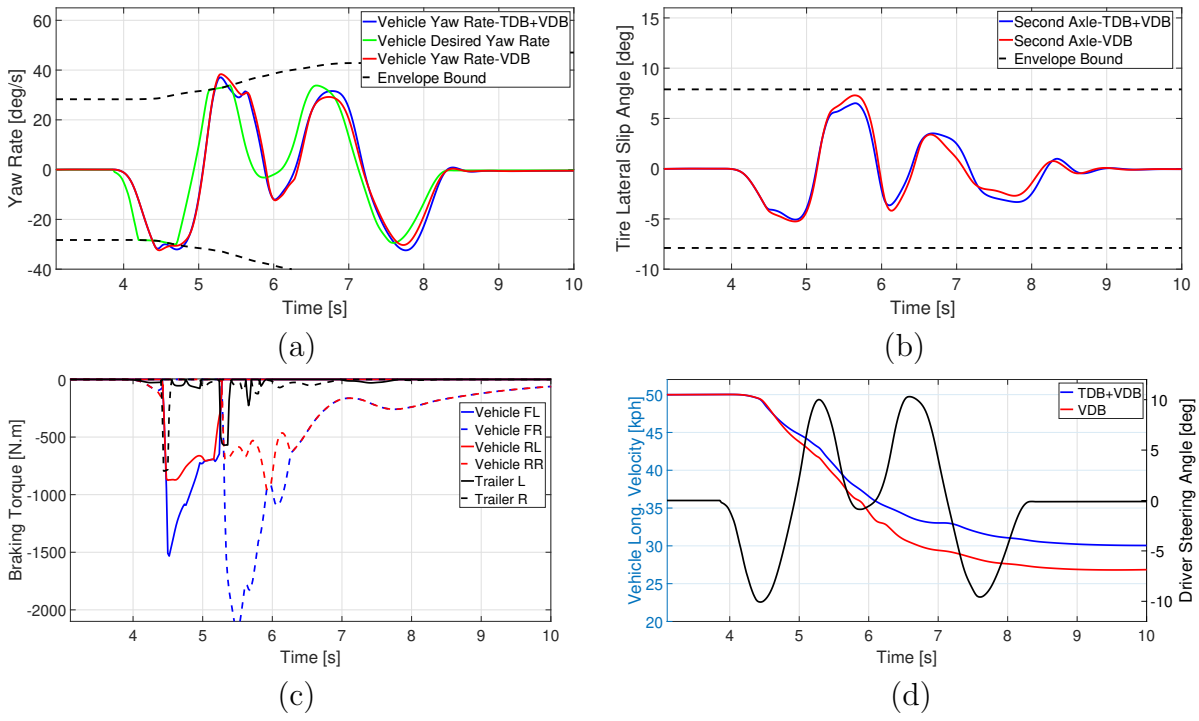

Figure 4.13: Performance of the controller with integrated VDB and TDB control actions in the double lane change maneuver

the operational actuators as their availability is updated in real-time at each time step. To evaluate the performance of the controller when an actuator fails, the same snaking maneuver is performed where the control action is VDB. However, at $t = 5s$ the braking actuator of the front-right (FR) wheel suddenly stops working meaning that the brake torque applied by this actuator is zero. To adjust the controller to the situation in which an actuator does not operate, its upper and lower limits in the controller allocation are set equal to zero not to be considered in the optimization process. The result of this simulation is shown and compared with the normal VDB in Figure 4.14. The results indicate that although the controller performance slightly degrades, the controller is able to keep the vehicle stable. Since the maximum corrective moment decreases in the case of failure, the yaw rate stays beyond its stability margin for a longer time, Figure 4.14-a and also the lateral slip angle overpasses its bound Figure 4.14-b.

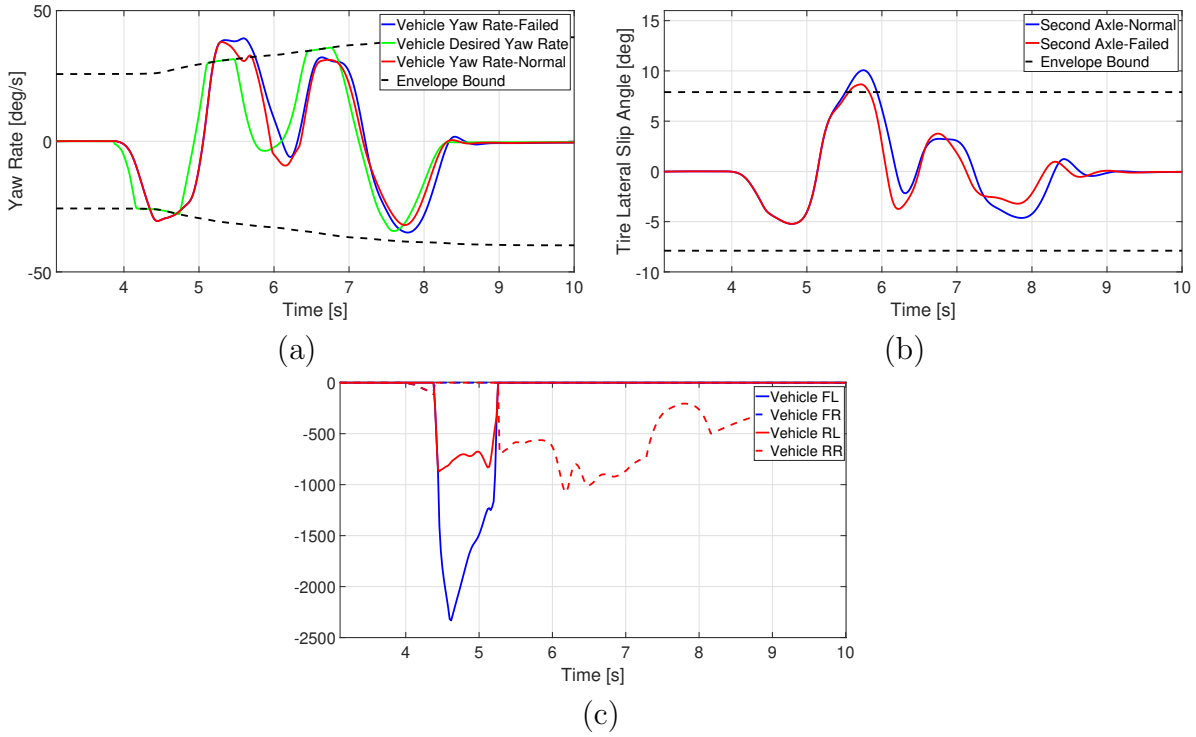

Figure 4.14: Performance of the controller with VDB control action in the double lane change maneuver when actuator failure occurs

Although the performance of model-based controllers mainly depends on the accuracy of the model, they need to handle the model uncertainty to a reasonable extent. This is

more important in vehicle trailers, as the estimated parameters of the trailer might not be adequately accurate, unlike the vehicle unit, or might have some variations owing to the payload. To assess the tolerance level of the designed controller, the mass and the yaw inertia of the trailer are increased about 30% while the original values in the model are kept unchanged. Besides, the trailer CG location is moved toward the rear end of the trailer for 20 cm. In this scenario, the actual trailer is heavier than the one used as the model in the MPC and the vehicle is more prone to snaking compared to the original trailer which makes it more challenging to stabilize. As Figure 4.15 shows, the performance of the controller is undermined as expected. Nonetheless, the controller is able to bring back the vehicle inside the stability envelope even though the lateral slip angle goes beyond its limit moderately.

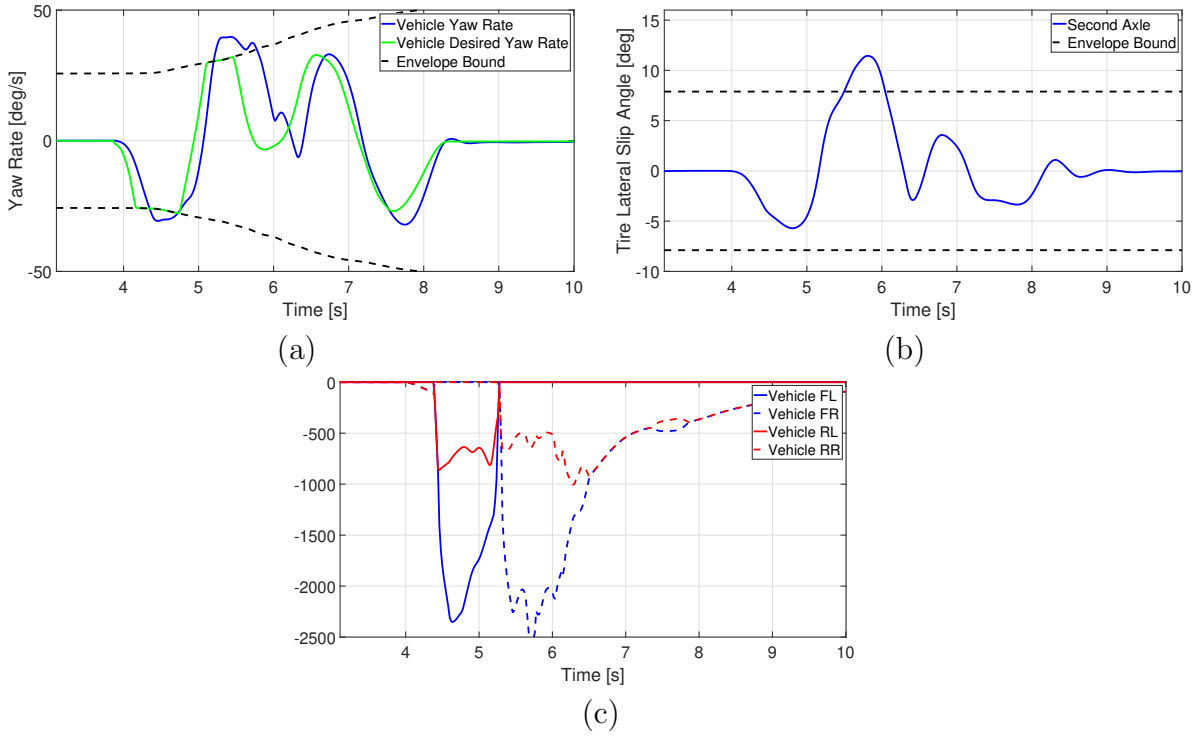

Figure 4.15: Performance of the controller with VDB control action in the double lane change maneuver where the estimated properties of the trailer are not accurate

Figure 4.16: The electric all-wheel-drive Chevrolet Equinox vehicle and the trailer attached

4.3.2 Experimental Results

To validate the proposed envelope controller presented in Section 3.3, experimental tests are conducted on a vehicle trailer in which the control action is VDB. The test vehicle is an all-wheel-drive electric vehicle Chevrolet Equinox attached to a research trailer (Figure 4.16). The vehicle is equipped with independent brake modules on each wheel that provide differential braking capability. The structure of the experimental setup is shown in Figure 4.17, in which the MPC controller and the qpOASES are implemented in the Simulink environment, and then compiled on dSPACE MicroAutoBox. The MicroAutoBox communicates with the sensors and the actuators through CAN bus. The vehicle lateral acceleration and the vehicle yaw rate are provided by the vehicle IMU; the vehicle lateral and longitudinal velocities are received from a 6-axis GPS (RT2500). The hitch angle and its rate are measured with a magnetic field induced sensor which is used as a vehicle suspension height measuring device.

Table 4.3 presents the main parameters of the vehicle-trailer system used in the experimental tests. Note that those values presented as the cornering stiffness of the tires, e.g., $C_{\alpha 1}$, $C_{\alpha 2}$, and $C_{\alpha 3}$, are calculated when the trailer is not attached to the vehicle and there is no payload on the trailer. The hyper-parameters of the MPC controller are presented in Table 4.4. The time step, the number of prediction horizon, and control horizon for the MPC controller are set equal to 10 ms, 15, and 15, respectively. Since VDB is the only control action available on the vehicle, only the vehicle yaw moment is considered the

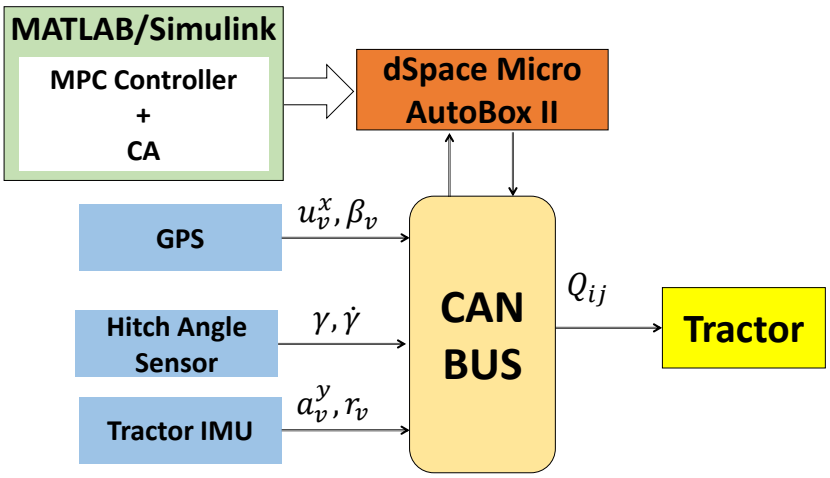

Figure 4.17: Experimental setup network

virtual control action and the rest are disabled by setting their lower and upper bounds as zero. Also, the distribution between the first and the second axles is performed based on their remaining capacity which is implemented using matrix **G** which defines the relative importance of the actuators.

Figure 4.18 illustrates the response of the vehicle without the controller in the accelerating slalom maneuver on a dry road ($\mu = 0.9$). The applied steering angle and vehicle's longitudinal velocity are shown in Figure 4.18-d. As Figure 4.18-a presents, the yaw rate of the vehicle increases divergently as the speed increases, as expected. After $t \approx 9.3$ s,

Table 4.3: Corresponding values for baseline-vehicle parameters.

Parameter	**Value**	**Parameter**	**Value**
m_v $[kg]$	2270	I_t^z $[kg.m^2]$	291
I_v^z $[kg.m^2]$	4605	l_3 $[m]$	0
l_1 $[m]$	1.42	l_{h2} $[m]$	1.80
l_2 $[m]$	1.44	$C_{\alpha 1}$ $[N/rad]$	94748
l_{h1} $[m]$	2.58	$C_{\alpha 2}$ $[N/rad]$	103235
m_t $[kg]$	755	$C_{\alpha 3}$ $[N/rad]$	56108

Table 4.4: Hyper-parameters of the MPC controller for stability control-Experimental

Parameter	**Description**	**Value**
T	Time step	0.01
h_p	Number of prediction horizon	15
h_c	Number of control horizon	15
$\boldsymbol{Q}$	Reference tracking weight	50
$\boldsymbol{R}$	Control effort increment weight	$\text{diag}([--, 5e^{-4}, --])$
$\boldsymbol{S}$	Control effort weight	$\text{diag}([--, 1e^{-6}, --])$
$\boldsymbol{E}$	Slack weight	$1e^{3}$
$\Delta M_v^{z.max}$	Maximum control effort increment	200
$\Delta M_v^{z.min}$	Minimum control effort increment	-200

the yaw rate reaches its stability bound, and at $t \approx 11.3$ s goes beyond this limit; consequently, the hitch angle starts to increase divergently indicating the initiation of snaking instability, and finally reaches 60 degrees, Figure 4.18-c. However, the driver reduces the steering angle as well as longitudinal velocity to keep the vehicle under control. This figure also shows that the vehicle yaw rate bounds are carefully defined, and the vehicle should be prevented from passing this limit. In this maneuver, the lateral slip angle of the second axle also grows as the vehicle's yaw rate increases.

This maneuver is repeated with the controller switched on. This time, as Figure 4.19 demonstrates, the maneuver is continued for a longer time to prove that the controller is able to steadily keep the vehicle inside the stability envelope. However, due to the effect of differential braking in speed reduction, the vehicle's longitudinal velocity does not exceed 42 kph during the maneuver, Figure 4.19-e. In Figure 4.19-a, the yaw rate of the vehicle appropriately follows the desired rate, especially when the vehicle is in the safe region and away from the yaw rate bounds. This originates from the fact that the vehicle's dynamic behavior, in the linear region of the tire, is almost the same whether the trailer is attached or not. In contrast, close to the stability envelope when the controller engages, the vehicle's yaw rate slightly deviates from the desired rate caused by the strong dynamic effects of the trailer and the corrective yaw moments applied by the controller to maintain the vehicle stable. Keeping the vehicle inside the stability envelope allows the driver to continue the maneuver for a longer time without any hitch angle intensification, as Figure 4.19-d indicates, meaning the vehicle remains steadily stable.

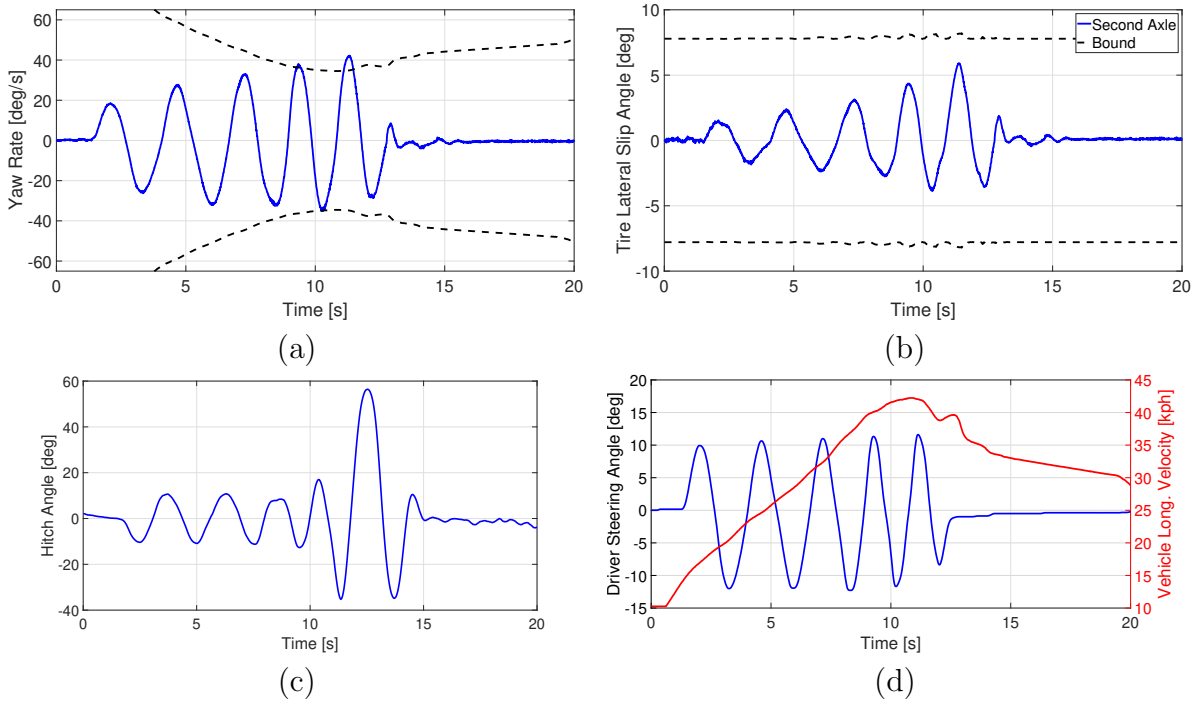

Figure 4.18: Experimental test results of the vehicle without controller in the accelerating slalom maneuver

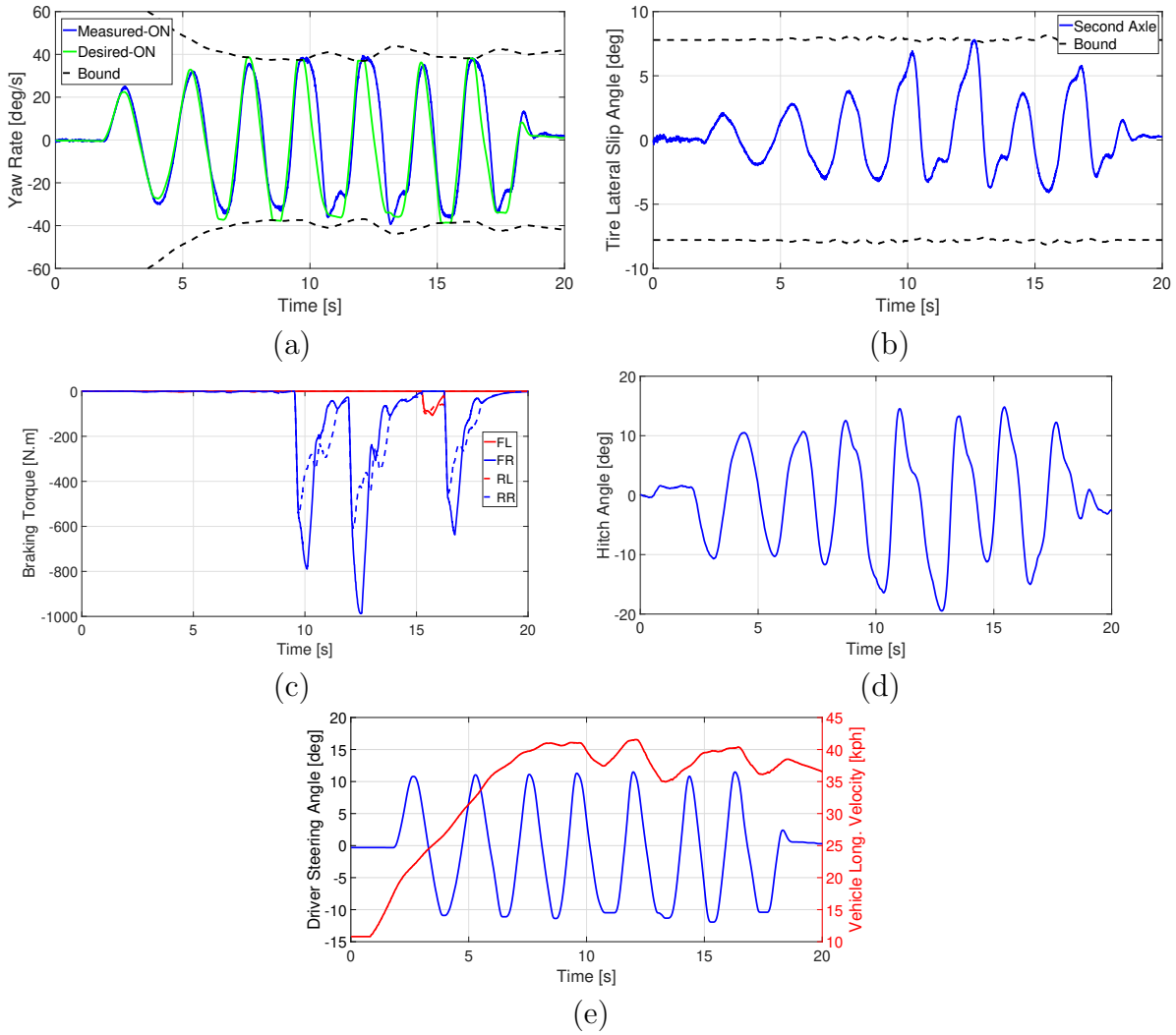

Figure 4.19: Experimental test results of the vehicle with controller in the accelerating slalom maneuver.

The applied braking torques on the vehicle are illustrated in Figure 4.19-c. As observed, when the vehicle is in the safe region and adequately below the vehicle's yaw rate and the lateral slip angle bounds, the controller nearly does not apply any corrective yaw moments (before $t \approx 9.5$ s) as one of the controller's main purpose. Although, when the vehicle is predicted to exceed the stability envelope, the controller kicks in to prevent it from entering the unsafe region.

Figure 4.20 shows the results of a double change maneuver on a dry road ($\mu = 0.9$) with an initial speed of 44 kph. Similar to the slalom maneuver, the controller prevents the vehicle from leaving the stability envelope, Figures 4.20-a and 4.20-b. The controller significantly intervenes at those time that the vehicle is about to leave the envelope including $t = 6.3s$, $t = 7s$, and $t = 8.3s$ and the braking torques gradually return to zero when the vehicle enters the stable region, Figure 4.20-c.

4.4 Summary

This chapter was dedicated to develop an optimization-based reconfigurable control structure for vehicle-trailer systems. This control structure included two hierarchical layers and its main objective was to prevent the vehicle from leaving the stability envelope. In the upper layer, an MPC was developed through a quadratic performance index formulation using the affine bicycle model. By solving this quadratic problem with respect to the control action and state constraints, the optimal virtual control actions were obtained and sent to the lower layer for optimal distribution. The lower layer, which provided reconfigurability, was a control allocation technique that optimally transformed the virtual control actions into actuator commands, steering and/or braking. This technique was able to take the capacity of the tires and the actuators into account.

The performance of the proposed control structure was evaluated in snaking and jackknifing instability modes with different control actions and their combinations. The simulations exploited high fidelity CarSim model and controller was implemented in MATLAB/Simulink. The results indicated that the proposed control structure is reconfigurable for different control actions. It is also tolerant to actuator failure and robust to inaccurate trailer parameter estimation. However, among the studied control actions, active trailer steering failed to stabilize the vehicle in both snaking and jackknifing and trailer differential braking was not able to keep the vehicle inside the stability envelope in jackknifing.

The developed MPC controller along with stability envelope was also assessed through experimental tests. The experimental results were also confirmed that the stability envelope was carefully defined and the vehicle remains stable if it stays inside the envelope.

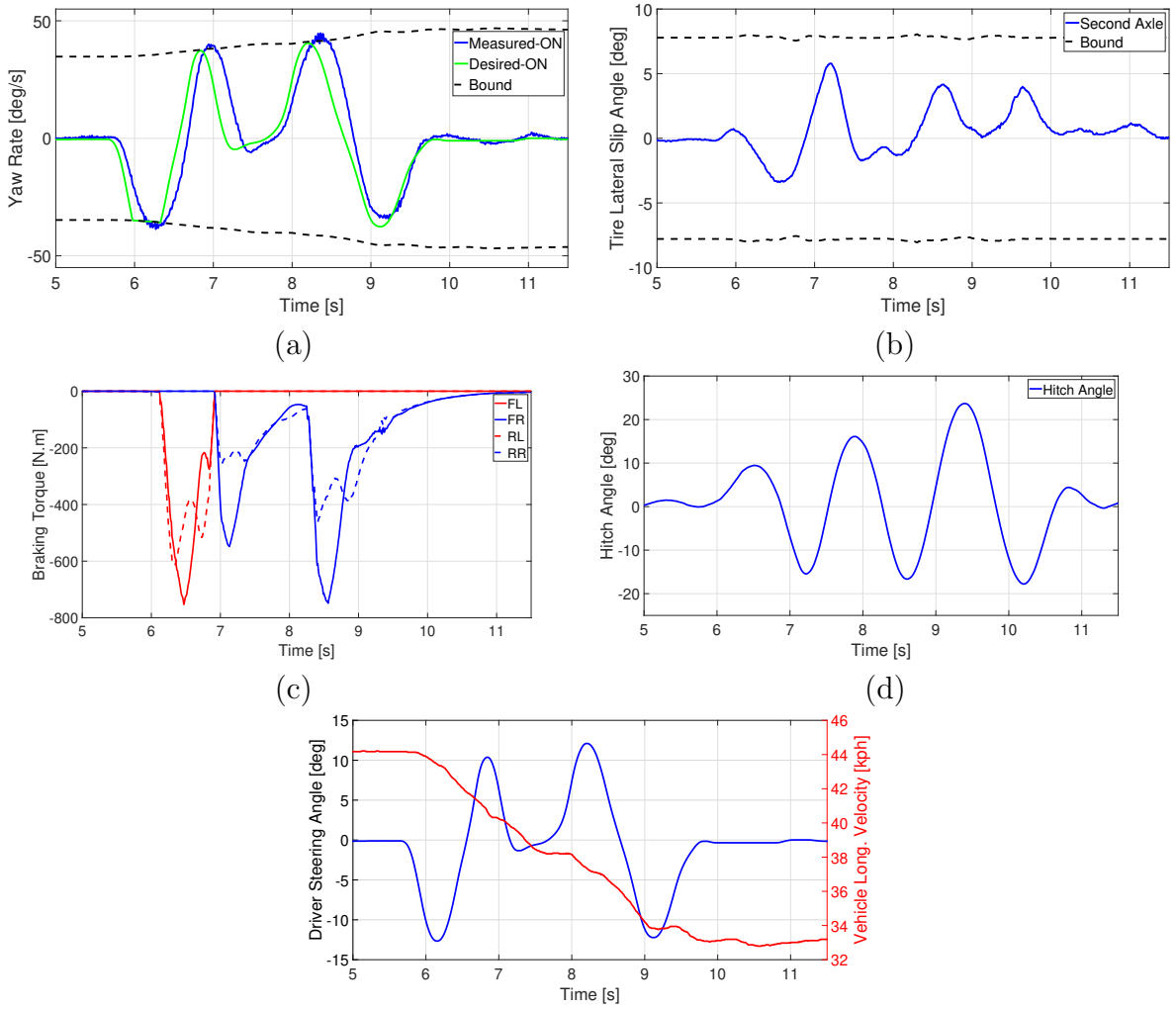

Figure 4.20: Experimental test results of the vehicle with controller in the double lane change maneuver

Chapter 5

Hybrid A*-Based Motion Planning for Vehicle-Trailer Systems

In this chapter, first, the previously introduced affine bicycle model is extended to serve as the prediction model in the MPC formulation required for trajectory tracking. Then, a hybrid A*-based motion planning module is developed to generate a feasible, safe, and comfortable local trajectory for an autonomous vehicle. This module considers obstacles, road lanes/bounds, and vehicle dynamic constraints, and also prioritizes obstacles by assigning different weights to them according to their time to collision distance and avoidance requirements. In addition, this path planner is able to take trailer effects, including its dynamics and off-tracking, into account in a systematic manner to ensure that the generated trajectory is collision-free and feasible. In the proposed motion planning module, a hybrid A* algorithm is utilized to find a path between the current location of the vehicle and target location assuming the speed is constant, and then the speed profile is optimally specified considering the proximity to obstacles along the defined path, traffic speed, road curvature, and the maximum allowable lateral and longitudinal accelerations.

In this motion planner, a generated trajectory needs to satisfy three main characteristics: feasibility, safety, and comfort. To provide a feasible trajectory, the motion planner verifies whether following the planned trajectory will require a control action beyond the capacity of the vehicle and tires. In this regard, the maximum allowable control action and also the stability envelope developed in Section 3.3 are considered in the motion planning process. Additionally, at low speed, although the planned trajectory might be feasible for a single-vehicle, where the trailer is attached, the motion planner needs to ensure that the trailer does not violate any obstacle avoidance constraint and road bound due to the longer length of the vehicle and the trailer off-tracking problem.

For safety purposes, the motion planner defines the obstacle-free area by eliminating the search area from the space occupied by obstacles. This approach guarantees that the provided trajectory avoids any obstacles that would cause collision; however, it is not necessarily a safe driving behavior as the generated trajectory might be dangerously and unnecessarily close to obstacles. As a solution, the potential field method is leveraged to keep the trajectory away from the obstacles and also to preserve that space to be used in case of emergencies.

The hybrid A* algorithm finds the shortest path between the current location and the target location of the vehicle. However, the generated trajectory is not essentially comfortable for passengers as it might cause high lateral accelerations. In this motion planner, to prohibit such maneuvers in normal driving scenarios, the vehicle is not allowed to exceed a certain level of acceleration, although this limitation is ignored in emergency situations owing to safety concerns.

5.1 Trajectory Tracking Affine Bicycle Model

Driving an autonomous vehicle along a trajectory, which is called trajectory tracking, requires that appropriate inputs (fundamentally steering angle and longitudinal acceleration) be applied. The main goal of trajectory tracking is to keep the vehicle close to the path, minimize the lateral deviation and the heading angle error between the vehicle and the target path, and follow the required speed while the vehicle remains stable. In this regard, the first step is to transform the state variables of the dynamic model into another set of state variables with an appropriate coordinate system (path coordinate is chosen here). The next step is to define the required variables that are meant to be controlled for better performance. In this trajectory tracking controller, in the longitudinal direction, the controller needs the vehicle's speed at its maximum allowable unless there is an obstacle as explained later in this chapter. In the lateral direction, the deviation of the vehicle's CG with respect to the target path needs to be minimized, both lateral and heading errors. Figure 5.1 shows the heading error $\Delta\psi$ and the lateral error e, both of which determine the position of the vehicle-trailer system relative to the target path.

If the vehicle remains stable during the maneuver, i.e., β_v is small, the dynamic of these errors is expressed as

$$\Delta\dot{\psi} = r_v - u_v^x K(s) \tag{5.1}$$

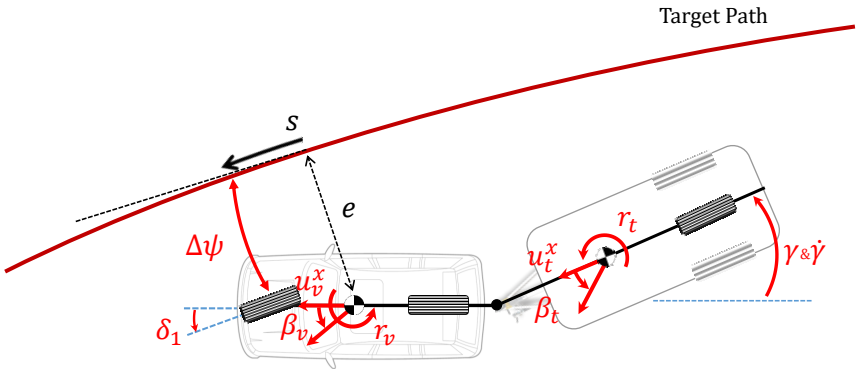

Figure 5.1: Schematic of the trajectory tracking model and the lateral and heading errors

$$\dot{e} = u_v^x \sin(\Delta\psi) + u_v^x \beta_v \cos(\Delta\psi) \tag{5.2}$$

where $K(s)$ is the curvature of the target path. With the assumption that the heading error is small, Equation 5.2 can be rewritten as

$$\dot{e} = u_v^x \Delta\psi + u_v^x \beta_v \tag{5.3}$$

For the longitudinal control, a kinematic model is used that is expressed as

$$a_v^x = \dot{u}_v^x \tag{5.4}$$

$$\dot{s} = u_v^x \cos(\Delta\psi) - u_v^x \beta_v \sin(\Delta\psi) \tag{5.5}$$

where s is the distance along the target path. Assuming the heading error is small, Equation 5.5 is rewritten as

$$\dot{s} = u_v^x - u_v \beta_v \Delta\psi \approx u_v^x \tag{5.6}$$

As a result, the affine bicycle model developed in Section 3.2.1 can be augmented by Equations (5.1), (5.3), (5.4), and (5.6) to represent a trajectory tracking state-space model as

$$\dot{x}_p = \mathbf{M}_p^{-1}(\mathbf{A}_p x_p + \mathbf{B}_p U_p + w_p), \quad y = \mathbf{C}_p x_p \tag{5.7}$$

where

$$w_p = \mathbf{F}_p f^y + \mathbf{L}_p \bar{\alpha} + \mathbf{E}_p K \tag{5.8}$$

$$x_p = \begin{bmatrix} \beta_v & r_v & \dot{\gamma} & \gamma & u_v^x & s & e & \Delta\psi \end{bmatrix}^T \tag{5.9}$$

$$U_p = \begin{bmatrix} \delta_1 & a_v^x \end{bmatrix}^T \tag{5.10}$$

In this model, the steering angle of the front axle and the longitudinal acceleration are defined as the model inputs. Matrices $\mathbf{M}_p$, $\mathbf{A}_p$, $\mathbf{B}_p$, $\mathbf{F}_p$, $\mathbf{L}_p$, $\mathbf{E}_p$, and $\mathbf{C}_p$ have been defined in Appendix A.3.

5.2 Autonomous Vehicle Architecture

Figure 5.2, illustrates the correlations between different layers/modules of the autonomous vehicle architecture. At each time step, the data acquisition layer collects all of the information either received by the sensors or estimated, all of which can be divided into three main categories: obstacle information, road information, and ego vehicle information. The obstacle information consists of the size, position, and velocity in the horizontal plane coordinates. The road information includes road profile, the number of lanes and their width, road curbs, and road friction. The vehicle information consists of the vehicle's location, axial and angular velocities, and axial accelerations.

In the perception layer, the collected information is used to localize the ego vehicle by finding its lateral deviation and heading angle with respect to the centerline of the current lane. The objects are also detected and classified, and their possible movements are predicted. The decision-making layer utilizes the information coming from the perception layer to ultimately provide the trajectory that the vehicle needs to follow. In this layer, the final destination of the vehicle and its route are determined by the global planning module, and the behavioral planning module sets local goals for the motion planning module such as lane change, merging, and pullover. Finally, the planned trajectory provided by the motion planning module is followed by the control layer by applying steering and brake/throttle commands.

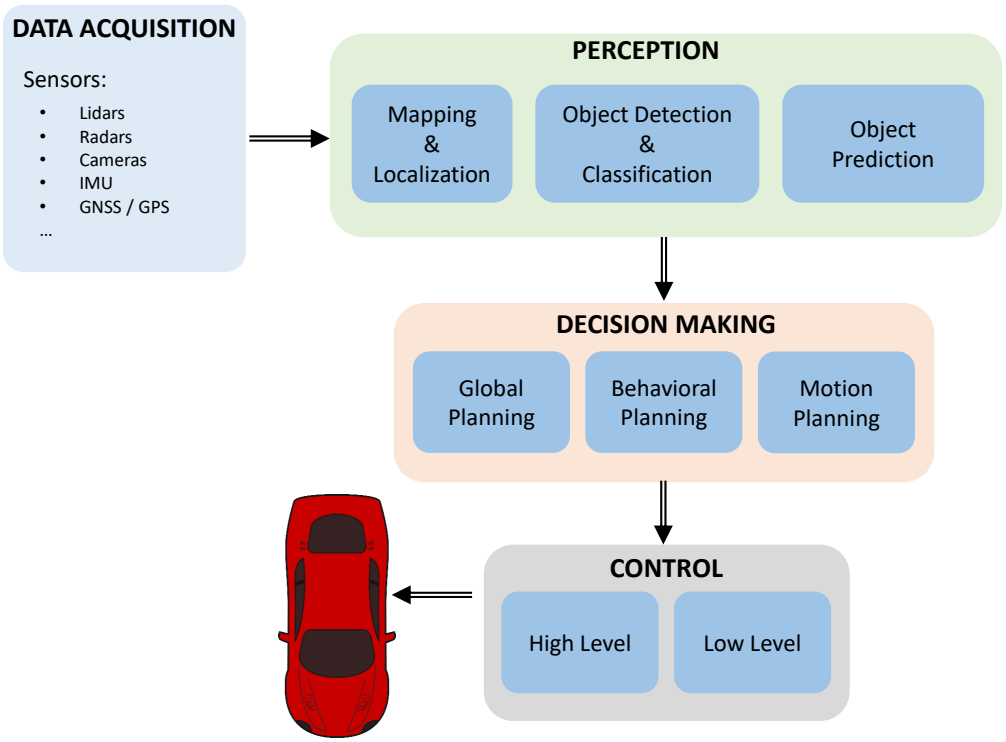

Figure 5.2: Autonomous vehicle architecture

5.3 Hybrid A* Algorithm

5.3.1 Fundamentals

In this section, the basic concepts and terminologies that are essential for understanding the hybrid A* algorithm are discussed. The content of this section is mostly from [76].

Configuration space: To facilitate the formulation of graph-based path planning algorithms, the concept of configuration space has been assigned. If $\mathcal{A}$ is an agent (vehicle) in a two dimensional plane world $\mathcal{W}$, each possible configuration of the agent $\mathcal{A}(q)$ is defined by a vector q in the form of $q = [x \quad y \quad \psi]^T$ in which x, y, and ψ are, respectively, the longitudinal position, lateral position, and heading angle measured with respect to the coordinate frame. A set of all possible configurations q is the configuration space, denoted as C. This configuration space is divided into two subsets: the collision-free configuration space $\mathcal{C}_f$ and the obstacle configuration space $\mathcal{C}_o$. The vehicle is in collision with obstacles if $\mathcal{A}(q) \cap \mathcal{O} \neq \emptyset$, where $\mathcal{O}$ is the obstacles in the world [76]. Since the explained configuration space is static and the agent is dynamic, the state space of the agent x can be mapped to the configuration of the agent q using the dynamic model of the agent.

Configuration space division In the A* algorithm, as the base of the hybrid A* algorithm, the configuration space is divided into rectangular cells while their edges are parallel to the axis of the space. Here, those cells that are fully or partially occupied by obstacles are considered obstacle configuration space $\mathcal{C}_o$ (grey cells in Figure 5.3), and the rest are viewed as collision-free configuration space $\mathcal{C}_f$ (white cells in Figure 5.3). It is notable that on the two-dimensional horizontal plane upon which the proposed motion planning is developed upon, only the x-axis and the y-axis of the configuration space are decomposed.

Graph search fundamentals: A graph G is represented by a set of vertices (states/nodes) V, $V = V(G)$, and a set of edges (trajectories/arcs) E, $E = E(G)$, connects the vertices, see Figure 5.4. Those vertices that have at least one edge in common are called neighbors. In the graph search, only a finite number of actions can be used to change the state of the agent from an initial state to a target state. In path planning, an agent starts from an initial state x_0 and moves toward the goal state x_g by choosing an action from a finite action space $U(x)$. Once the current state is known and a new action has been selected, a state transition function f (kinematic/dynamic model) generates a new state x' as $x' = f(x, u)$ in which $u \in U(x)$ and $x', x \in X$, where X is a nonempty state space.

To relate the graph and state-space representations, it can be said that a vertex V of a graph G is the state-space X of the agent. As the edges E connect the vertices, they

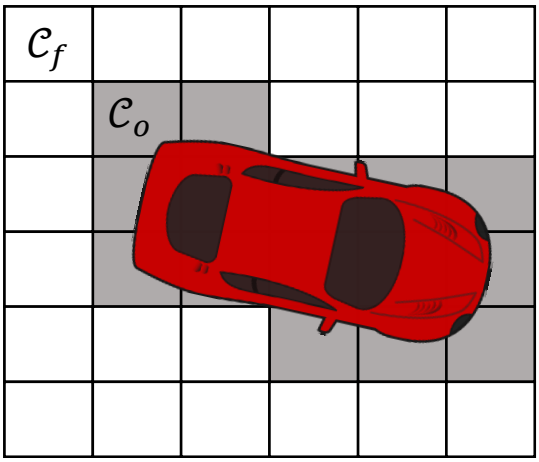

Figure 5.3: State space subdivision

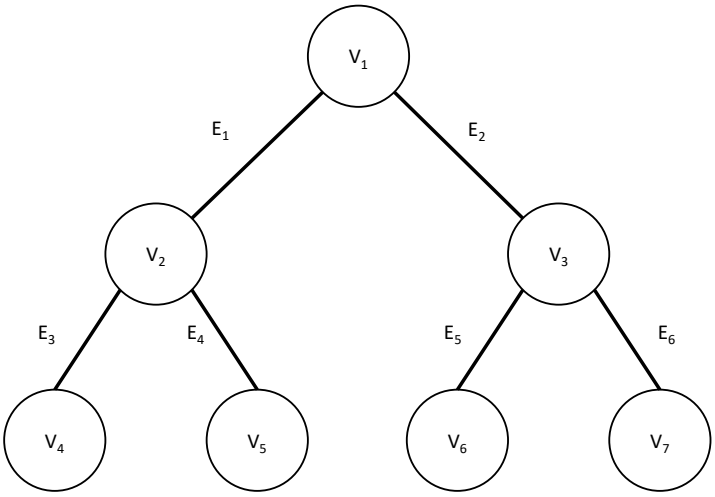

Figure 5.4: Graph representation

can be considered the action space $U(x)$. In other words, the agent at each state (vertex) x takes an action u (Edge) to move to a new sate x' (neighbor vertex) using the state transition function f.

Open and closed lists: In graph-based algorithms, at each vertex, all possible actions, available at that vertex are taken, and new vertices are generated. This process is called expansion. The newly generated vertices are added to the open list that contains all of the expanded vertices and forms a set of search frontiers for the next expansion process. The visited vertex, however, is stored in a list called a closed list, which includes all of the vertices that have already been visited/expanded. This list is generated to prevent the revisiting of expanded vertices.

Heuristics: In graph-based algorithms, to enhance the speed of convergence, various vertex-expansion methods have been proposed. In this regard, the main idea is that the algorithm needs to skip visiting unpromising vertices and expand those that have more potential to be part of the optimal path. In the hybrid A* algorithm, heuristics are utilized to promote quick conversion and as a criterion for choosing the next vertex to expand. Heuristics primarily provide an estimated cost of moving from the current location to the target location. It is notable that the condition of optimality necessitates that the intended heuristic to be admissible, meaning that the cost estimated by the heuristic is necessarily the lowest cost from that location to the target location. Some of the most-common heuristic estimates are the Euclidean norm of two points, Dubins curves, and Reeds Shepp curves.

5.3.2 Hybrid A* search:

Needless to say, planning a trajectory for an agent with non-holonomic constraints like a vehicle might lead to an infeasible trajectory. Therefore, the A* algorithm is not suitable for this type of agents as the direction change of the resulting trajectory is not smooth [86]. Regardless of the fundamental similarities of the hybrid A* and A* algorithms, in the former, the agent can be transformed between cells in a continuous manner rather than discrete, although the grid cell is still exploited to prevent the uncontrolled growth of the graph as explained later in this chapter. When the hybrid A* algorithm is switched on, open and closed lists are defined as empty, expansion starts from the initial state of the agent, and the new vertices are generated and added to the open list. Next, from the open list, a vertex/configuration with the minimum cost is selected and expanded. This loop continues until the termination condition is met. The vertex/configuration cost, $f_c(x)$, is the summation of cost-to-come (heuristic), $h(x)$, and cost-so-far, $g(x)$, Equation

5.11. If x is the current state and x' is the next state by taking action u, cost-so-far for the vertex belonging to x' is obtained by Equation 5.12, where $g(x)$ and $g_u(x, u)$ are the cost-so-far of the current state and the cost of state transition from x to x' by taking action u, respectively.

$$f_c(x') = g(x') + h(x') \tag{5.11}$$

$$g(x') = g(x) + g_u(x, u) \tag{5.12}$$

5.4 Potential Field

Generally, a potential field algorithm exploits artificial potential fields generated by immediate hazards such as obstacles, and the goal is to keep the agent away from the hazard while moving toward the goal. The potential field of the obstacles is repulsive, and its strength might vary based on the priority of the obstacles or other design purposes.

In the proposed motion planning, the hybrid A* algorithm plans a collision-free path for the vehicle as a result of the planner having excluded those cells that are occupied by the obstacles. However, the potential field is employed to fulfill two objectives in addition to the path planning approach. First, since the hybrid A* algorithm finds the shortest path between the current and the target locations, the generated path might let the vehicle approach the obstacles and road bounds dangerously, which is clearly not acceptable. However, the potential field allows the trajectory planner to exploit those collision-free areas in emergencies to avoid accidents. The second objective is to reduce the risk of accident owing to the uncertain behavior of immediate dynamic obstacles surrounding the vehicle, along with errors in the estimation of different variables, such as the vehicle speed and obstacle state.

In this thesis, two different potential fields are constructed: non-crossable obstacles and road curbs. The corresponding function for each of these potential fields is presented in the following.

5.4.1 Non-Crossable Obstacle

Non-crossable obstacles are those that the vehicle is not allowed to cross over, such as pedestrians or cars. As mentioned, the potential field is integrated with the hybrid A*

algorithm to provide a safe distance during non-emergency maneuvers. Therefore, three different areas around a non-crossable obstacle are defined, including behind, side, and front as in Figure 5.5. At each side, the potential of the field regulates a safe distance between the vehicle and the obstacle at each side.

The object detection and identification module, using a bounding box, defines every object i around the vehicle, and provides the object's width w_b^i, length l_b^i, and height h_b^i as well as its centroid location (x^i,y^i) with respect to the road coordinate at its centroid location. The velocity of the object v_x^i is only provided in the direction the obstacle is moving (assuming a longitudinal axis), and the yaw angle of the object ψ^i, reported by the module, is the angle of its longitudinal direction with respect to the centerline. Since, accurately measuring the lateral velocity of other vehicles is difficult, it is assumed to be zero.

As the vehicle is assumed to be a particle, i.e., its size is neglected, to prevent collisions, the modified width w^i and length l^i of each bounding box are used to construct the object's potential field (PF) and obstacle configuration rather than the actual ones, as in Equations (5.13) and (5.14). In these equations, w_e, l_e^f, and l_r^e can be calculated using Equations (5.15) and (5.16), where l_e^f, w_v, w_t, l_v^r, and l_t^r are the distance between the front end of the ego vehicle and its CG location, the ego vehicle width, the trailer width, the distance between the rear end of the ego vehicle to the CG location, and the distance between the rear end of the trailer to the CG location of the ego vehicle when the hitch angle is zero, respectively (see Figure 5.6). If the obstacle located on the lane has a high rank in the obstacle priority order, such as a vehicle and pedestrian, the vehicle is not allowed to pass by it using the same lane. This constraint can be simply implemented by replacing the width of the modified bounding box with the road lane width. Otherwise, for example, if the obstacle is a small rock and there is enough lateral space for the vehicle to pass, the modified bounding box is considered.

$$w^i = w_b^i + w_e \tag{5.13}$$

$$l^i = l_b^i + l_e^f + l_e^r \tag{5.14}$$

$$w_e = max(w_v, w_t) \tag{5.15}$$

$$l_e^r = max(l_v^r, l_t^r) \tag{5.16}$$

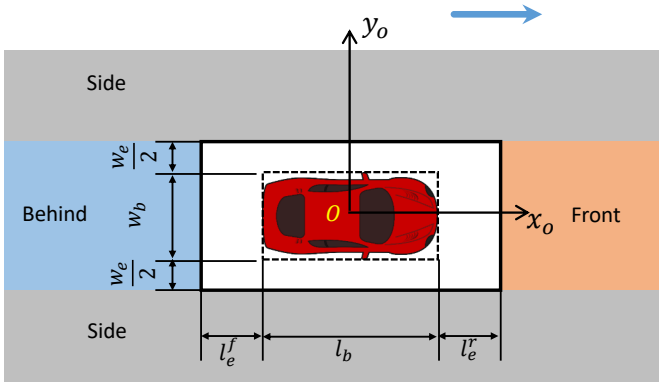

Figure 5.5: Defined areas around non-crossable obstacle

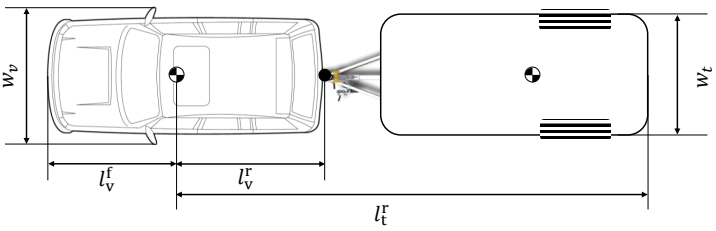

Figure 5.6: Ego vehicle with trailer

The PF of a non-crossable obstacle is generated by Equation (5.17) using the modified bounding box, where a_i^j is the intensity parameter of the potential field, b_i^j and c_i^j are its shape parameters, and $j = b, s, f$ denotes the behind, side, and front of the obstacle i. The PF needs to be adjusted based on the velocity of the ego vehicle u_v, its relative velocity with respect to the obstacle Δu^i, and the normal acceleration a_n needed to provide a suitable safe distance [53]. Therefore, the distance between the ego vehicle and the obstacles is normalized in x and y directions using x_n^i and y_n^i expressed by Equations (5.18) and (5.19), in which ψ^i is the heading angle of the obstacle with respect to the centerline. T_0 is the safe time gap, defined based on the ego vehicle response time.

$$\begin{cases} U_{nc}^i = a_i^j, & \text{(x,y) inside the modified box} \\ U_{nc}^i = \dfrac{a_i^j}{e^{\left(c_i^j || \frac{x-x^i}{x_n}, \frac{y-y^i}{y_n} ||_2^{b_i^j}\right)}}, & \text{otherwise} \end{cases} \tag{5.17}$$

$$x_n^i = x_0 + u_v T_0 + \frac{(\Delta u^i cos(\psi^i))^2}{2a_n} \tag{5.18}$$

$$y_n^i = y_0 + u_v T_0 + \frac{(\Delta u^i sin(\psi^i))^2}{2a_n} \tag{5.19}$$

As an example, Figure 5.7 shows the potential field of an obstacle moving at the same speed as the vehicle at 50 kph with a zero heading angle with respect to the centerline, and its modified bounding box is 4 meters wide and 4 meters long and is located at $(x^i, y^i) = (20, 0)$.

5.4.2 Road Curb

Although the ego vehicle is expected to safely deviate from the centerline of its current lane or even change its lane to avoid possible collisions, the vehicle is not allowed to become dangerously close to the road curbs in normal driving scenarios or leave the road boundaries in emergencies. Since the area beyond the road curbs is considered to be part of the obstacle configuration, the generated path certainly does not violate the road curbs. However, to have a safe distance from the road curb during maneuvers, a potential field for road curbs is specified. In addition, if the decision making layer is intended to prevent the ego vehicle from crossing specific road lanes, those lanes can also be treated as road curbs. The function of this potential field is as follows

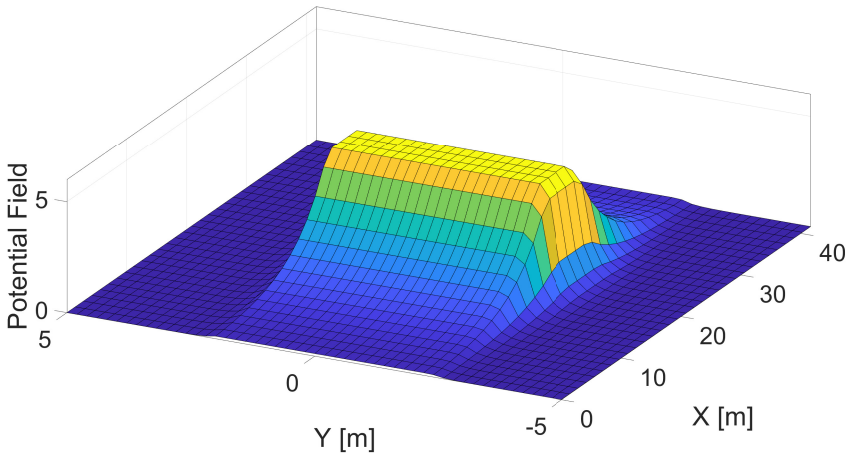

Figure 5.7: Potential field of a non-crossable obstacle

$$\begin{cases} U_{rc} = a_{rc} e^{c_{rc}(y-y_{rc})^{b_{rc}}}, & \text{left curb} \\ U_{rc} = a_{rc} e^{-c_{rc}(y-y_{rc})^{b_{rc}}}, & \text{right curb} \end{cases} \tag{5.20}$$

where y_{rc} is the lateral position of the road curb (considering the ego vehicle width w_e) with respect to the center line of the current lane. Figure 5.8 shows the PF of the road curb, where the road curbs are parallel to the straight centerline at $\pm 6m$ distance.

5.5 The Proposed Motion Planning

As mentioned, the proposed motion planning is based on the hybrid A* algorithm, which generates the shortest path from the current location to the target location. Although this shortest path never passes the obstacle configuration space, i.e., it is collision-free, it might violate the safe distance from obstacles in normal driving due to path tracking error and inaccurate estimation of the size, position, and velocity of an obstacle. Therefore, the potential field approach is integrated with hybrid A* to rectify safety concerns as explained in the following.

The motion planning algorithm receives information about the obstacles, the road, the ego vehicle from the perception module. Since the locations of the obstacles and road curbs received from the perception module are in the ego vehicle coordinates, they are

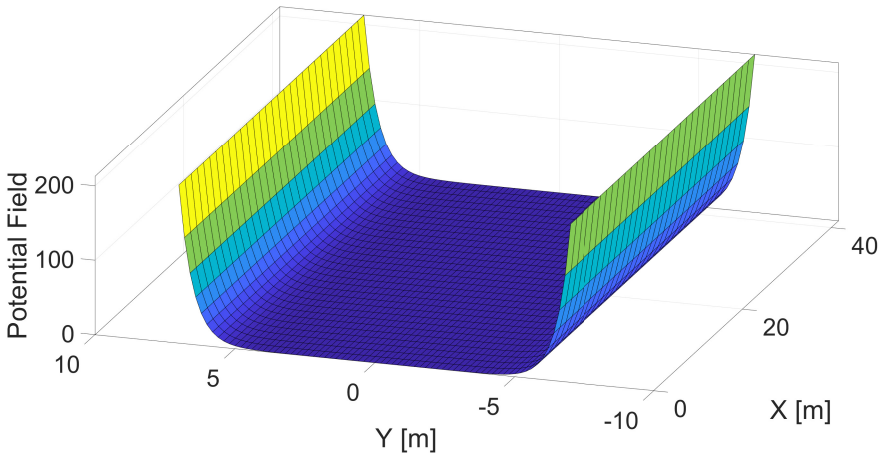

Figure 5.8: Potential field of road curbs

transformed to (s,y) coordinates (s being defined along the centerline) at their locations as Figure 5.9 shows.

Next, the configuration space (road space) is discretized. The overall potential of each cell corner is calculated using the introduced potential field functions. If a corner is powered by different potential fields due to different obstacles or road curbs, the maximum value of those potential fields in that corner is chosen. The size of each cell is also an important parameter to choose and depends on obstacle size and the fidelity of the sensor information [76]. On the one hand, fine discretization increases computation time as the number of cells increases. On the other hand, coarse size underestimates collision-free configuration space and makes the planning conservative, possibly leaving the algorithm without a solution. Here, the width of the cell is set $c_w = 0.25$ m and the length of the cell is expressed by $c_l = u_v^x T$, where T is the time step. As known, each configuration is characterized by $q = [x \quad y \quad \psi]^T$.

At this stage, hybrid A* starts expansion from the current location of the ego vehicle by taking all of the actions in the action space $U(x)$. In the proposed hybrid A* algorithm, control action is a set of steady-state variables rather than an actual control action like steering as a common method. At high speed, applying the maximum steering angle is not practically possible due to stability concerns. However, the proposed approach can be used since the control actions can be defined based on the stability envelope, although the transient behavior is ignored. This approach is also computationally efficient, as it does not need to use a dynamic model to ensure the feasibility of the proposed trajectory.

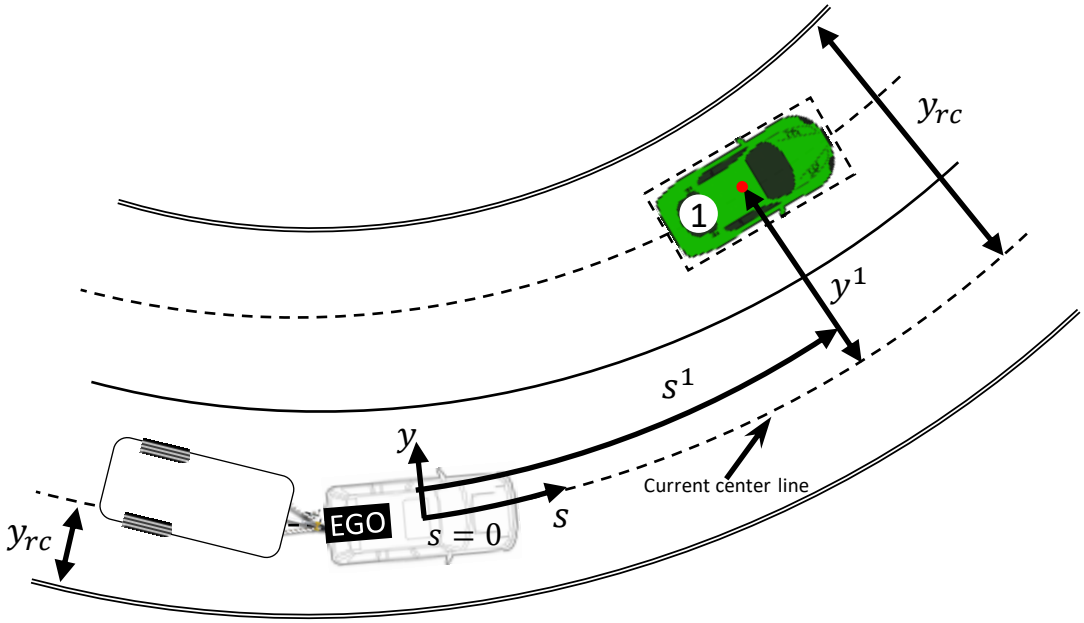

Figure 5.9: Obstacles in (s,y) coordinates

Assuming the vehicle speed is constant over the planning horizon, each vehicle has two state variables that predict its position in the future in the X-Y coordinates: the yaw rate and lateral velocity (or the sideslip angle). At each vertex, the algorithm takes all the control actions from the control action space $U = [-u, 0, u]$, where $u = [r^u_{max}, \beta^u_{max}]^T$, to expand new vertices. Basically, r^u_{max} and β^u_{max} are obtained from the equilibrium at the stability limit. r^u_{max} is available from the stability envelope defined in Section 3.3, but β^u_{max} can be defined using the steady-state gains of a single-vehicle that are defined as follows

$$r^{ss} = \frac{u^x}{(l_1 + l_2) + k_{us}(u^x_v)^2}\delta_1 \tag{5.21}$$

$$\beta^u_{max} = \frac{l_2 + \frac{ml_1}{(l_1+l_2)C_{\alpha 2}}(u^x_v)^2}{(l_1 + l_2) + k_{us}(u^x_v)^2}\delta_1 \tag{5.22}$$

where k_{us} is the under-steer coefficient of the vehicle. Using Equations (5.21) and (5.22), β^u_{max} can be expressed as follows

$$\beta^u_{max} = \frac{l_2 + \frac{ml_1}{(l_1+l_2)C_{\alpha 2}}(u^x_v)^2}{u^x_v} r^u_{max} \tag{5.23}$$

It is notable that β^u_{max} should not exceed the stability limit defined in the stability envelope. To prevent any sudden jumps in the generated path, an additional cost is aslo added to the cost-so-far if the predecessor's action is -u and the chosen control action for the successor is u, and vice versa.

The configuration of a vertex (successor), $q_s = [x_s \quad y_s \quad \psi_s]^T$, newly generated by taking the aforementioned control actions can be obtained using the kinematic relationships as follows:

$$\psi_s = r^u T + \psi_p \tag{5.24}$$

$$x_s = x_p + (u^x_v \cos\psi_s - \beta^u u^x_v \sin\psi_s)T \tag{5.25}$$

$$y_s = y_p + (u^x_v \sin\psi_s + \beta^u u^x_v \cos\psi_s)T \tag{5.26}$$

where x_p, y_p, and ψ_p are the configuration of the predecessor (the vertex that was expanded). The configuration of each successor is stored for further expansion. The successors and the predecessor are added to the open list and the closed list, respectively.

As the algorithm proceeds, during the expansion, the successors can be inspected for different criteria. If a successor does not pass the defined measures, it is discarded. In this research, failure to pass happens if a successor falls into one of the following four categories.

1. A successor goes into the obstacle configuration space: This condition guarantees that the generated path is collision-free.

2. The successor passes over the stability envelope: The stability envelope is implemented in the trajectory tracking controller to keep the vehicle stable: However, if the generated path does not consider the stability limitations, the vehicle deviates from the path so as not to violate stability bounds, which is inappropriate. To guarantee that the vehicle remains stable while following the generated path, the successor is ignored if the vehicle exceeds the comfort/stability envelope in that node (these envelopes are explained below). This is the second inspection, and Figure 5.10 demonstrates this process in a green dashed branch.

3. The trailer enters the obstacle configuration space: The third inspection is performed to ensure that the trailer does not violate the obstacle configuration space. To do so, having the state of the ego vehicle, the rear end location of the trailer is estimated. If this location is inside the prohibited space, the successor is skipped.

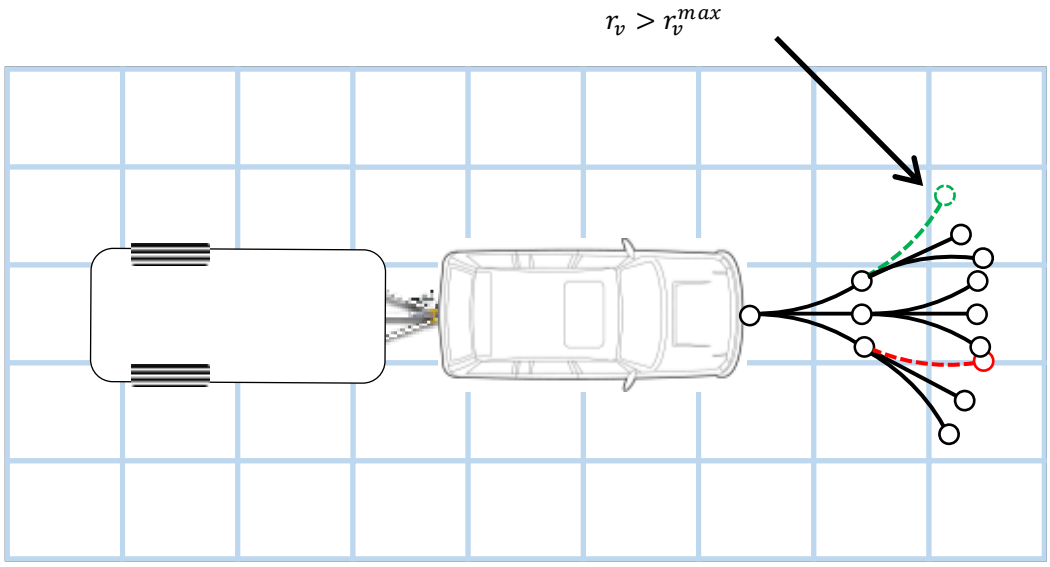

Figure 5.10: Expansion and pruning

4. The cost of maintaining the successor may not be justified: The last inspection is executed to prevent the unnecessary growth of vertices: This process is called branch pruning [76]. If a successor falls into a cell that has not been visited yet, the successor is added to the open list. However, if there is a previously-generated vertex in that cell and it is on the closed list, or that previously-generated vertex is on the open list but its cost-so-far is lower than that of the newly generated one, the successor is discarded, shown as a red dashed branch, Figure 5.10.

As discussed, some proceedings are included in the motion planning algorithm to generate a path that addresses stability concerns. However, since the generated path is the shortest one between the current and the target locations, and the maximum increment capacity of the control action is utilized at each expansion, the lateral acceleration of the ego vehicle during a maneuver might rise to a level that is uncomfortable for the passengers under normal driving conditions. To deal with this problem, the control action and the stability envelope are scaled down by a factor λ_c, $0 < \lambda_c \leq 1$, expressed by Equation (5.27) in which a^y_{cmf} represents comfortable lateral acceleration, considered as a hype-parameter, and a^y_{max} is the maximum lateral acceleration (see Figure 5.11).

$$\lambda_c = \frac{a^y_{cmf}}{a^y_{max}}, \quad a^y_{max} = r_v^{max} u_v^x \tag{5.27}$$

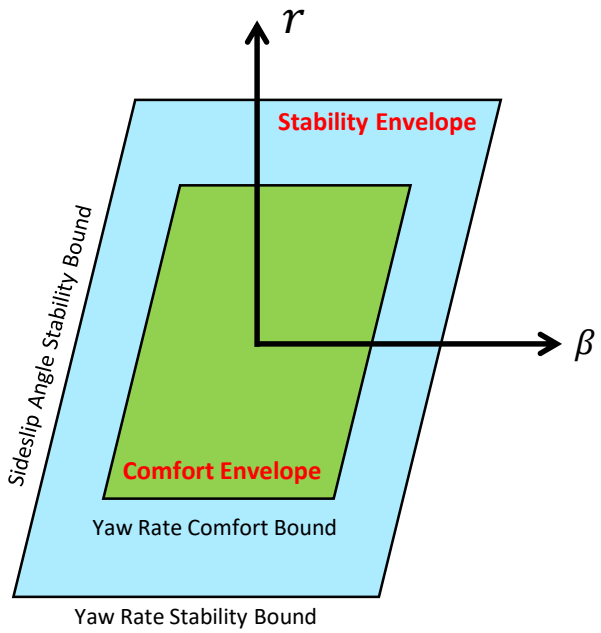

Figure 5.11: Stability and comfortable envelopes

As explained, in general, the cost of each configuration, $f_c(x')$, is the summation of the cost-so-far, $g(x')$, and the cost-to-come (heuristic), $h(x')$. In the proposed motion planning, the cost-so-far of each successor x', $g(x')$, is obtained by Equation (5.28) in which $g(x)$ is the cost-so-far of the predecessor, $g_u(x, u)$ is the cost of taking action u at the state x that is the Euclidean distance between the successor and the predecessor, and $g_{pf}(x')$ is the potential of that vertex being in that cell, resulting from the interpolation of the potential field of the cell corners. To consider the effect of the trailer, $g_{pf}(x')_{re}$ is added to the cost-so-far formula, and represents the potential field of the trailer rear end. If the trailer becomes close to the obstacles or road curb, the cost-so-far of the expanded vertex increases, and the successor will probably not be part of the path. The position of the trailer with respect to the vehicle is explained in [50]. The heuristic that is used in this motion planning approach is the Euclidean distance.

$$g(x') = g(x) + g_u(x, u) + g_{pf}(x') + g_{pf}(x'_{re}) \tag{5.28}$$

Normally, the goal/target location for the motion planning module is set by the behavioral planning module, and the hybrid A* algorithm terminates when it reaches this location, or is reasonably close to it. In normal driving, the target location (green circles

in Figure 5.12) is set laterally on the centerline of the target lane and longitudinally at the prediction horizon of the motion planner. However, this point might not be reachable if an obstacle blocks the lane. In such a scenario, the algorithm defines a local terminal behind each obstacle, in addition to the goal location, thus avoiding infeasibility, as Figure 5.12 illustrates. Thus, the algorithm terminates if the vertex is reasonably close to the goal location or a local terminal.

If there is no behavioral planning module to set the goal location, or the behavioral planning module is not able to provide the best goal location, the algorithm is able to consider several goal locations and find the one that will cost the least to reach. In this situation, during expansion, a separate heuristic is determined for each goal at each vertex, and the minimum heuristic is chosen. As a result, the cost-to-come, $h(x)$, and accordingly $f_c(x)$, are calculated.

These local terminals can also be exploited for crash mitigation. As mentioned, the algorithm selects the vertex with the lowest cost from the open list each time in the expansion process and terminates when the vertex is near the goal location or local terminals. Crash mitigation is important where collision is inevitable, meaning that the goal location is not reachable due to the presence of obstacles. Therefore, the vehicle converges to one of the local terminals with minimum cost, providing an opportunity for generating a path to mitigate the cash cost as much as possible. To this aim, the cost of a local terminal located at a distance d_t from the ego vehicle can be adjusted based on the obstacle priority cost g_p and the proximity cost of the ego vehicle to the corresponding obstacle g_{pr}, as follows

$$g_{ter}(x_t) = g_p(x_t) + g_{pr}(x_t) \tag{5.29}$$

$$\begin{cases} g_{pr} = \frac{a_{pr}}{e^{-c_{pr}|d_t - d_{sd}|^{b_{pr}}}}, & d_t - d_{sd} < 0 \\ g_{pr} = 0, & otherwise \end{cases} \tag{5.30}$$

where a_{pr}, b_{pr}, and c_{pr} are the tuning parameters, and d_{sd} is the estimated stopping distance, which can be defined as

$$d_{sd} = \frac{(u_v^x)^2}{2a_{max}^x} + u_v^x T_0 \tag{5.31}$$

In this thesis, to smooth the path generated by the hybrid A* algorithm, a 6^{th}-order polynomial is fitted on the path, with the current and target locations and their heading angles weighted heavily to be on the polynomial.

After the path has been generated, the target speed profile over the path needs to be defined, optimally by the MPC controller. In the proposed motion planning module,

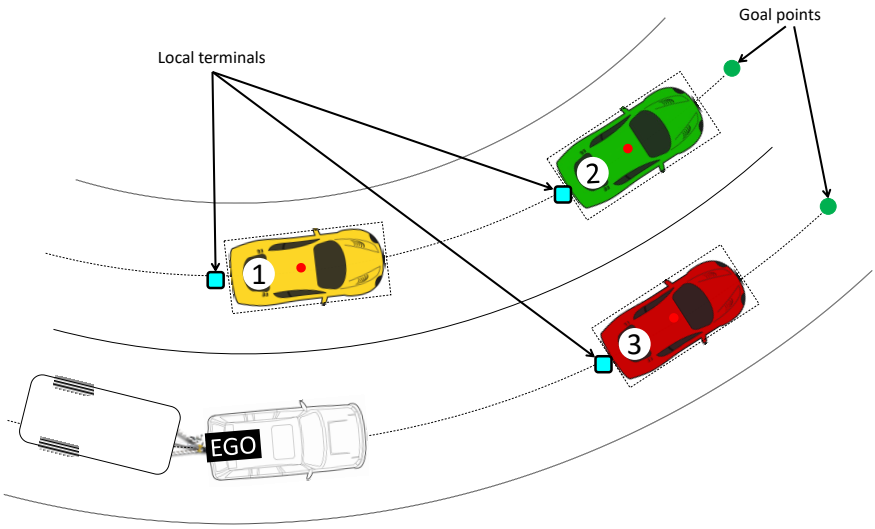

Figure 5.12: Possible goal/target locations and local terminals

the maximum allowable speed is implemented as an upper bound constraint for the state variable u_v^x in the MPC formulation; therefore, the optimization solution provides the optimal longitudinal acceleration required to adjust the speed. The maximum allowable speed is expressed as follows:

$$u_{max}^x = min(u_{max}^r, u_{max}^k) \tag{5.32}$$

where u_{max}^r is the maximum speed imposed by the road regulation and u_{max}^k is the maximum speed based on the maximum allowable lateral acceleration. In a cornering maneuver, the maximum speed can be defined as

$$u_{max}^k = \sqrt{\frac{\lambda_c a_{max}^y}{k_{max}}} \tag{5.33}$$

where k_{max} is the maximum curvature of the path over the motion planning horizon. Additionally, the ego vehicle needs to adjust the speed so that a safe distance with respect to the front vehicle is maintained. To do so, an upper bound on the state variable s is imposed.

5.6 Simulation Results

In this section, computer simulations are conducted to assess the performance of the proposed motion planning module and the MPC-based trajectory tracking controller developed in Section 5.5 and Section 5.1 for different scenarios. Both modules are implemented in MATLAB, and the same CarSim model introduced in Section 4.3 is used to represent the vehicle dynamics.

Although the steering angle is directly applied to the vehicle, the control action for longitudinal direction, longitudinal acceleration a_x, is transformed into longitudinal force as multiplied by the total mass of the vehicle and the trailer. Then, this force is distributed among the wheels proportionate to their normal load (considering the lateral load transfer) and applied by four electric motors. Although the tire capacity is considered as a constraint in this controller formulation, a slip controller is designed to prevent large slip ratios.

To show the performance of the aforementioned modules, different scenarios are defined as:

- Merging, a normal driving scenario
- Sharp turn, off-tracking problem
- Lane change, a pop-up obstacle
- Crash mitigation, obstacle prioritization

During these maneuvers, at each time step, the obstacle data is received and the discretized potential field is generated. The location of the obstacles is predicted with the assumption that each obstacle keeps its speed and the moving direction over the motion planning horizon, which is set to be 3 s with a time step of 100 ms. Having the potential field, free configuration space, and the available control actions, the motion planning module generates the trajectory. Next, the proposed controller uses the current state of the vehicle, and the generated path defined as the target path formulates the performance index as a quadratic function with a 2 s prediction horizon and 100 ms time step. It is important to note that only the first 2 s of the generated path are considered for the performance index formulation. This function is computed by a quadratic programming solver qpOASES [119] with respect to the stability envelope, environmental, and control action constraints in order to produce steering angle and throttle/brake commands. These commands are applied to the CarSim model to receive the new state of the vehicle in the environment for the next time step.

5.6.1 Merging, a normal driving scenario

Merging and lane keeping are two normal driving scenarios that frequently happen on roads. To show the performance of the vehicle in both maneuvers, Scenario 1 has been designed. In it, the current lane of the ego vehicle ends, and since the left lane is occupied with other vehicles, the ego vehicle needs to slow down and change the lanes when it is safe. There are two obstacles on the left lane moving at a constant speed of 70 kph, and spaced 50 m apart, the initial longitudinal distance between the ego vehicle and the closer obstacle is 50 m. At the beginning of this scenario, the behavioral planner does not allow the ego vehicle to change its lane due to safety concerns; as a result, the vehicle has to slow down and wait for a lane change command. In this situation, there is only one goal point on the current lane, at the horizon since the vehicle is not allowed to use the other lane. However, as mentioned, if the goal point exceeds the road boundary or passes an obstacle, a local terminal is added to prevent infeasibility as Figure 5.13 shows.

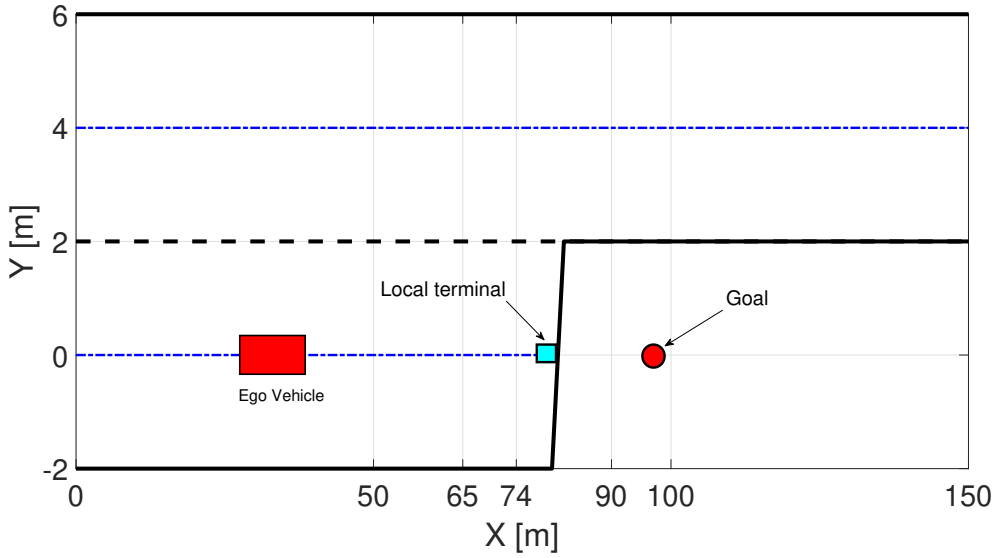

Figure 5.13: Goal and local terminal in normal driving scenario

Figures 5.14 and 5.15 illustrate the result of this maneuver, and indicate the path of the ego vehicle, control commands, the velocity and accelerations, stability envelope, and hitch angle. To demonstrates the position of each object with respect to the road in Figure 5.14, each object is given a different shape (the rectangle is the ego vehicle) and, at some sample times, different colors are used. In this plot, the vehicle is shown to smoothly and

safely merges into the left lane and follows it.

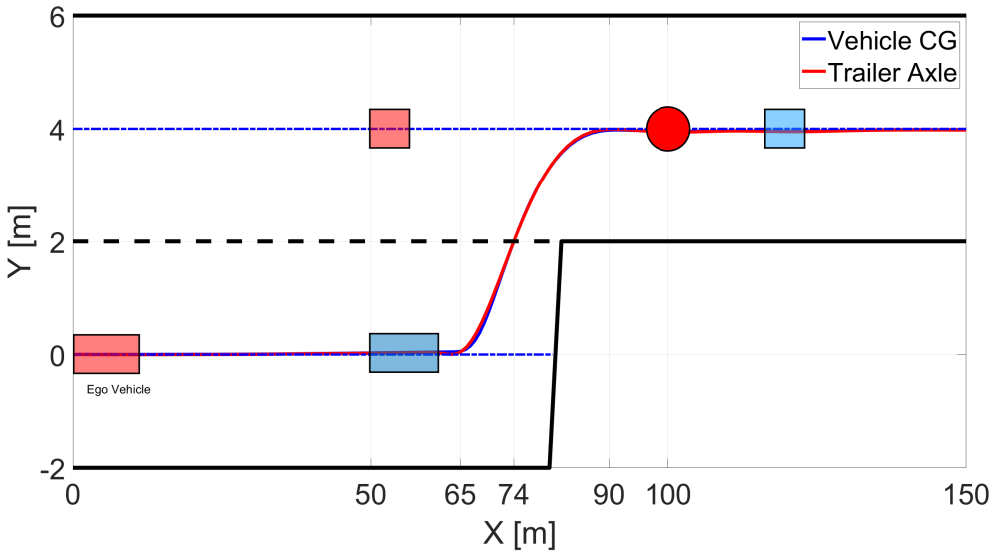

Figure 5.14: Path of the ego vehicle in the normal driving scenario

As Figure 5.15-a suggests, in this maneuver, at $t = 1.1s$, the ego vehicle realizes that the lane ends and accordingly starts to brake, reducing its speed for 2 s so as not to violate the road bound. Then, after receiving the lane change command at $t = 4.1s$, when the left lane is safe, the vehicle begins to merge into that new lane and simultaneously speeds up through positive acceleration. As the vehicle becomes close to the maximum speed, which is set to 70 kph, the acceleration reduces not to exceed the speed limit. In this plot, it is shown that both the requested steering angle and longitudinal acceleration are smooth, and the actual acceleration follows the control command effectively. As a result, the longitudinal velocity, lateral acceleration, and yaw rate are smooth as well, see Figure 5.15-b.

Since it is a normal driving scenario, the parameter λ_c is set at 0.5 and, as can be seen in the figure, and the lateral acceleration of the vehicle is below its limit (0.45g). The yaw rate and lateral slip angle of the second axle are also considerably below the defined stability bounds, Figures 5.15-c and 5.15-d, and the hitch angle remains small, Figure 5.15-e.

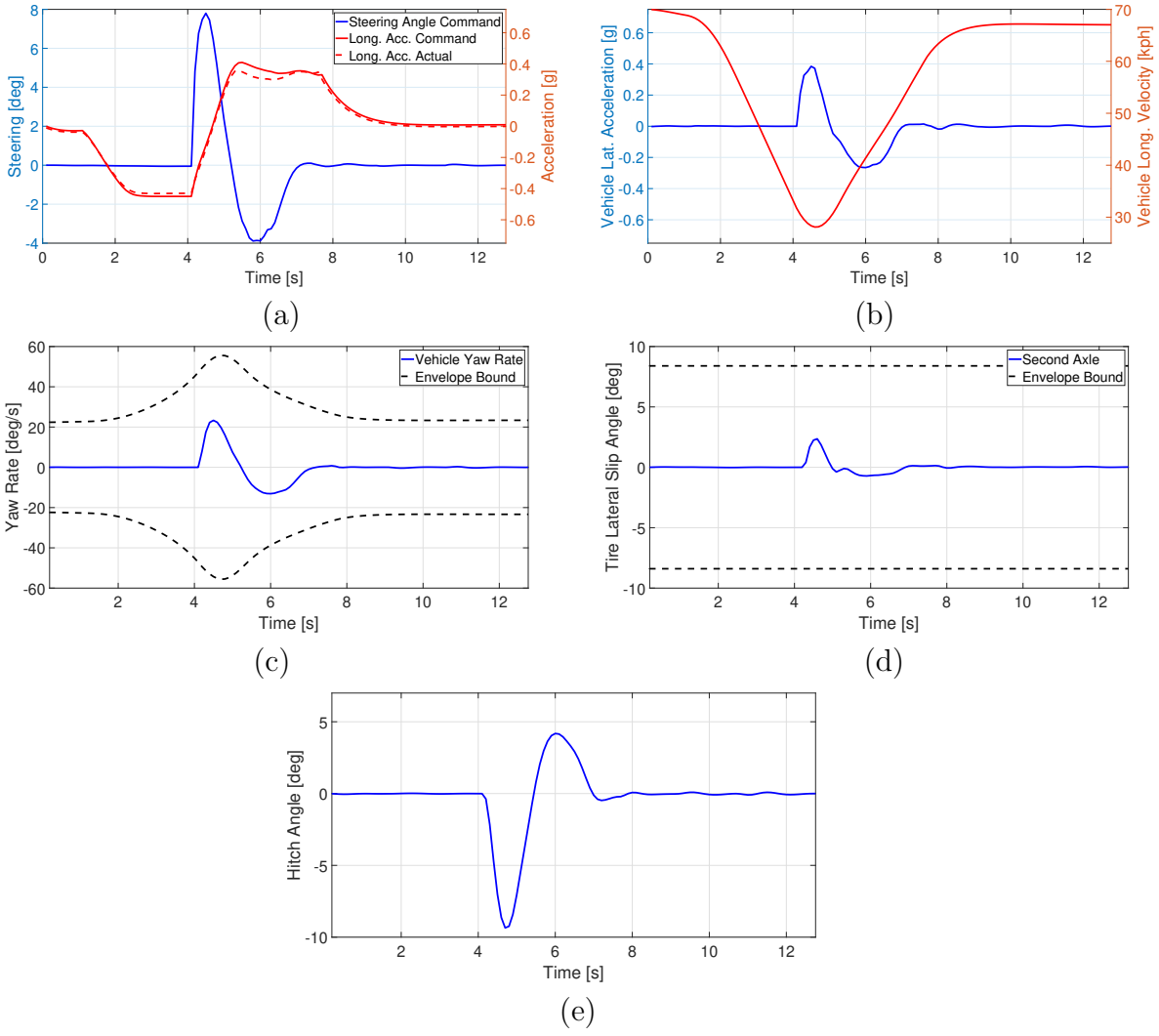

Figure 5.15: Simulation results in the normal driving scenario

5.6.2 Sharp turn, off-tracking problem

As mentioned, generally, vehicle-trailer systems suffer from the off-tracking problem, i.e., the rear end of the trailer does not follow the path generated by the vehicle front end, causing a large swept width. For example, in high curvature roads such as sharp intersections or roundabouts, the trailer might violate the road bounds. In an obstacle avoidance situation, the trailer might also collide with the obstacles although the vehicle unit passes them safely. To address this problem, in the proposed motion planning, the effect of the trailer movement is considered as explained in Section 5.5.

Scenario has been designed to show the performance of the proposed method. In it, the ego vehicle follows a centerline containing a 90-degree turn at a radius of 10 m. The initial speed of the vehicle and the lane width are set equal to 40 kph and 3.6 m, respectively, and a new trailer with a longer wheelbase (4.8 m) is attached to the vehicle. The other properties of the trailer remain the same.

As Figures 5.16 and 5.17-c show, where the trailer effect is considered, the vehicle deviates from the centerline to the right side in order to accommodate the trailer on the road and keep it near the center line. Since the lane and trailer widths are 3.6 m and 2 m, respectively, and the measured deviation of the trailer is 0.85 m, the trailer violates the road bound for 5 cm. Thus, those nodes in which the trailer violates the road bounds are not added to the open list. In addition, as the trailer approaches the bounds, the cost of the visited nodes, as explained in Section 5.5, increases, and as a consequence, those nodes have a lower chance to be selected as part of the target path.

From the control action point of view, where the trailer effect is on, at $t = 5.3s$, as the trailer enters the turn, the controller prevents larger steering angles, compared to where that effect is off, to provide a larger turning radius. To adjust the speed with respect to the curvature and the defined comfortable acceleration, see Equation (5.33), the controller starts to command negative acceleration before entering the turn. As explained, this adjustment is performed by changing the upper bound constraint of the velocity in the MPC formulation. When the vehicle passes the turn, it begins to accelerate gently to reach the maximum allowable speed of 40 kph, as Figure 5.17-a and 5.17-b present.

5.6.3 Lane change, a pop-up obstacle

The motion planning module and accordingly the controller module are expected to immediately and safely respond to situations that can cause serious damages to the ego vehicle

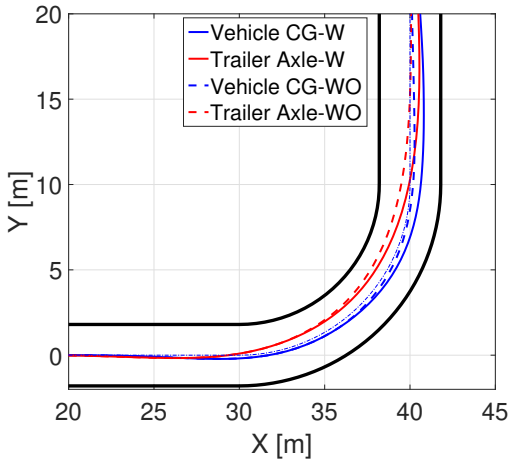

Figure 5.16: Path of ego vehicle in sharp turn with and without considering trailer effect

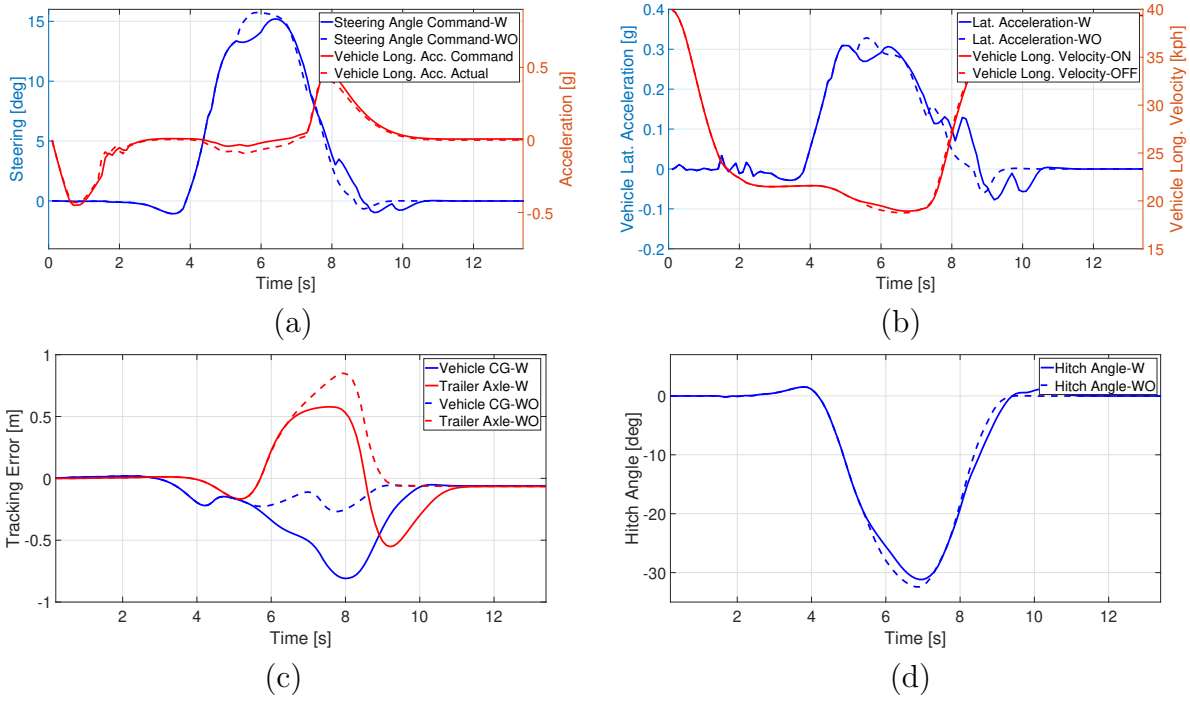

Figure 5.17: Simulation results in the normal driving scenario

or other objects on the road, all while keeping the vehicle stable. To assess the capability of the proposed approach in these situations, the third scenario is proposed, in which a pop-up obstacle appears on the current lane of the vehicle, while the left lane can be exploited for obstacle avoidance. The distance between the obstacle and the ego vehicle is shorter than the one estimated by time to collision; thus, the vehicle needs to change its lane to prevent a collision. In this scenario, the vehicle moves at a constant speed of 70 kph on a dry road ($\mu = 0.9$), and the obstacle appears at $X = 85m$, and $t = 3s$. The obstacle is assumed to be square-shaped, with the sides of 2 m, and the distance between the vehicle and the obstacle is 25 m when the obstacle pops up, whereas the estimated stopping distance is 29 m.

As Figure 5.18 shows, none of the paths generated by the vehicle and the trailer rear end intersect with the yellow area, which is the modified box of the obstacle explained in Section 5.4.1; i.e., there is no collision. It is important to note that the parameter λ_c is set to 1 due to the necessity of this emergency situation.

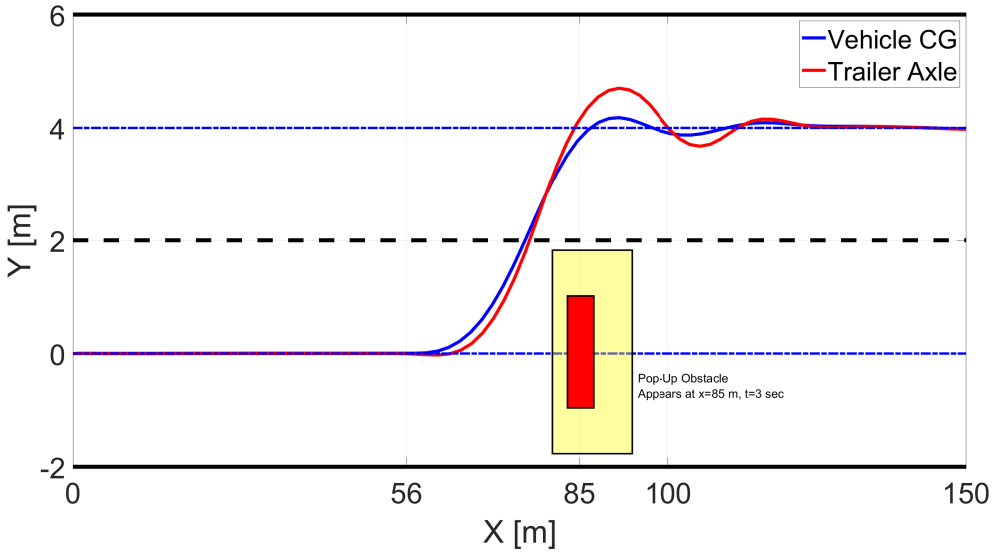

Figure 5.18: Path of ego vehicle in lane change scenario

During this maneuver, contrary to the lateral acceleration, which goes up to $0.6g$, the speed of the vehicle does not change much, because there is no obstacle ahead of the vehicle along the generated path to impose speed reduction for collision avoidance, and also the road curvature remains constant (see Figures 5.19-a and 5.19-b). After the maneuver, the controller begins to gradually increase the speed up to the maximum of 70 kph by

requesting positive acceleration.

In this maneuver, although the lateral slip angle of the second axle is notably below the stability bound (see Figure 5.19-d), the yaw rate of the vehicle is near its stability margin, which means that the vehicle comes close to its handling limit as Figure 5.19-c shows. The hitch angle remains small but demonstrates oscillatory behavior because this vehicle is prone to snaking instability, Figures 5.19-e and 5.18.

5.6.4 Crash mitigation, obstacle prioritization

As presented in the previous scenarios, the proposed motion planning has the ability to slow the vehicle or allow it to pass the obstacle on its side if it is not feasible to stop behind it. However, in some situations, a collision is inevitable and, as a result, choosing the lowest crash cost is an appropriate approach. With this in mind, Scenario 4 is defined to show the capability of the proposed motion planning module in prioritizing the obstacles among which the ego vehicle moves with a maximum speed of 70 kph on the first lane of a two-lane road. The road is dry ($\mu = 0.9$), and another vehicle in the second lane, driving at the constant speed of 40 kph, is initially 10 m ahead of the ego vehicle. Suddenly a pop-up obstacle appears on the lane at $X = 25$ as well. Depending on the type/position of the obstacle and its crash cost, three different situations can be determined. First, the obstacle, such as a rock, is small and its position allows the vehicle to pass by without crashing into the other vehicle. Second, the pop-up obstacle is a pedestrian, and thus has the highest priority in the collision-avoidance ranking. In the last situation, the pop-up obstacle, perhaps a box, has a lower crash cost than the vehicle. As explained, the crash cost of each obstacle is the summation of the time-to-collision-based cost function and the type of the obstacle, presented in Table 5.1. All goals are activated in crash mitigation scenarios, and the motion planner allows the hybrid A* algorithm to find the lowest cost path from the starting point to one of these goals or converge to the lowest-cost local terminal,i.e., the lowest crash cost path.

Table 5.1: Priority of the Obstacles and the corresponding cost

Obstacle	Priority Order	Priority Cost g_p
Pedestrian	1	100
Vehicle	2	20
Box	3	5

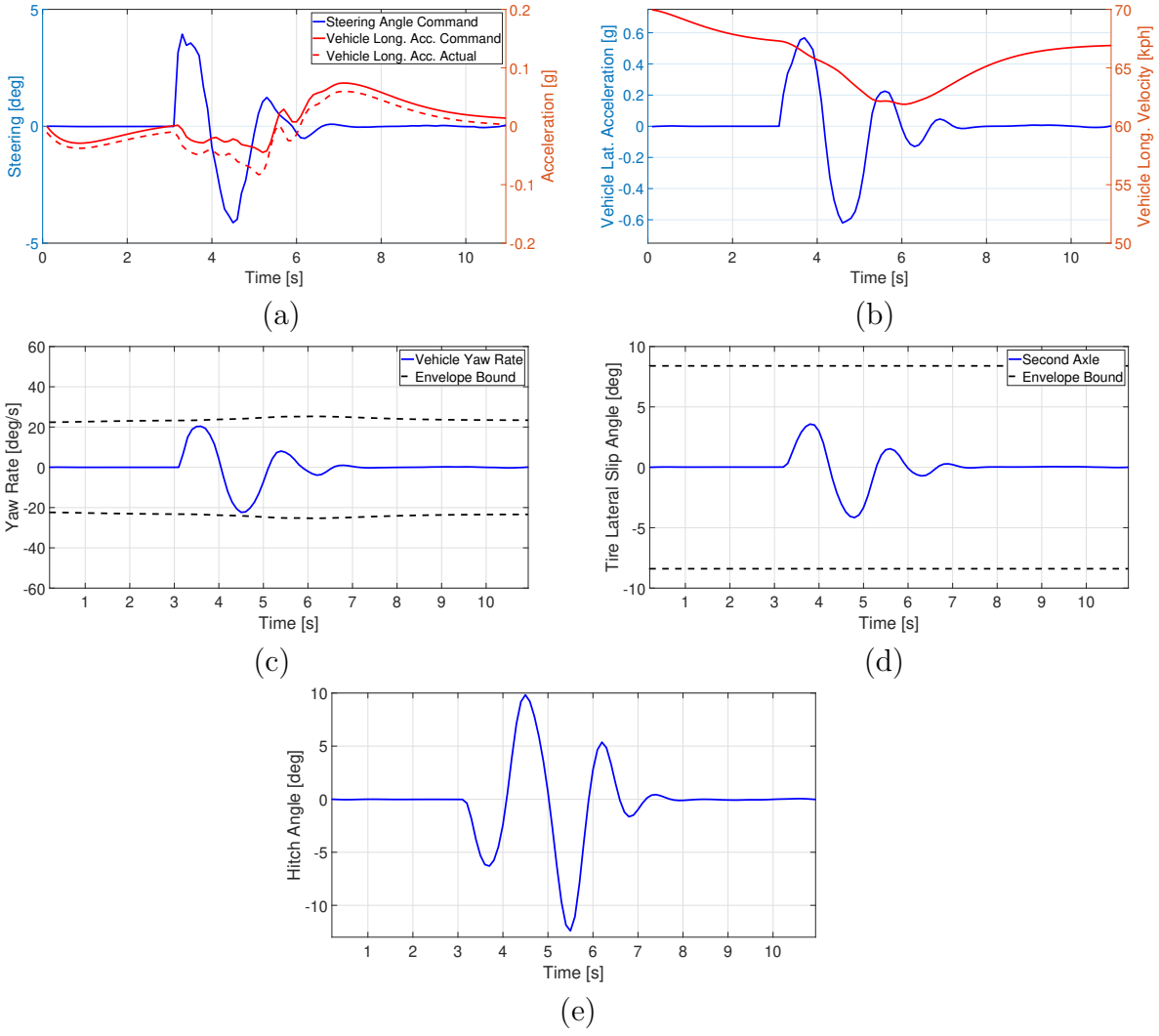

Figure 5.19: Simulation results in the lane change scenario

Figures 5.20- and 5.21 show the result of the first situation, in which a square-shaped obstacle with the sides of 1 m appears at $X = 25m$ and $Y = -1m$, as presented in Figure 5.20. In this situation, the ego vehicle is able to pass the obstacle without collision as the path of the vehicle, and its trailer's rear end, do not collide with the modified box of the obstacle (yellow area). During this maneuver, the vehicle speed is kept approximately constant, Figure 5.21-b, the yaw rate and the lateral slip angle of the second axle are considerably below the stability bounds, Figures 5.21-c and Figure 5.21-d, and the hitch angle remains small due to the small steering angle and low lateral acceleration, Figure 5.21-e.

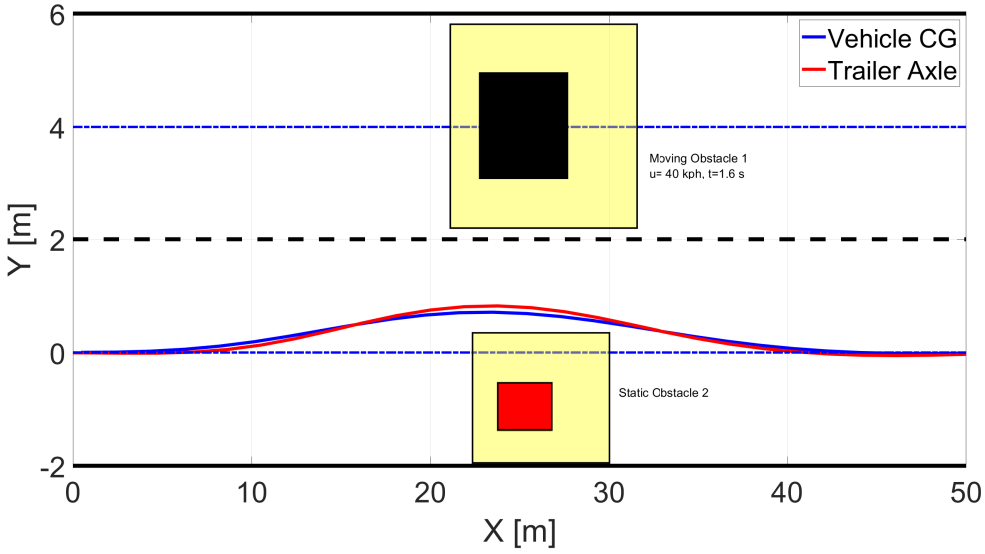

Figure 5.20: Path of ego vehicle in first crash mitigation scenario

Figure 5.22 shows how the hybrid A* algorithm searches the free configuration space to find a path from the start point to the goals or local terminals, at the first time step of the simulation. In this figure, the start point is the red square, the goals are magenta diamonds, local terminals are cyan squares, the red bullets are the nodes in the open list, and the black bullets are the nodes in the closed list. The maroon dashed line shows the output path of the hybrid A* algorithm; however, as explained, this path is smoothed by the defined polynomial, demonstrated by the solid blue line in the figure.

For the second situation, it is assumed that the pop-up obstacle is a pedestrian located in the middle of the first lane, and its bounding box is square-shaped with the sides of 1

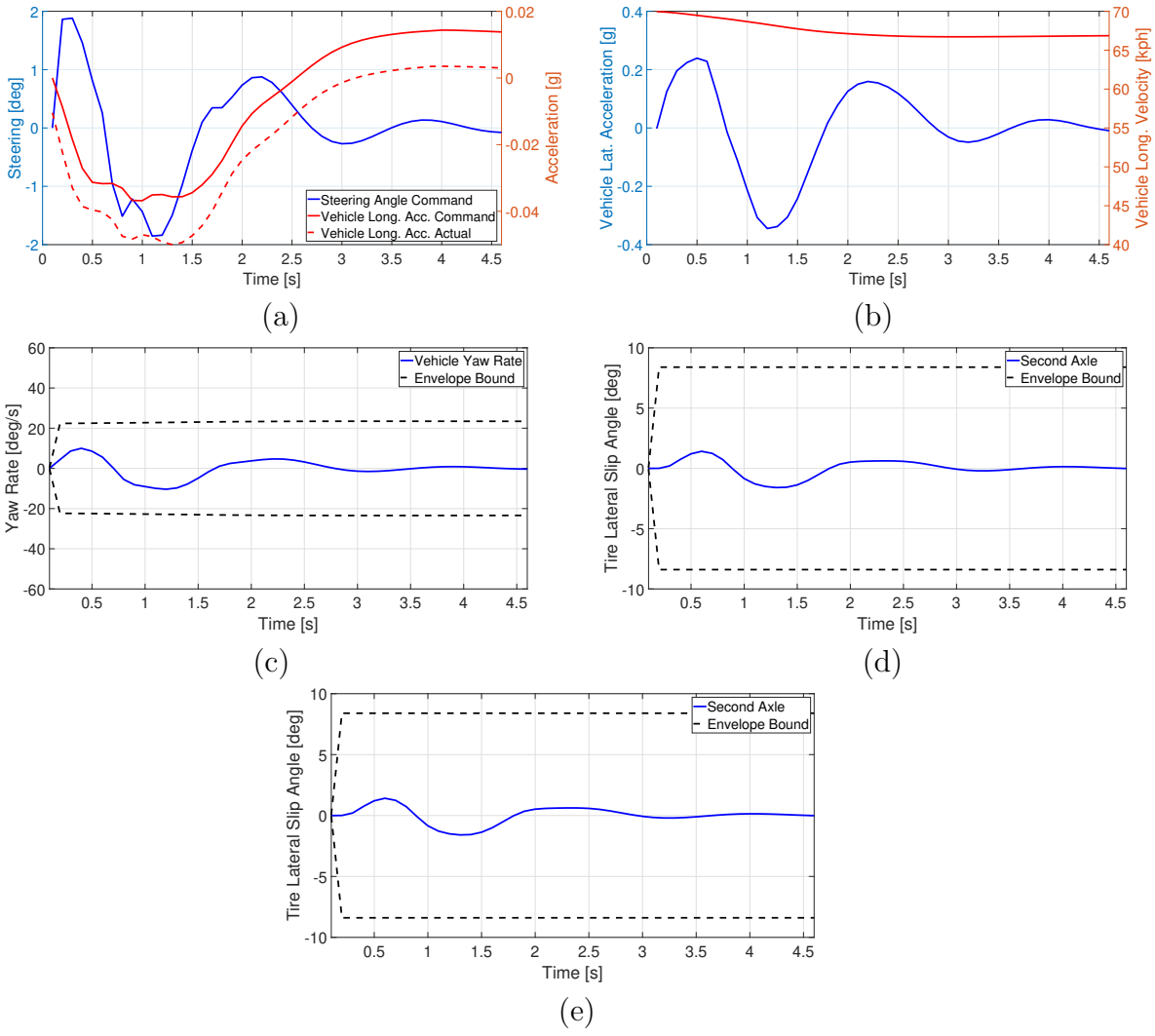

Figure 5.21: Simulation results in the obstacle prioritization scenario-passing

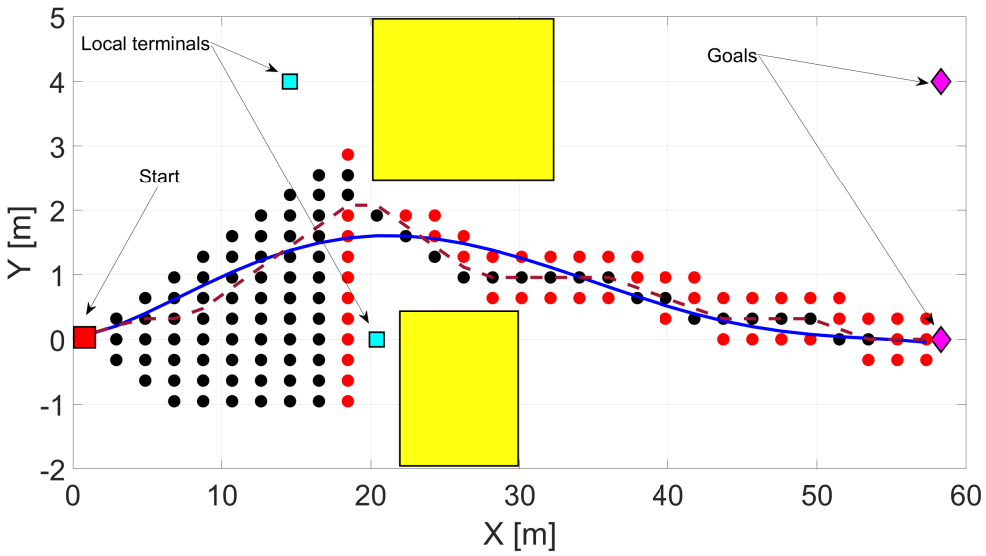

Figure 5.22: Hybrid A* algorithm search process at first time step in first crash mitigation scenario

m. Since avoiding the pedestrian has the highest priority, in order to prevent a collision, the motion planner generates a path to change the lane and keep the vehicle away from the pedestrian, although the ego vehicle crashes into the other vehicle in the second lane at $t = 1.6s$, see Figure 5.23.

As Figure 5.24-a shows, the actual longitudinal acceleration does not follow the commanded one, unlike in the previous scenarios. To explain this difference, it can be said that although the longitudinal acceleration is bounded according to the tire capacity, neglecting longitudinal load transfer and the existence of uncertainties/approximations in the tire and vehicle models can cause incorrect lateral or longitudinal force demand from the tires, especially in harsh maneuvers. However, as mentioned, to avoid these situations, a slip controller is implemented, which helps to keep the vehicle stable and prevent wheel lock.

At the beginning of this maneuver, to avoid the pedestrian, the controller applies about 8 degrees of steering angle in the first time step, Figure 5.24-a. This steering angle pushes the vehicle to leave the stability envelope from the yaw rate edge, as Figure 5.24-c shows. Thus, in the next step, the controller applies a counter-steering to bring the vehicle back within the envelope. The same process happens in the next couple of time steps due to these contradictory requirements. Moreover, in the lateral dynamic derivation presented in Section 3.2.1, it is assumed that the vehicle velocity remains constant over the horizon.

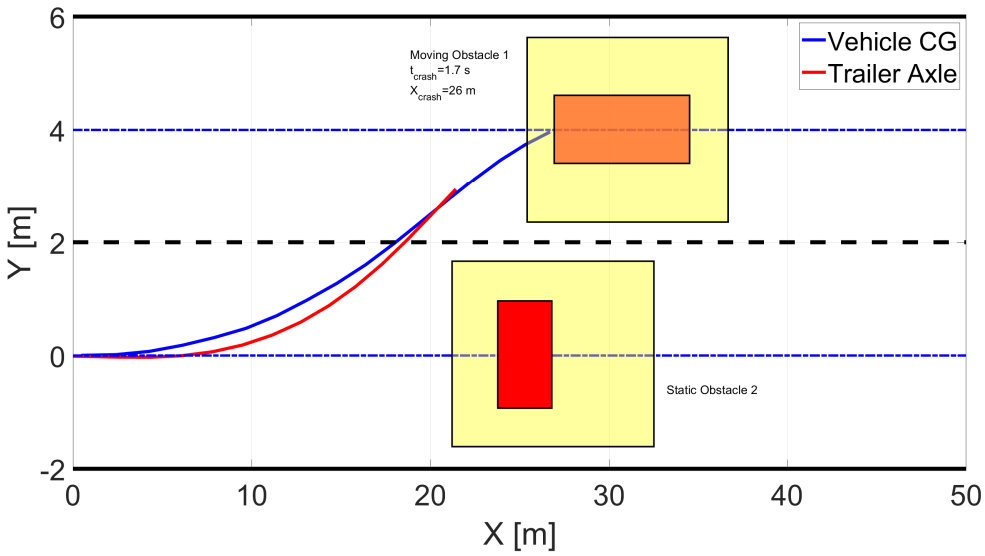

Figure 5.23: Path of ego vehicle in second crash mitigation scenario

However, in harsh braking scenarios, this assumption is not valid, and consequently, the lateral model becomes inaccurate, resulting in poor controller performance. Nonetheless, the lateral slip angle of the rear axle remains in the stable region 5.24-d.

Figure 5.23 demonstrates the searching process of the hybrid A* algorithm as it searches for the shortest trajectory from the starting point to the goal points while avoiding the pedestrian. However, in this situation, the motion planner is not able to reach the goals, and therefore, it converges to the local terminal of the moving obstacle on the second lane, a choice that imposes a lower cost than hitting the pedestrian would, see Table 5.1. As explained, if the search algorithm converges to a local terminal, its lateral coordinate Y is assigned for the rest of the points on the trajectory over the horizon as this figure illustrates. In conclusion, although having multiple goals increases the computation load, in emergency situations in which there are several obstacles, the search space reduces significantly. Thus, it is practically feasible to use the proposed motion planning method for crash mitigation scenarios as well.

The results of the third situation are presented in Figures 5.26 and 5.27. Here, the cost of hitting the pop-up obstacle is lower than that of hitting the vehicle, and consequently, the algorithm converges to the local terminal of the obstacle, Figure 5.26, and the controller requests only the maximum deceleration, Figure 5.27-a.

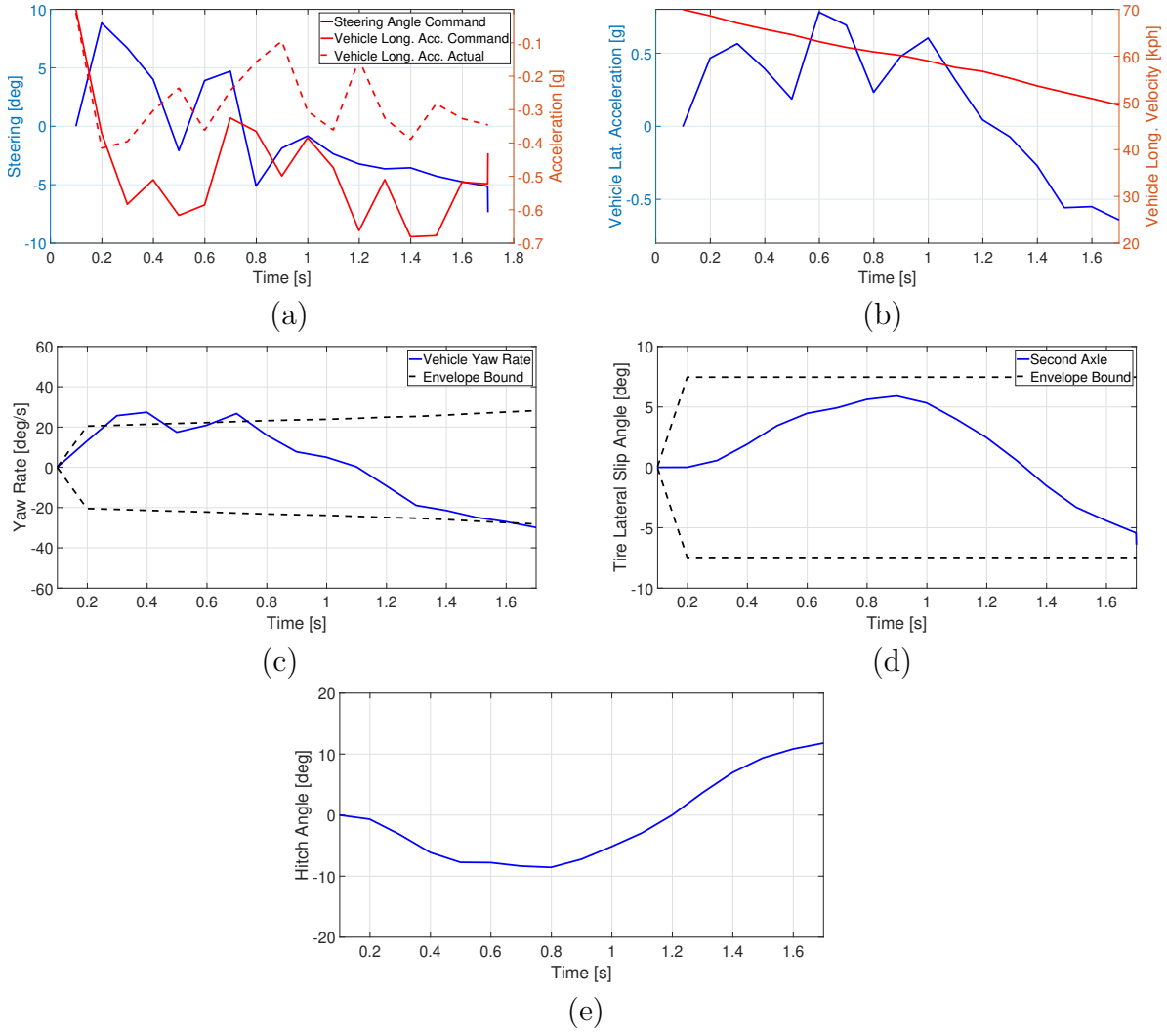

Figure 5.24: Simulation results in the obstacle prioritization scenario-lane change

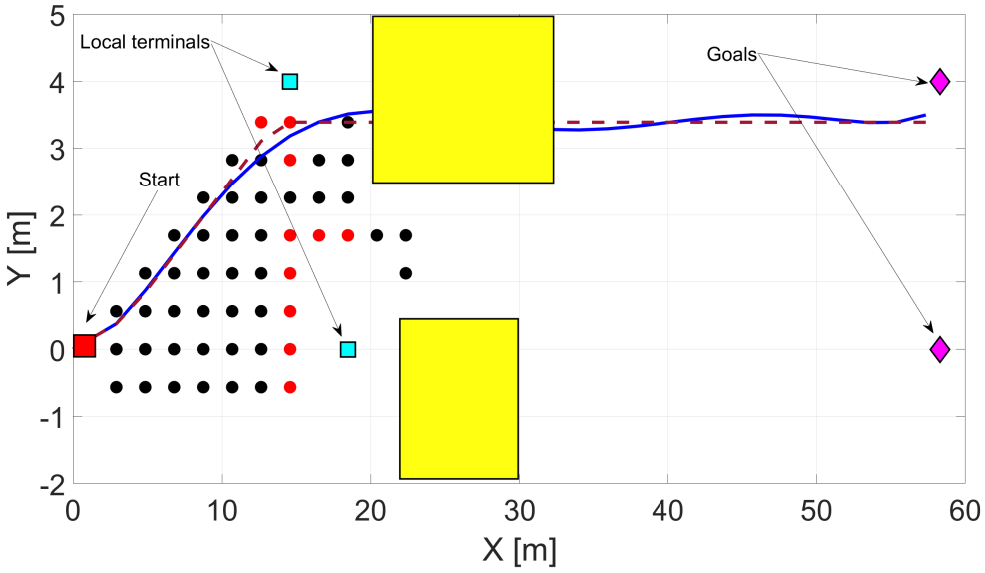

Figure 5.25: Hybrid A* algorithm search process at first time step second crash mitigation scenario

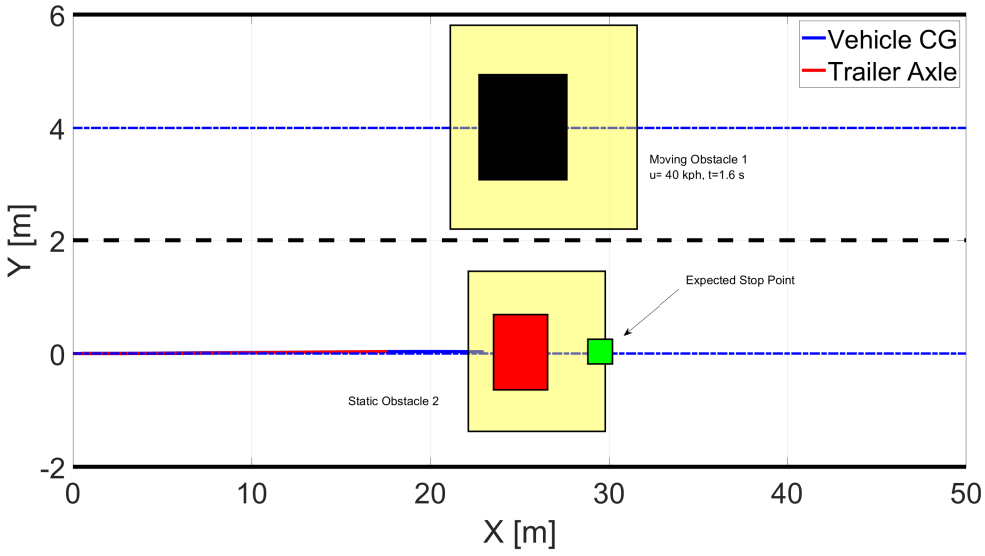

Figure 5.26: Path of ego vehicle in third crash mitigation scenario

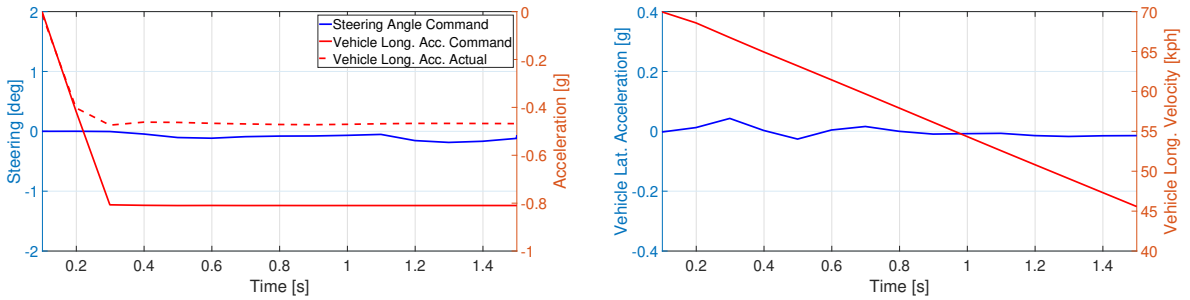

(a) (b)

Figure 5.27: Simulation results in the obstacle prioritization scenario-Straight

5.7 Summary

In this chapter, a hybrid A*-based motion planning was introduced for vehicle-trailer systems. The affine bicycle model derived in Chapter 3 was augmented with new state variables, including lateral error, heading error, and longitudinal velocity, to form a trajectory tracking model. The hybrid A* algorithm was discussed, and the potential fields of non-crossable obstacles and road curbs were defined. The proposed motion planning was developed by combining the hybrid A* algorithm and the potential fields and defining the speed control strategy. In this module, the effect of the trailer was considered by adding the potential of the trailer rear end to the cost of the current successor. Crash mitigation capability was also devised in the algorithm by defining local terminals that the algorithm may converge to based on the obstacle priority order.

The motion planning module was examined in multiple complex scenarios using the high fidelity CarSim model and MATLAB/Simulink co-simulations. The results showed the capability of the introduced motion planning method in performing a wide range of maneuvers from normal driving to obstacle avoidance scenarios. In sharp maneuvers where the hitch angle increases significantly so that the trailer violates road bounds, the algorithm was able to deviate from the centerline to keep the trailer inside the road space. In addition, where the obstacle avoidance was inevitable, the motion planning algorithm was able to prioritize the obstacles and find a solution with the minimum cost.

Chapter 6

Conclusions and Future Work

This thesis was divided into two main parts. The first part was devoted to developing a reconfigurable control system for vehicle-trailer systems. This structure was capable of considering multiple control actions either on the vehicle or on the trailer. Also, the controller would not engage when the vehicle was inside the stable region and interfered only when the vehicle was expected to cross the stability bounds. In the second part, a hybrid A*-based motion planning was developed to address the specific characteristics of vehicle-trailer systems. The proposed motion planning was able to take the effect of the trailer path into consideration while generating the trajectory. Also, the motion planning generated trajectories that ensures the stability of the vehicle-trailer system to provide feasible tracking.

6.1 Conclusions

In this thesis, first, a two-dimensional stability envelope was developed using phase plane analysis for vehicle-trailer systems. A two-layer hierarchical reconfigurable control structure was proposed to keep the vehicle inside this stability envelope. The upper layer was an MPC controller with virtual control actions for each degree of freedom and the lower layer utilized the control allocation technique to optimally map these virtual control actions to actuator commands. In addition, a motion planning module was introduced that is able to consider both the instability requirements of vehicle-trailers and the off-tracking problem systematically.

In the literature, the stability analysis of vehicle-trailer systems is mostly based on linear techniques. Although these methods provide valuable insight into instability mode

characterization, the complexity of non-linear behavior necessities a profound understanding of these modes. In this regard, a non-linear bicycle model with three degrees of freedom was derived using a non-linear brush tire model. Then, the phase portraits of the lateral dynamic for multiple steering inputs were depicted in a three-dimensional space using the sideslip angle and the yaw rate of the vehicle and hitch angle. It was observed that increasing steering angle pushes the vehicle toward higher yaw rates and stable trajectories converge to an asymptotically stable equilibrium point. However, after a specific steering angle, this equilibrium point disappears and the vehicle becomes unstable. This was also noticeable where the vehicle was vulnerable to both jackknifing and snaking, although the instability margin was different. This study showed that bounding the state variables of the vehicle can be defined as a general solution to vehicle-trailer instability regardless of its mode. Therefore, a two-dimensional stability envelope was defined based on the tire capacities and the trailer parameters.

A hierarchical control structure with two layers was developed for vehicle-trailer stabilization with minimum intervention when the vehicle is inside the stability envelope. As the upper layer, an MPC was developed through a quadratic performance index formulation. As the accuracy of the perdition model drastically affects the performance of MPC controllers, an affine bicycle model was derived based on the non-linear bicycle model. This accuracy was especially tangible where the control action was ARS and the controller was able to use the maximum capacity of the rear tires to keep the vehicle stable. The upper layer sends the optimal virtual control actions for the lower layer, the control allocation module, to be distributed optimally. In the simulations, it was observed that this structure and control strategy were able to keep the vehicle stable using all the control actions, except ATS, without any modifications in the control structure and re-tuning process. It was also seen that this control structure was able to tolerate actuator failure and adapt the distribution to keep the vehicle stable. Using stability envelope enabled the controller to prevent unnecessary control intervention as it was clearly observable in simulations and experimental tests. Among the studied control actions, active trailer steering failed to stabilize the vehicle in both snaking and jackknifing. It can be concluded that this actuator is not suitable for vehicle-trailer systems, although it was particularly effective in commercial vehicle-trailers. In addition, trailer differential braking was not able to keep the vehicle inside the stability envelope in jackknifing due to the mass distribution causing limited tire capacity.

Finally, a hybrid A*-based motion planning was proposed that considers the stability limits of vehicle-trailer systems and the off-tracking problem. From the simulation results, it was confirmed that this approach is able to provide safe, feasible, and comfortable trajectories while avoiding the obstacles. Also, thanks to combining the potential field with

the hybrid A* algorithm, the ego vehicle had a safe distance from the obstacles during all the simulated maneuvers and did not cross road bounds in the high curvature maneuver. Using the stability envelope in the process of motion planning and in the trajectory tracking controller ensured that the provided trajectory never required higher demands than the vehicle's capacity in order to keep it stable as it was following the trajectory. In the crash mitigation simulations, it was observed that using local terminals was a proper approach to prioritize the obstacles in situations that collision is not preventable. In those scenarios, the algorithm was able to find a path toward the lowest crash cost and keep the vehicle away from the obstacle with the higher priority. It was also observed that longitudinal load transfer needs to be considered in the situations that harsh braking occurs to have a better braking distribution on tires.

6.2 Future Work

In the following, some suggestions are provided for the continuation and the improvement of the current study:

Three-Dimensional Safety Envelope

In the current work, a two-dimensional stability envelope was developed to keep the vehicle stable. Although stability is the major concern of active safety systems, the vehicle maneuver needs to be safe as well. In vehicle-trailer systems, where a light-weight trailer is attached to the vehicle, large oscillations of the trailer caused by a quick maneuver or wind gust is not a threat for stability since the hitch forces are not significant. However, that can be considered as a safety concern as the trailer might collide with adjacent vehicles. Thus, expanding the current two-dimensional stability envelope to a three-dimensional safety envelope in which hitch angle rate is also limited provides an opportunity for safety improvement.

Control Action Prioritization

The proposed hierarchical control structure offers a possibility for actuator prioritization. As it was shown in the simulations, some control actions are more effective than others in different instability modes or vehicle states. For example, although trailer differential braking was not able to bring the vehicle back to the stability envelope in jackknifing, it had a more efficient performance with a moderate speed drop in snaking compared to vehicle differential braking. Thus, prioritizing available control actions based on driving conditions and vehicle states using the proposed structure can lead to more efficient stability control systems.

Considering Longitudinal Load transfer for Hard Braking Improvement

Neither in the derived affine bicycle dynamic model nor the tire capacity constraint, the pitch dynamic and longitudinal load transfer were considered. For the scenarios in which hard braking does not exist, the longitudinal load transfer is negligible, however in harsh braking, where longitudinal deceleration is substantial, this effect is important as it was noticeable in Figure 5.27. Therefore, taking longitudinal load transfer into consideration to find tire normal forces, subsequently the capacity of tires, improves the braking performance, especially in harsh braking scenarios.

References

[1] E. Lee, *Design optimization of active trailer differential braking systems for car-trailer combinations*. PhD thesis, University of Ontario Institute of Technology, 2016.

[2] T. Canada, "Canadian motor vehicle traffic collision statistics: pp. 1-6, 2015," 2015.

[3] C. E. Beal and J. C. Gerdes, "Model predictive control for vehicle stabilization at the limits of handling," *IEEE Transactions on Control Systems Technology*, vol. 21, no. 4, pp. 1258–1269, 2012.

[4] K. Kritayakirana and J. C. Gerdes, "Autonomous vehicle control at the limits of handling," *International Journal of Vehicle Autonomous Systems*, vol. 10, no. 4, pp. 271–296, 2012.

[5] M. A. Sotelo, F. J. Rodriguez, L. Magdalena, L. M. Bergasa, and L. Boquete, "A color vision-based lane tracking system for autonomous driving on unmarked roads," *Autonomous Robots*, vol. 16, no. 1, pp. 95–116, 2004.

[6] S. Vempaty and Y. He, "A review of car-trailer lateral stability control approaches," tech. rep., SAE Technical Paper, 2017.

[7] S. Vempaty, E. Lee, and Y. He, "Model-reference based adaptive control for enhancing lateral stability of car-trailer systems," in *ASME International Mechanical Engineering Congress and Exposition*, vol. 50664, p. V012T16A021, American Society of Mechanical Engineers, 2016.

[8] E. Dahlberg, *Commercial vehicle stability-focusing on rollover*. PhD thesis, Institutionen för farkostteknik, 2001.

[9] A. Hac, D. Fulk, and H. Chen, "Stability and control considerations of vehicle-trailer combination," *SAE International Journal of Passenger Cars-Mechanical Systems*, vol. 1, no. 2008-01-1228, pp. 925–937, 2008.

[10] M. Van de Molengraft-Luijten, I. J. Besselink, R. Verschuren, and H. Nijmeijer, "Analysis of the lateral dynamic behaviour of articulated commercial vehicles," *Vehicle system dynamics*, vol. 50, no. sup1, pp. 169–189, 2012.

[11] C. Gros, *Complex and adaptive dynamical systems*. Springer, 2010.

[12] N. Zhang, *Stability investigation of car-trailer combinations based on time-frequency analysis*. PhD thesis, Technische Universität, 2015.

[13] N. Zhang, H. Xiao, and H. Winner, "A parameter identification method based on time–frequency analysis for time-varying vehicle dynamics," *Proceedings of the Institution of Mechanical Engineers, Part D: Journal of Automobile Engineering*, vol. 230, no. 1, pp. 3–17, 2016.

[14] Y. He and J. Ren, "A comparative study of car-trailer dynamics models," *SAE International Journal of Passenger Cars-Mechanical Systems*, vol. 6, no. 2013-01-0695, pp. 177–186, 2013.

[15] J. Darling, D. Tilley, and B. Gao, "An experimental investigation of car—trailer high-speed stability," *Proceedings of the Institution of Mechanical Engineers, Part D: Journal of Automobile Engineering*, vol. 223, no. 4, pp. 471–484, 2009.

[16] V. Nguyen, *Vehicle handling, stability, and bifurcaiton analysis for nonlinear vehicle models*. PhD thesis, University of Maryland, 2005.

[17] E. Ono, S. Hosoe, H. D. Tuan, and S. Doi, "Bifurcation in vehicle dynamics and robust front wheel steering control," *IEEE transactions on control systems technology*, vol. 6, no. 3, pp. 412–420, 1998.

[18] B. M. Hung, S.-S. You, and H.-S. Kim, "Nonlinear vehicle stability analysis," in *International Conference on Advanced Engineering Theory and Applications*, pp. 922–931, Springer, 2016.

[19] S. Shen, J. Wang, P. Shi, and G. Premier, "Nonlinear dynamics and stability analysis of vehicle plane motions," *Vehicle System Dynamics*, vol. 45, no. 1, pp. 15–35, 2007.

[20] Z. Hao, L. Xian-sheng, S. Shu-ming, L. Hong-fei, G. Rachel, and L. Li, "Phase plane analysis for vehicle handling and stability," *International journal of computational intelligence Systems*, vol. 4, no. 6, pp. 1179–1186, 2011.

[21] S. Inagaki, I. Kushiro, and M. Yamamoto, "Analysis on vehicle stability in critical cornering using phase-plane method," *Jsae Review*, vol. 2, no. 16, p. 216, 1995.

[22] K. Koibuchi, M. Yamamoto, Y. Fukada, and S. Inagaki, "Vehicle stability control in limit cornering by active brake," tech. rep., SAE technical paper, 1996.

[23] T. Sun, E. Lee, and Y. He, "Non-linear bifurcation stability analysis for articulated vehicles with active trailer differential braking systems," *SAE International Journal of Materials and Manufacturing*, vol. 9, no. 3, pp. 688–698, 2016.

[24] A. Odhams, R. Roebuck, B. Jujnovich, and D. Cebon, "Active steering of a tractor–semi-trailer," *Proceedings of the Institution of Mechanical Engineers, Part D: Journal of Automobile Engineering*, vol. 225, no. 7, pp. 847–869, 2011.

[25] L. De Novellis, A. Sorniotti, P. Gruber, J. Orus, J.-M. R. Fortun, J. Theunissen, and J. De Smet, "Direct yaw moment control actuated through electric drivetrains and friction brakes: Theoretical design and experimental assessment," *Mechatronics*, vol. 26, pp. 1–15, 2015.

[26] D. Kasinathan, A. Kasaiezadeh, A. Wong, A. Khajepour, S.-K. Chen, and B. Litkouhi, "An optimal torque vectoring control for vehicle applications via real-time constraints," *IEEE Transactions on Vehicular Technology*, vol. 65, no. 6, pp. 4368–4378, 2015.

[27] G. Fischer, R. Heyken, and A. Trächtler, "Active stabilisation of the car/trailer combination for the bmw x5," *ATZ worldwide*, vol. 104, no. 4, pp. 7–10, 2002.

[28] Y. Zhao, S. Chen, and T. Shim, "Investigation of trailer yaw motion control using active front steer and differential brake," *SAE International Journal of Materials and Manufacturing*, vol. 4, no. 1, pp. 1057–1067, 2011.

[29] X. Yang, Z. Wang, and W. Peng, "Coordinated control of afs and dyc for vehicle handling and stability based on optimal guaranteed cost theory," *Vehicle System Dynamics*, vol. 47, no. 1, pp. 57–79, 2009.

[30] R. Shamim, M. M. Islam, and Y. He, "A comparative study of active control strategies for improving lateral stability of car-trailer systems," tech. rep., SAE Technical Paper, 2011.

[31] M. A. Fernandez and R. Sharp, "Caravan active braking system-effective stabilisation of snaking of combination vehicles," tech. rep., SAE Technical Paper, 2001.

[32] K. Rangavajhula and H.-S. J. Tsao, "Active trailer steering control of an articulated system with a tractor and three full trailers for tractor-track following," *International Journal of Heavy Vehicle Systems*, vol. 14, no. 3, pp. 271–293, 2007.

[33] Q. Wang, M. Oya, and T. Kobayashi, "Adaptive steering control scheme for combination vehicles to track target lane," in *2006 SICE-ICASE International Joint Conference*, pp. 1790–1795, IEEE, 2006.

[34] M. M. Islam, X. Ding, and Y. He, "A closed-loop dynamic simulation-based design method for articulated heavy vehicles with active trailer steering systems," *Vehicle system dynamics*, vol. 50, no. 5, pp. 675–697, 2012.

[35] M. Islam and Y. He, "Design of a preview controller for articulated heavy vehicles," *Journal of Mechanics Engineering and Automation*, vol. 3, no. 11, pp. 661–676, 2013.

[36] C. Cheng, R. Roebuck, A. Odhams, and D. Cebon, "High-speed optimal steering of a tractor–semitrailer," *Vehicle system dynamics*, vol. 49, no. 4, pp. 561–593, 2011.

[37] K. Kural, P. Hatzidimitris, N. van de Wouw, I. Besselink, and H. Nijmeijer, "Active trailer steering control for high-capacity vehicle combinations," *IEEE Transactions on Intelligent Vehicles*, vol. 2, no. 4, pp. 251–265, 2017.

[38] J. Ziegler, P. Bender, M. Schreiber, H. Lategahn, T. Strauss, C. Stiller, T. Dang, U. Franke, N. Appenrodt, C. G. Keller, *et al.*, "Making bertha drive—an autonomous journey on a historic route," *IEEE Intelligent transportation systems magazine*, vol. 6, no. 2, pp. 8–20, 2014.

[39] C. Urmson, J. Anhalt, D. Bagnell, C. Baker, R. Bittner, M. Clark, J. Dolan, D. Duggins, T. Galatali, C. Geyer, *et al.*, "Autonomous driving in urban environments: Boss and the urban challenge," *Journal of Field Robotics*, vol. 25, no. 8, pp. 425–466, 2008.

[40] M. Bertozzi, L. Bombini, A. Broggi, M. Buzzoni, E. Cardarelli, S. Cattani, P. Cerri, A. Coati, S. Debattisti, A. Falzoni, *et al.*, "Viac: An out of ordinary experiment," in *2011 IEEE Intelligent Vehicles Symposium (IV)*, pp. 175–180, IEEE, 2011.

[41] D. González, J. Pérez, V. Milanés, and F. Nashashibi, "A review of motion planning techniques for automated vehicles," *IEEE Transactions on Intelligent Transportation Systems*, vol. 17, no. 4, pp. 1135–1145, 2015.

[42] J. M. Alvarez, A. M. López, T. Gevers, and F. Lumbreras, "Combining priors, appearance, and context for road detection," *IEEE Transactions on Intelligent Transportation Systems*, vol. 15, no. 3, pp. 1168–1178, 2014.

[43] Q. Li, L. Chen, M. Li, S.-L. Shaw, and A. Nüchter, "A sensor-fusion drivable-region and lane-detection system for autonomous vehicle navigation in challenging road

scenarios," *IEEE Transactions on Vehicular Technology*, vol. 63, no. 2, pp. 540–555, 2013.

[44] V. John, K. Yoneda, Z. Liu, and S. Mita, "Saliency map generation by the convolutional neural network for real-time traffic light detection using template matching," *IEEE transactions on computational imaging*, vol. 1, no. 3, pp. 159–173, 2015.

[45] B. Kim, B. Choi, S. Park, H. Kim, and E. Kim, "Pedestrian/vehicle detection using a 2.5-d multi-layer laser scanner," *IEEE Sensors Journal*, vol. 16, no. 2, pp. 400–408, 2015.

[46] J. Hernandez-Aceituno, R. Arnay, J. Toledo, and L. Acosta, "Using kinect on an autonomous vehicle for outdoors obstacle detection," *IEEE Sensors Journal*, vol. 16, no. 10, pp. 3603–3610, 2016.

[47] A. Y. Hata and D. F. Wolf, "Feature detection for vehicle localization in urban environments using a multilayer lidar," *IEEE Transactions on Intelligent Transportation Systems*, vol. 17, no. 2, pp. 420–429, 2015.

[48] R. Geisberger, P. Sanders, D. Schultes, and C. Vetter, "Exact routing in large road networks using contraction hierarchies," *Transportation Science*, vol. 46, no. 3, pp. 388–404, 2012.

[49] H. Bast, D. Delling, A. Goldberg, M. Müller-Hannemann, T. Pajor, P. Sanders, D. Wagner, and R. F. Werneck, "Route planning in transportation networks," in *Algorithm engineering*, pp. 19–80, Springer, 2016.

[50] D. Watzenig and M. Horn, *Automated driving: safer and more efficient future driving*. Springer, 2016.

[51] M. Ardelt, C. Coester, and N. Kaempchen, "Highly automated driving on freeways in real traffic using a probabilistic framework," *IEEE Transactions on Intelligent Transportation Systems*, vol. 13, no. 4, pp. 1576–1585, 2012.

[52] S. Glaser, B. Vanholme, S. Mammar, D. Gruyer, and L. Nouveliere, "Maneuver-based trajectory planning for highly autonomous vehicles on real road with traffic and driver interaction," *IEEE Transactions on intelligent transportation systems*, vol. 11, no. 3, pp. 589–606, 2010.

[53] Y. Rasekhipour, A. Khajepour, S.-K. Chen, and B. Litkouhi, "A potential field-based model predictive path-planning controller for autonomous road vehicles," *IEEE*

Transactions on Intelligent Transportation Systems, vol. 18, no. 5, pp. 1255–1267, 2016.

[54] J. Ji, A. Khajepour, W. W. Melek, and Y. Huang, "Path planning and tracking for vehicle collision avoidance based on model predictive control with multiconstraints," *IEEE Transactions on Vehicular Technology*, vol. 66, no. 2, pp. 952–964, 2016.

[55] Y. Huang, H. Ding, Y. Zhang, H. Wang, D. Cao, N. Xu, and C. Hu, "A motion planning and tracking framework for autonomous vehicles based on artificial potential field elaborated resistance network approach," *IEEE Transactions on Industrial Electronics*, vol. 67, no. 2, pp. 1376–1386, 2019.

[56] Y. Rasekhipour, *Prioritized Obstacle Avoidance in Motion Planning of Autonomous Vehicles*. PhD thesis, University of Waterloo, 2017.

[57] P. Petrov and F. Nashashibi, "Modeling and nonlinear adaptive control for autonomous vehicle overtaking," *IEEE Transactions on Intelligent Transportation Systems*, vol. 15, no. 4, pp. 1643–1656, 2014.

[58] A. Piazzi, C. L. Bianco, M. Bertozzi, A. Fascioli, and A. Broggi, "Quintic g/sup 2/-splines for the iterative steering of vision-based autonomous vehicles," *IEEE Transactions on Intelligent Transportation Systems*, vol. 3, no. 1, pp. 27–36, 2002.

[59] P. G. Trepagnier, J. Nagel, P. M. Kinney, C. Koutsougeras, and M. Dooner, "Kat-5: Robust systems for autonomous vehicle navigation in challenging and unknown terrain," *Journal of Field Robotics*, vol. 23, no. 8, pp. 509–526, 2006.

[60] Z. Shiller, Y.-R. Gwo, *et al.*, "Dynamic motion planning of autonomous vehicles," *IEEE Transactions on Robotics and Automation*, vol. 7, no. 2, pp. 241–249, 1991.

[61] T. Berglund, A. Brodnik, H. Jonsson, M. Staffanson, and I. Soderkvist, "Planning smooth and obstacle-avoiding b-spline paths for autonomous mining vehicles," *IEEE Transactions on Automation Science and Engineering*, vol. 7, no. 1, pp. 167–172, 2009.

[62] M. F. Hsieh and U. Ozguner, "A parking algorithm for an autonomous vehicle," in *2008 IEEE Intelligent Vehicles Symposium*, pp. 1155–1160, IEEE, 2008.

[63] J. Reeds and L. Shepp, "Optimal paths for a car that goes both forwards and backwards," *Pacific journal of mathematics*, vol. 145, no. 2, pp. 367–393, 1990.

[64] S. Thrun, M. Montemerlo, H. Dahlkamp, D. Stavens, A. Aron, J. Diebel, P. Fong, J. Gale, M. Halpenny, G. Hoffmann, *et al.*, "Stanley: The robot that won the darpa grand challenge," *Journal of field Robotics*, vol. 23, no. 9, pp. 661–692, 2006.

[65] W. Lim, S. Lee, M. Sunwoo, and K. Jo, "Hybrid trajectory planning for autonomous driving in on-road dynamic scenarios," *IEEE Transactions on Intelligent Transportation Systems*, 2019.

[66] K. Chu, M. Lee, and M. Sunwoo, "Local path planning for off-road autonomous driving with avoidance of static obstacles," *IEEE Transactions on Intelligent Transportation Systems*, vol. 13, no. 4, pp. 1599–1616, 2012.

[67] M. Montremerlo, J. Beeker, S. Bhat, and H. Dahlkamp, "The stanford entry in the urban challenge," *Journal of Field Robotics*, vol. 7, no. 9, pp. 468–492, 2008.

[68] M. Werling, J. Ziegler, S. Kammel, and S. Thrun, "Optimal trajectory generation for dynamic street scenarios in a frenet frame," in *2010 IEEE International Conference on Robotics and Automation*, pp. 987–993, IEEE, 2010.

[69] M. Brown, J. Funke, S. Erlien, and J. C. Gerdes, "Safe driving envelopes for path tracking in autonomous vehicles," *Control Engineering Practice*, vol. 61, pp. 307–316, 2017.

[70] J. Funke, M. Brown, S. M. Erlien, and J. C. Gerdes, "Collision avoidance and stabilization for autonomous vehicles in emergency scenarios," *IEEE Transactions on Control Systems Technology*, vol. 25, no. 4, pp. 1204–1216, 2016.

[71] B. Yi, P. Bender, F. Bonarens, and C. Stiller, "Model predictive trajectory planning for automated driving," *IEEE Transactions on Intelligent Vehicles*, vol. 4, no. 1, pp. 24–38, 2018.

[72] B. Gutjahr, L. Gröll, and M. Werling, "Lateral vehicle trajectory optimization using constrained linear time-varying mpc," *IEEE Transactions on Intelligent Transportation Systems*, vol. 18, no. 6, pp. 1586–1595, 2016.

[73] H. Wang, Y. Huang, A. Khajepour, Y. Zhang, Y. Rasekhipour, and D. Cao, "Crash mitigation in motion planning for autonomous vehicles," *IEEE Transactions on Intelligent Transportation Systems*, vol. 20, no. 9, pp. 3313–3323, 2019.

[74] S. Khosravani, M. Jalali, A. Khajepour, A. Kasaiezadeh, S.-K. Chen, and B. Litkouhi, "Application of lexicographic optimization method to integrated vehicle control systems," *IEEE Transactions on Industrial Electronics*, vol. 65, no. 12, pp. 9677–9686, 2018.

[75] Y. Huang, H. Wang, A. Khajepour, H. Ding, K. Yuan, and Y. Qin, "A novel local motion planning framework for autonomous vehicles based on resistance network and model predictive control," *IEEE Transactions on Vehicular Technology*, vol. 69, no. 1, pp. 55–66, 2019.

[76] K. Kurzer, "Path planning in unstructured environments: A real-time hybrid a* implementation for fast and deterministic path generation for the kth research concept vehicle," 2016.

[77] R. Kala and K. Warwick, "Multi-level planning for semi-autonomous vehicles in traffic scenarios based on separation maximization," *Journal of Intelligent & Robotic Systems*, vol. 72, no. 3-4, pp. 559–590, 2013.

[78] J. Y. Hwang, J. S. Kim, S. S. Lim, and K. H. Park, "A fast path planning by path graph optimization," *IEEE Transactions on systems, man, and cybernetics-part a: systems and humans*, vol. 33, no. 1, pp. 121–129, 2003.

[79] Q. Li, Z. Zeng, B. Yang, and T. Zhang, "Hierarchical route planning based on taxi gps-trajectories," in *2009 17th International Conference on Geoinformatics*, pp. 1–5, IEEE, 2009.

[80] A. Bacha, C. Bauman, R. Faruque, M. Fleming, C. Terwelp, C. Reinholtz, D. Hong, A. Wicks, T. Alberi, D. Anderson, *et al.*, "Odin: Team victortango's entry in the darpa urban challenge," *Journal of field Robotics*, vol. 25, no. 8, pp. 467–492, 2008.

[81] J. Bohren, T. Foote, J. Keller, A. Kushleyev, D. Lee, A. Stewart, P. Vernaza, J. Derenick, J. Spletzer, and B. Satterfield, "Little ben: The ben franklin racing team's entry in the 2007 darpa urban challenge," *Journal of Field Robotics*, vol. 25, no. 9, pp. 598–614, 2008.

[82] A. Kushleyev and M. Likhachev, "Time-bounded lattice for efficient planning in dynamic environments," in *2009 IEEE International Conference on Robotics and Automation*, pp. 1662–1668, IEEE, 2009.

[83] M. Rufli and R. Siegwart, "On the application of the d* search algorithm to time-based planning on lattice graphs," in *Proc. of The 4th European Conference on Mobile Robotics (ECMR)*, pp. 105–110, Eidgenössische Technische Hochschule Zürich, 2009.

[84] M. Likhachev and D. Ferguson, "Planning long dynamically feasible maneuvers for autonomous vehicles," *The International Journal of Robotics Research*, vol. 28, no. 8, pp. 933–945, 2009.

[85] J. Ziegler, M. Werling, and J. Schroder, "Navigating car-like robots in unstructured environments using an obstacle sensitive cost function," in *2008 IEEE intelligent vehicles symposium*, pp. 787–791, IEEE, 2008.

[86] D. Dolgov, S. Thrun, M. Montemerlo, and J. Diebel, "Path planning for autonomous vehicles in unknown semi-structured environments," *The International Journal of Robotics Research*, vol. 29, no. 5, pp. 485–501, 2010.

[87] M. Jalalmaab, B. Fidan, S. Jeon, and P. Falcone, "Model predictive path planning with time-varying safety constraints for highway autonomous driving," in *2015 International Conference on Advanced Robotics (ICAR)*, pp. 213–217, IEEE, 2015.

[88] X. Qian, A. De La Fortelle, and F. Moutarde, "A hierarchical model predictive control framework for on-road formation control of autonomous vehicles," in *2016 IEEE Intelligent Vehicles Symposium (IV)*, pp. 376–381, IEEE, 2016.

[89] U. Rosolia and F. Borrelli, "Learning how to autonomously race a car: a predictive control approach," *IEEE Transactions on Control Systems Technology*, 2019.

[90] K. Zhang, J. Sprinkle, and R. G. Sanfelice, "Computationally aware control of autonomous vehicles: a hybrid model predictive control approach," *Autonomous Robots*, vol. 39, no. 4, pp. 503–517, 2015.

[91] A. Carvalho, Y. Gao, S. Lefevre, and F. Borrelli, "Stochastic predictive control of autonomous vehicles in uncertain environments," in *12th International Symposium on Advanced Vehicle Control*, pp. 712–719, 2014.

[92] B. Yi, S. Gottschling, J. Ferdinand, N. Simm, F. Bonarens, and C. Stiller, "Real time integrated vehicle dynamics control and trajectory planning with mpc for critical maneuvers," in *2016 IEEE Intelligent Vehicles Symposium (IV)*, pp. 584–589, IEEE, 2016.

[93] L. I. R. Castro, P. Chaudhari, J. Tumova, S. Karaman, E. Frazzoli, and D. Rus, "Incremental sampling-based algorithm for minimum-violation motion planning," in *52nd IEEE Conference on Decision and Control*, pp. 3217–3224, IEEE, 2013.

[94] Y. Rasekhipour, I. Fadakar, and A. Khajepour, "Autonomous driving motion planning with obstacles prioritization using lexicographic optimization," *Control Engineering Practice*, vol. 77, pp. 235–246, 2018.

[95] H. T. Smakman, *Functional integration of slip control with active suspension for improved lateral vehicle dynamics*. PhD thesis, Delft University of Technology, 2000.

[96] C. E. Beal, *Applications of model predictive control to vehicle dynamics for active safety and stability*. Stanford University, 2011.

[97] K. Well, "Aircraft control laws for envelope protection," in *AIAA Guidance, Navigation, and Control Conference and Exhibit*, p. 6055, 2006.

[98] J. Ni, J. Hu, and C. Xiang, "Envelope control for four-wheel independently actuated autonomous ground vehicle through afs/dyc integrated control," *IEEE Transactions on Vehicular Technology*, vol. 66, no. 11, pp. 9712–9726, 2017.

[99] C. G. Bobier and J. C. Gerdes, "Staying within the nullcline boundary for vehicle envelope control using a sliding surface," *Vehicle System Dynamics*, vol. 51, no. 2, pp. 199–217, 2013.

[100] C. G. Bobier-Tiu, C. E. Beal, J. C. Kegelman, R. Y. Hindiyeh, and J. C. Gerdes, "Vehicle control synthesis using phase portraits of planar dynamics," *Vehicle System Dynamics*, vol. 57, no. 9, pp. 1318–1337, 2019.

[101] C. G. Bobier, *A phase portrait approach to vehicle stabilization and envelope control*. Stanford University, 2012.

[102] C. E. Beal and C. Boyd, "Coupled lateral-longitudinal vehicle dynamics and control design with three-dimensional state portraits," *Vehicle System Dynamics*, vol. 57, no. 2, pp. 286–313, 2019.

[103] C. Tang and A. Khajepour, "Integrated stability control for narrow tilting vehicles: An envelope approach," *IEEE Transactions on Intelligent Transportation Systems*, 2020.

[104] L. Cavanini and G. Ippoliti, "Fault tolerant model predictive control for an over-actuated vessel," *Ocean Engineering*, vol. 160, pp. 1–9, 2018.

[105] S. A. Frost and M. Bodson, "Resource balancing control allocation," in *Proceedings of the 2010 American Control Conference*, pp. 1326–1331, IEEE, 2010.

[106] M. Kirchengast, M. Steinberger, and M. Horn, "Control allocation under actuator saturation: An experimental evaluation," *IFAC-PapersOnLine*, vol. 51, no. 25, pp. 48–54, 2018.

[107] S. A. Nahidi, *Reconfigurable Integrated Vehicle Stability Control Using Optimal Control Techniques*. PhD thesis, University of Waterloo, 2017.

[108] J. Wang and R. G. Longoria, "Coordinated and reconfigurable vehicle dynamics control," *IEEE Transactions on Control Systems Technology*, vol. 17, no. 3, pp. 723–732, 2009.

[109] V. Pylypchuk, S.-K. Chen, N. Moshchuk, and B. Litkouhi, "Slip-based holistic corner control," in *ASME International Mechanical Engineering Congress and Exposition*, vol. 54952, pp. 337–342, 2011.

[110] J. Guo, Y. Luo, and K. Li, "An adaptive hierarchical trajectory following control approach of autonomous four-wheel independent drive electric vehicles," *IEEE Transactions on Intelligent Transportation Systems*, vol. 19, no. 8, pp. 2482–2492, 2017.

[111] C. Tang, M. Ataei, and A. Khajepour, "A reconfigurable integrated control for narrow tilting vehicles," *IEEE Transactions on Vehicular Technology*, vol. 68, no. 1, pp. 234–244, 2018.

[112] S. M. Erlien, S. Fujita, and J. C. Gerdes, "Shared steering control using safe envelopes for obstacle avoidance and vehicle stability," *IEEE Transactions on Intelligent Transportation Systems*, vol. 17, no. 2, pp. 441–451, 2015.

[113] N. R. Kapania and J. C. Gerdes, "Design of a feedback-feedforward steering controller for accurate path tracking and stability at the limits of handling," *Vehicle System Dynamics*, vol. 53, no. 12, pp. 1687–1704, 2015.

[114] M. Luijten, "Lateral dynamic behaviour of articulated commercial vehicles," *Eindhoven University of Technology*, 2010.

[115] M. Jalaliyazdi, *Integrated vehicle stability control and power distribution using model predictive control*. PhD thesis, University of Waterloo, 2016.

[116] C. E. Beal, C. G. Bobier, and J. C. Gerdes, "Controlling vehicle instability through stable handling envelopes," in *ASME 2011 Dynamic Systems and Control Conference and Bath/ASME Symposium on Fluid Power and Motion Control*, pp. 861–868, American Society of Mechanical Engineers Digital Collection, 2011.

[117] A. Balachandran, M. Brown, S. M. Erlien, and J. C. Gerdes, "Predictive haptic feedback for obstacle avoidance based on model predictive control," *IEEE Transactions on Automation Science and Engineering*, vol. 13, no. 1, pp. 26–31, 2015.

[118] F. Borrelli, A. Bemporad, and M. Morari, *Predictive control for linear and hybrid systems*. Cambridge University Press, 2017.

[119] H. J. Ferreau, C. Kirches, A. Potschka, H. G. Bock, and M. Diehl, "qpoases: A parametric active-set algorithm for quadratic programming," *Mathematical Programming Computation*, vol. 6, no. 4, pp. 327–363, 2014.

[120] M. Abroshan, R. Hajiloo, E. Hashemi, and A. Khajepour, "Model predictive-based tractor-trailer stabilisation using differential braking with experimental verification," *Vehicle System Dynamics*, pp. 1–24, 2020.

[121] J. M. Snider *et al.*, "Automatic steering methods for autonomous automobile path tracking," *Robotics Institute, Pittsburgh, PA, Tech. Rep. CMU-RITR-09-08*, 2009.

[122] O. Amidi and C. E. Thorpe, "Integrated mobile robot control," in *Mobile Robots V*, vol. 1388, pp. 504–523, International Society for Optics and Photonics, 1991.

[123] M. Elbanhawi, M. Simic, and R. Jazar, "Receding horizon lateral vehicle control for pure pursuit path tracking," *Journal of Vibration and Control*, vol. 24, no. 3, pp. 619–642, 2018.

[124] S. H. Tamaddoni, S. Taheri, and M. Ahmadian, "Optimal preview game theory approach to vehicle stability controller design," *Vehicle system dynamics*, vol. 49, no. 12, pp. 1967–1979, 2011.

[125] T. P. Le and I. Stiharu, "An optimal preview driver model applied to a non-linear vehicle and an impaired driver," *Proceedings of the Institution of Mechanical Engineers, Part D: Journal of automobile engineering*, vol. 227, no. 4, pp. 536–548, 2013.

[126] A. Odhams and D. J. Cole, "Application of linear preview control to modelling human steering control," *Proceedings of the Institution of Mechanical Engineers, Part D: Journal of Automobile Engineering*, vol. 223, no. 7, pp. 835–853, 2009.

[127] R. S. Sharp, "Driver steering control and a new perspective on car handling qualities," *Proceedings of the Institution of Mechanical Engineers, Part C: Journal of Mechanical Engineering Science*, vol. 219, no. 10, pp. 1041–1051, 2005.

[128] J. Funke, *Collision avoidance up to the handling limits for autonomous vehicles*. Stanford University, 2015.

[129] V. A. Laurense, J. Y. Goh, and J. C. Gerdes, "Path-tracking for autonomous vehicles at the limit of friction," in *2017 American Control Conference (ACC)*, pp. 5586–5591, IEEE, 2017.

[130] J. K. Subosits and J. C. Gerdes, "A synthetic input approach to slip angle based steering control for autonomous vehicles," in *2017 American Control Conference (ACC)*, pp. 2297–2302, IEEE, 2017.

[131] P. Falcone, F. Borrelli, J. Asgari, H. E. Tseng, and D. Hrovat, "Predictive active steering control for autonomous vehicle systems," *IEEE Transactions on control systems technology*, vol. 15, no. 3, pp. 566–580, 2007.

[132] P. Falcone, H. Eric Tseng, F. Borrelli, J. Asgari, and D. Hrovat, "Mpc-based yaw and lateral stabilisation via active front steering and braking," *Vehicle System Dynamics*, vol. 46, no. S1, pp. 611–628, 2008.

[133] P. A. Theodosis and J. C. Gerdes, "Generating a racing line for an autonomous racecar using professional driving techniques," in *Dynamic Systems and Control Conference*, vol. 54761, pp. 853–860, 2011.

[134] S. F. Campbell, *Steering control of an autonomous ground vehicle with application to the DARPA urban challenge*. PhD thesis, Massachusetts Institute of Technology, 2007.

[135] S. M. LaValle and S. A. Hutchinson, "Optimal motion planning for multiple robots having independent goals," *IEEE Transactions on Robotics and Automation*, vol. 14, no. 6, pp. 912–925, 1998.

[136] M. Pivtoraiko and A. Kelly, "Efficient constrained path planning via search in state lattices," in *International Symposium on Artificial Intelligence, Robotics, and Automation in Space*, pp. 1–7, Munich Germany, 2005.

[137] Y. Kuwata, J. Teo, G. Fiore, S. Karaman, E. Frazzoli, and J. P. How, "Real-time motion planning with applications to autonomous urban driving," *IEEE Transactions on control systems technology*, vol. 17, no. 5, pp. 1105–1118, 2009.

[138] M. Taiebat, A. L. Brown, H. R. Safford, S. Qu, and M. Xu, "A review on energy, environmental, and sustainability implications of connected and automated vehicles," *Environmental science & technology*, vol. 52, no. 20, pp. 11449–11465, 2018.

[139] M. Sever, E. Kaya, M. Arslan, and H. Yazici, "Active trailer braking system design with linear matrix inequalities based multi-objective robust lqr controller for vehicle-trailer systems," in *2016 IEEE Intelligent Vehicles Symposium (IV)*, pp. 796–801, IEEE, 2016.

[140] I. Kageyama and R. Nagai, "Stabilization of passenger car-caravan combination using four wheel steering control," *Vehicle System Dynamics*, vol. 24, no. 4-5, pp. 313–327, 1995.

[141] M. Zanchetta, D. Tavernini, A. Sorniotti, P. Gruber, B. Lenzo, A. Ferrara, W. De Nijs, K. Sannen, and J. De Smet, "On the feedback control of hitch angle through torque-vectoring," in *2018 IEEE 15th International Workshop on Advanced Motion Control (AMC)*, pp. 535–540, IEEE, 2018.

[142] T. Chung and K. Yi, "Design and evaluation of side slip angle-based vehicle stability control scheme on a virtual test track," *IEEE Transactions on control systems technology*, vol. 14, no. 2, pp. 224–234, 2006.

[143] R. C. Hoffman, J. L. Stein, L. S. Louca, and K. Huh, "Using the milliken moment method and dynamic simulation to evaluate vehicle stability and controllability," *International journal of vehicle design*, vol. 48, no. 1-2, pp. 132–148, 2008.

[144] J. Åkesson, *MPCtools 1.0: Reference Manual*. Department of Automatic Control, Lund University, 2006.

[145] H. Her, Y. Koh, E. Joa, K. Yi, and K. Kim, "An integrated control of differential braking, front/rear traction, and active roll moment for limit handling performance," *IEEE Transactions on Vehicular Technology*, vol. 65, no. 6, pp. 4288–4300, 2015.

[146] E. Snapper, "Model-based path planning and control for autonomous vehicles using artificial potential fields," Master's thesis, Delft University of Technology, 2018.

[147] M. Goossens, F. Mittelbach, and A. Samarin, *The LaTeX Companion*. Reading, Massachusetts: Addison-Wesley, 1994.

[148] D. Knuth, *The TeXbook*. Reading, Massachusetts: Addison-Wesley, 1986.

[149] L. Lamport, *LaTeX — A Document Preparation System*. Reading, Massachusetts: Addison-Wesley, second ed., 1994.

[150] M. Naderi and A. K. Sedigh, "Actuator selection for over-actuated systems using the actuator effectiveness index," *International Journal of Dynamics and Control*, pp. 1–8, 2020.

[151] A. Casavola and E. Garone, "Adaptive control allocation for fault tolerant overactuated autonomous vehicles," tech. rep., UNIVERSITA DELLA CALABRIA RENDE (ITALY), 2007.

APPENDICES

Appendix A

Matrices

A.1 Affine Bicycle Model

$$\mathbf{M} = \begin{bmatrix} (m_v + m_t)u_v^x & -m_t l_h & -m_t l_{h2} & 0 \\ -m_t l_{h1} u_v^x & I_v^z + m_t l_{h1} l_h & m_t l_{h1} l_{h2} & 0 \\ -m_t l_{h2} u_v^x & I_t^z + m_t l_{h2} l_h & I_t^z + m_t l_{h2}^2 & 0 \\ 0 & 0 & 0 & 1 \end{bmatrix}$$

$$l_h = l_{h1} + l_{h2}$$

$$\mathbf{A} = -\frac{1}{u_x^T} \begin{bmatrix} (\bar{C}_t + \bar{C}_3)u_v^x & a_{12} & -\bar{C}_3(d_2) & -\bar{C}_3 u_v^x \\ (\bar{C}_t s_1 - \bar{C}_3 l_{h1})u_v^x & a_{22} & \bar{C}_3 l_{h1} d_2 & \bar{C}_3 l_{h1} u_v^x \\ -\bar{C}_3 d_2 u_v^x & a_{32} & \bar{C}_3 d_2^2 & \bar{C}_3 d_2 u_v^x \\ 0 & 0 & -u_v^x & 0 \end{bmatrix}$$

$$a_{12} = \bar{C}_t s_1 - \bar{C}_3 d_3 + (m_v + m_t)(u_v^x)^2$$
$$a_{22} = \bar{C}_t q_1^2 + \bar{C}_3 l_{h1} d_3 + l_{h1} m_t (u_v^x)^2$$
$$a_{32} = \bar{C}_3 d_2 d_3 - l_{h2} m_t (u_v^x)^2$$

and $\bar{C}_t = \bar{C}_1 + \bar{C}_2$, $s_1 = \frac{\bar{C}_1 l_1 - \bar{C}_2 l_2}{\bar{C}_t}$, $q_1 = \sqrt{\frac{\bar{C}_1 l_1^2 + \bar{C}_2 l_2^2}{\bar{C}_t}}$, $d_2 = l_3 + l_{h2}$, $d_3 = d_2 + l_{h1}$.

$$\mathbf{B_1} = \begin{bmatrix} 1 & 0 & 0 \\ 0 & 1 & 0 \\ 0 & 0 & 1 \\ 0 & 0 & 0 \end{bmatrix}, \mathbf{C} = \begin{bmatrix} 1 & 0 & 0 & 0 \\ 0 & 1 & 0 & 0 \end{bmatrix}, \mathbf{F} = \begin{bmatrix} 1 & 1 & 1 \\ l_1 & -l_2 & -l_{h1} \\ 0 & 0 & -d_2 \\ 0 & 0 & 0 \end{bmatrix}$$

$$\mathbf{L} = -\begin{bmatrix} \bar{C}_1 & \bar{C}_2 & \bar{C}_3 \\ l_1\bar{C}_1 & -l_2\bar{C}_2 & -l_{h1}\bar{C}_3 \\ 0 & 0 & -\bar{C}_3 d_2 \\ 0 & 0 & 0 \end{bmatrix}, \mathbf{B_2} = -\mathbf{L} \tag{A.1}$$

A.2 Performance Index

$$\mathbf{\Psi} = \begin{bmatrix} C \\ CA \\ CA^2 \\ \vdots \\ CA^{h_p-1} \end{bmatrix}, \tag{A.2}$$

$$\mathbf{\Gamma} = \begin{bmatrix} CB \\ CAB + CB \\ \vdots \\ C\sum_{i=0}^{h_p-2} A^i B \end{bmatrix}, \tag{A.3}$$

$$\mathbf{\Phi} = \begin{bmatrix} CB & 0 & \dots & 0 \\ CAB + CB & CB & \dots & 0 \\ \vdots & \ddots & \ddots & 0 \\ C\sum_{i=0}^{h_p-2} A^i B & \dots & \dots & C\sum_{i=0}^{h_p-h_c-2} A^i B \end{bmatrix}, \tag{A.4}$$

$$\mathbf{\Lambda} = \begin{bmatrix} C \\ CA + C \\ \vdots \\ C\sum_{i=0}^{h_p-2} A^i \end{bmatrix} \tag{A.5}$$

$$\Delta\mathbb{V}(k) = \begin{bmatrix} \Delta V(k|k) \\ \Delta V((k+1)|k) \\ \vdots \\ \Delta V((k+h_c-1)|k) \end{bmatrix} \tag{A.6}$$

A.3 Trajectory Tracking Affine Bicycle Model

$$\mathbf{M}_p = \begin{bmatrix} (m_v+m_t)u_v^x & -m_t l_h & -m_t l_{h2} & 0 & 0 & 0 & 0 & 0 \\ -m_t l_{h1} u_v^x & I_v^z + m_t l_{h1} l_h & m_t l_{h1} l_{h2} & 0 & 0 & 0 & 0 & 0 \\ -m_t l_{h2} u_v^x & I_t^z + m_t l_{h2} l_h & I_t^z + m_t l_{h2}^2 & 0 & 0 & 0 & 0 & 0 \\ 0 & 0 & 0 & 1 & 0 & 0 & 0 & 0 \\ 0 & 0 & 0 & 0 & 1 & 0 & 0 & 0 \\ 0 & 0 & 0 & 0 & 0 & 1 & 0 & 0 \\ 0 & 0 & 0 & 0 & 0 & 0 & 1 & 0 \\ 0 & 0 & 0 & 0 & 0 & 0 & 0 & 1 \end{bmatrix}$$

$$l_h = l_{h1} + l_{h2}$$

$$\mathbf{A}_p = -\frac{1}{u_x^T} \begin{bmatrix} (\bar{C}_t + \bar{C}_3)u_v^x & a_{12} & -\bar{C}_3(d_2) & -\bar{C}_3 u_v^x & 0 & 0 & 0 & 0 \\ (\bar{C}_t s_1 - \bar{C}_3 l_{h1})u_v^x & a_{22} & \bar{C}_3 l_{h1} d_2 & \bar{C}_3 l_{h1} u_v^x & 0 & 0 & 0 & 0 \\ -\bar{C}_3 d_2 u_v^x & a_{32} & \bar{C}_3 d_2^2 & \bar{C}_3 d_2 u_v^x & 0 & 0 & 0 & 0 \\ 0 & 0 & -u_v^x & 0 & 0 & 0 & 0 & 0 \\ 0 & 0 & 0 & 0 & 0 & 0 & 0 & 0 \\ 0 & 0 & 0 & 0 & -u_v^x & 0 & 0 & 0 \\ -(u_v^x)^2 & 0 & 0 & 0 & 0 & 0 & 0 & -(u_v^x)^2 \\ 0 & -u_v^x & 0 & 0 & 0 & 0 & 0 & 0 \end{bmatrix}$$

$$a_{12} = \bar{C}_t s_1 - \bar{C}_3 d_3 + (m_v + m_t)(u_v^x)^2$$
$$a_{22} = \bar{C}_t q_1^2 + \bar{C}_3 l_{h1} d_3 + l_{h1} m_t (u_v^x)^2$$
$$a_{32} = \bar{C}_3 d_2 d_3 - l_{h2} m_t (u_v^x)^2$$

and $\bar{C}_t = \bar{C}_1 + \bar{C}_2$, $s_1 = \frac{\bar{C}_1 l_1 - \bar{C}_2 l_2}{\bar{C}_t}$, $q_1 = \sqrt{\frac{\bar{C}_1 l_1^2 + \bar{C}_2 l_2^2}{\bar{C}_t}}$, $d_2 = l_3 + l_{h2}$, $d_3 = d_2 + l_{h1}$.

$$\mathbf{B}_p = \begin{bmatrix} \bar{C}_1 & 0 \\ \bar{C}_1 l_1 & 0 \\ 0 & 0 \\ 0 & 0 \\ 0 & 1 \\ 0 & 0 \\ 0 & 0 \\ 0 & 0 \end{bmatrix}, \mathbf{C}_p = \begin{bmatrix} 1 & 0 & 0 & 0 & 0 & 0 & 0 & 0 \\ 0 & 1 & 0 & 0 & 0 & 0 & 0 & 0 \\ 0 & 0 & 0 & 0 & 1 & 0 & 0 & 0 \\ 0 & 0 & 0 & 0 & 0 & 1 & 0 & 0 \\ 0 & 0 & 0 & 0 & 0 & 0 & 1 & 0 \\ 0 & 0 & 0 & 0 & 0 & 0 & 0 & 1 \end{bmatrix}, \mathbf{F} = \begin{bmatrix} 1 & 1 & 1 \\ l_1 & -l_2 & -l_{h1} \\ 0 & 0 & -d_2 \\ 0 & 0 & 0 \\ 0 & 0 & 0 \\ 0 & 0 & 0 \\ 0 & 0 & 0 \\ 0 & 0 & 0 \end{bmatrix}$$

$$\mathbf{L}_p = -\begin{bmatrix} \bar{C}_1 & \bar{C}_2 & \bar{C}_3 \\ l_1\bar{C}_1 & -l_2\bar{C}_2 & -l_{h1}\bar{C}_3 \\ 0 & 0 & -\bar{C}_3 d_2 \\ 0 & 0 & 0 \\ 0 & 0 & 0 \\ 0 & 0 & 0 \\ 0 & 0 & 0 \\ 0 & 0 & 0 \end{bmatrix}, \mathbf{E}_p = \begin{bmatrix} 0 \\ 0 \\ 0 \\ 0 \\ 0 \\ 0 \\ 0 \\ -u_x^T \end{bmatrix}$$